Study on the Progenitors of Type II Supernovae based on Extensive Observations

Tatsuya Nakaoka

2019 Mar 4

Abstract

A core-collapse supernova (CC SN) is thought to be ignited by the core-collapse in a massive star having initial mass of $\gtrsim$ 8–10 $M_{\odot}$. One of the subtypes of CC SNe is Type II SNe (SNe II) which show hydrogen absorption/emission lines in their early spectra. SNe II showing the plateau phase in their light curves are classified into SNe II-plateau (SNe IIP). SNe II which show the helium absorption lines as well as hydrogen ones in their early phase are classified into SNe IIb. Progenitors of SNe IIP are widely known as red supergiants (RSGs). Recently, some SNe II show a sign of a interaction between the SN ejecta and the circumstellar matter (CSM) which is likely to be originated from the stellar wind of the progenitor. It is not well known how the progenitor star have expelled their atmosphere just before the explosion, and unveiling the CSM properties should be a probe to understand the progenitor's stellar evolution.

Recently, a quite conspicuous objects showing the fast-declining light curves have been found. They are called as 'rapidly-evolving transients'. Their explosion nature are poorly understood. Due to the short timescale, spectral properties were not well clarified until today. Since little spectra are obtained from these transients, the progenitor of the rapidly evolving transients is still unknown. These observational samples are limited, because the prompt follow up observations just after the discovery are necessary.

We systematically performed the prompt and ceaseless follow-up observations of 23 SNe with imaging and spectroscopy mode, from the explosion through the tail phase. In our extensive observations, we found that SNe 2016bkv and 2017czd show quite conspicuous properties. These data would provide unique information enough to unveil the unknown progenitor properties of peculiar SNe including the rapidly-evolving transients.

We performed optical and near-infrared observations of a low-luminosity Type IIP (LL SN IIP) SN 2016bkv from the initial rising phase to the plateau phase. The ejecta mass in SN 2016bkv is larger than that of the well-studied LL IIP SN 2003Z. In the early phase, SN 2016bkv shows a strong bump in the light curve. In addition, the optical spectra in this bump phase exhibit a blue continuum accompanied with a narrow Hα emission line. These features indicate an interaction between the SN ejecta and the CSM. Assuming the ejecta-CSM interaction scenario, the mass loss rate is estimated to be $\sim 1.7 \times 10^{-2}$ $M_{\odot}$ yr^{-1} within a few years before the SN explosion. This is comparable to or even larger than the largest mass loss rate observed for the Galactic red supergiants ($\sim 10^{-3}$ $M_{\odot}$ yr^{-1} for VY CMa). We suggest that the progenitor star of SN 2016bkv experienced a violent mass loss just before the SN explosion.

In addition, we performed optical and near-infrared observations of the rapidly evolving SN 2017czd that shows hydrogen features. The optical light curves exhibit a short plateau phase ($\sim$13 days in the R-band) followed by a rapid decline by 4.5 mag in $\sim$ 20 days after the peak. The decline rate is larger than those of any standard SNe, and close to those of rapidly evolving transients. The peak absolute magnitude is -16.8 mag in the V-band, which is within the observed range for SNe IIP and rapidly evolving transients. The spectra of SN 2017czd clearly show the hydrogen features and resemble those of SNe IIP at early phase (3–19 days). The Hα line, however, does not evolve much with time and it becomes similar to those in SNe IIb at late phases. We calculate the synthetic light curves using a SN IIb progenitor which has

16 $M_\odot$ at the zero-age main sequence and evolves in a binary system. The model with a low explosion energy (5×10^{50} erg) and a low ^{56}Ni mass (0.003 $M_\odot$) can reproduce the short plateau phase as well as the sudden drop of the light curve as observed in SN 2017czd. We conclude that SN 2017czd might be the first identified weak explosion from a SN IIb progenitor. We suggest that some rapidly evolving transients can be explained by such a weak explosion of the progenitors with little hydrogen-rich envelope.

From our findings on SN 2016bkv, we recognized that the progenitor of SNe II may occasionally have blown a large amount of the CSM just before the SN explosion. The interaction luminosity depends on the CSM density. It is known that the luminosity of SNe IIP widely distributes in the range of $M_V = -14 - -17$ mag. In the case of luminous SNe II, a signature of the CSM may not be detected due to its relative faintness. The sign of the CSM interaction in SN 2016bkv was found due to the low-peak luminosity of the SN itself. From these facts, we speculate that the progenitor of SNe II commonly may have the CSM more or less. We found that the ejected ^{56}Ni masses of SNe 2016bkv and 2017czd are extremely low from their low luminosity at the tail phases. Although the ^{56}Ni mass should be dependent on the explosion energy and its progenitor mass, the initial masses of their progenitors are relatively large, e.g., the yellow supergiant for the SN 2017czd progenitor. This fact implies that the heavy elements synthesized in the SN explosion may fall back to the central region to some degrees, and it may form the compact remnant, e.g., black hole. These phenomena may be related to the moderately large-mass black hole discovered by the observations of gravitational wave.

Contents

List of Figures

List of Tables

Chapter 1

Introduction

1.1 Stellar Evolution

1.1.1 Main Sequence Star and Red Giant

A star spends most of its life as a main sequence star. The energy source of the main sequence star is nuclear fusion of hydrogen, but the dominant process differs depending on the initial mass (or central temperature) of the star. For light stars ($\lesssim 1.1\ M_\odot$), the proton-proton chain reaction is the main process. Figure 1.1 shows the process of the proton-proton chain reaction. The proton-proton chain reaction is a nuclear fusion reaction to a helium atom from four hydrogen atoms through three main processes.

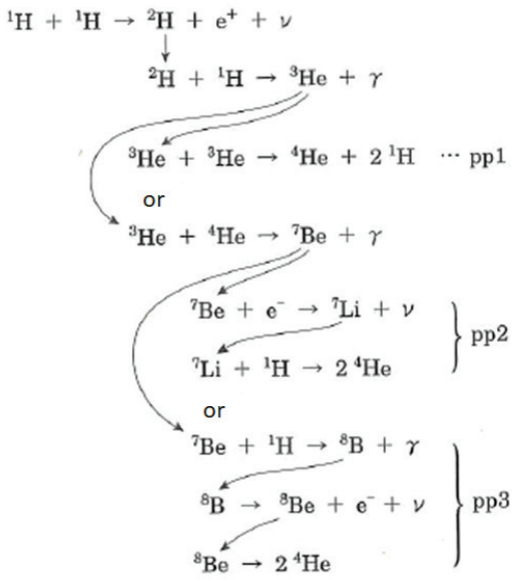

Figure 1.1: Proton-proton chain reaction(Clayton, 1984)

For heavier stars than 1.1 $M_\odot$, the temperature at the stellar core reaches $\sim 2\times10^7$ K and the

carbon-nitrogen-oxygen fusion reaction (CNO cycle) is the dominant process. Figure 1.2 shows the process of the CNO cycle. The CNO cycle is the reaction mediated by carbon, nitrogen and oxygen, and convert four hydrogen atoms to one helium atoms. However, since the reaction rate of CNO cycle is higher than that of proton-proton chain reaction, the heavier star has a shorter lifetime in the age of main sequence star phase.

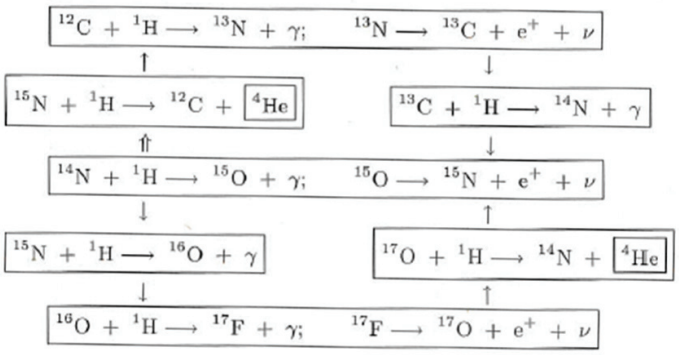

Figure 1.2: CNO cycle(Clayton, 1984)

As the hydrogen in the stellar center is synthesized to helium, the region of the hydrogen nuclear fusion gradually moves to the outer layer in the star. The central helium nucleus shrinks to support the outer atmosphere, and the temperature rises. In this shell-burning phase, the adiabatic expansion is ineffective because of the thin reaction layer. The temperature becomes higher and the hydrogen burns more intensely. The outer layer expands and the star evolve a red giant.

1.1.2 Red Supergiant

In the case of a high mass star ($\gtrsim$ 8–10 $M_{\odot}$), the nuclear fusion continue until the iron which is final product for the nuclear fusion. As a result of these nuclear fusion, the star has an onion-like layers like the Figure 1.3.

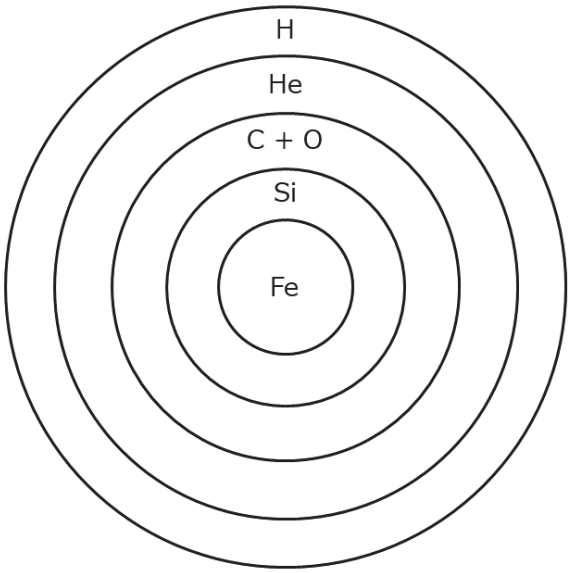

Figure 1.3: The onion-like layers of a massive star just before the core-collapse (Clayton, 1984)(not to scale).

As the core of the star consists of iron atoms, the nuclear fusion stops and the generation of energy ceases. The core further shrinks and the temperature becomes higher. When the temperature in the core reaches 10 billion K, the energy of photons is higher than that of iron atoms, and iron atoms are decomposed by light. This process is an endothermic reaction, so the core loses its supporting pressure. Therefore, outer layer of the star fall toward the center. This is the core-collapse which is one of the origin of the supernova.

1.2 Supernova

Supernovae (SNe) are classified into some Types using the spectral features and light curve properties, which reflects the diversity in their progenitor stars and explosion mechanisms.

Typical spectra for each Type of SN are shown in the Figure 1.4. SNe are roughly divided into two Types depending on the hydrogen absorption lines. In Type I supernovae (SNe Ia), the hydrogen absorption / emission lines are not seen. In Type II supernovae (SNe II), hydrogen lines are seen. In SNe Ia are divided into Type Ia supernovae (SNe Ia) which shows the strong silicon absorption lines, Type Ib supernovae (SNe Ib) which shows helium absorption lines, and Type Ic supernovae (SNe Ic) which shows strong oxygen and calcium absorption lines. It is widely believed that the progenitors of SNe Ia are white dwarfs and that of SNe Ib/c and SNe II are evolved to high-mass stars.

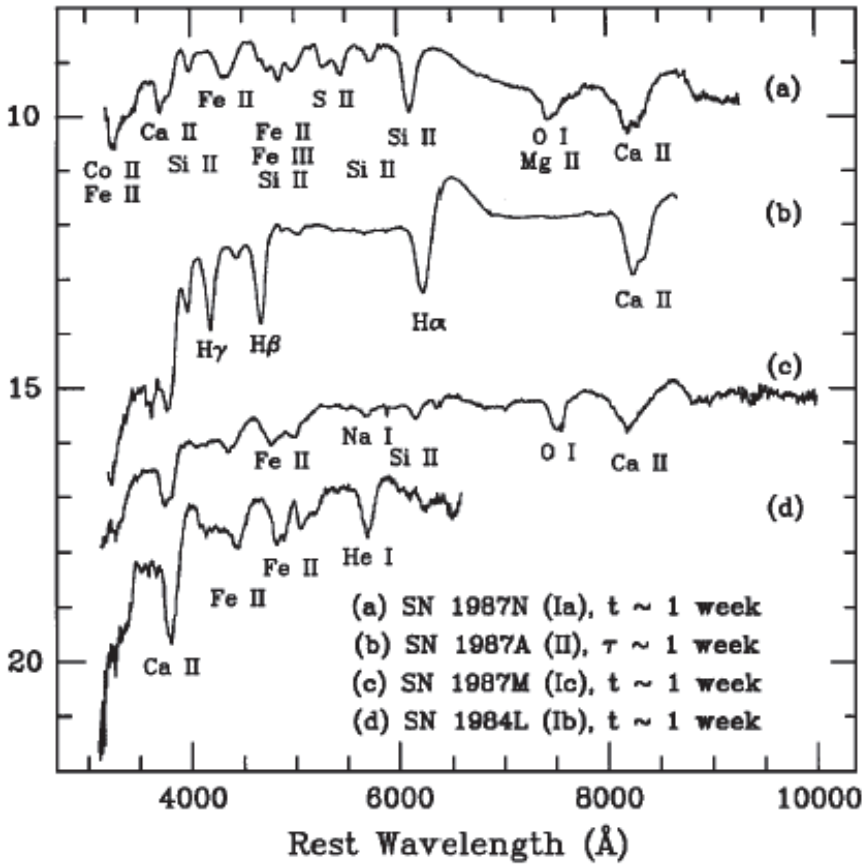

Figure 1.4: Typical spectra for each subtype of SN (Filippenko, 1997).

Figure 1.5 demonstrates the rate of each subtype of SNe that appeared in nearby galaxies ($\lesssim$ 60 Mpc^3 volume-limited; Li et al., 2011). Among the core-collapse supernovae (CC SNe), hydrogen absorption lines do not appear in their spectra in SNe Ib and Ic. The origin of these SNe are thought to be core-collapse in quite massive stars. It is believed that the outer hydrogen layer are stripped off due to their strong radiation pressure (or the mass exchange between close binary system). On the other hand, since the SNe II has a large amount of hydrogen layer, it is generally considered that a progenitor star of SNe II is usually lighter than those of SNe Ib or Ic. The most frequently appearing SN subtype in the nearby galaxy is the SNe II. As SNe Ia are explosions of white dwarfs, there is no direct relationship with CC SNe. However, since the generated mass of ^{56}Ni is generally larger than that of the CC SNe, SNe Ia becomes a brighter SN. Therefore, the discovery ratio of SNe Ia is the most highest in the all subtypes.

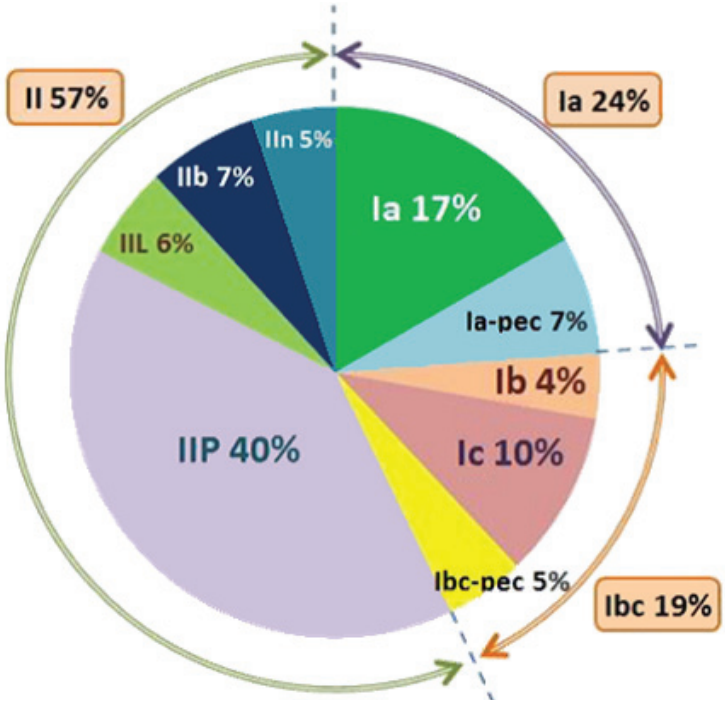

Figure 1.5: The occurring rate of each SN subtype(Li et al., 2011) ($\lesssim$ 60 Mpc^3 volume-limited).

1.3 Type II SN

SNe with hydrogen absorption features in their spectra are classified as SNe II (Filippenko, 1997). SNe II are roughly divide into four subtypes; Type II-Plateau (SNe IIP), II-Linear (SNe IIL), II-narrow (SNe IIn), and IIb (SNe IIb). Each subtype has different characteristics in its light curves and spectra.

1.3.1 Type II-Plateau SN

SNe IIP are characterized by hydrogen features in their early-phase spectra and the 'plateau' in their optical light curves lasting for $\sim$100 days (Filippenko, 1997). Figure 1.6 shows the $UBVRI$-band light curve of SN IIP 1999em (Leonard et al., 2002a). This object shows the plateau between about 10 and 90 days after the explosion. After the plateau, the luminosity of SNe IIP suddenly drops from the plateau in the optical bands.

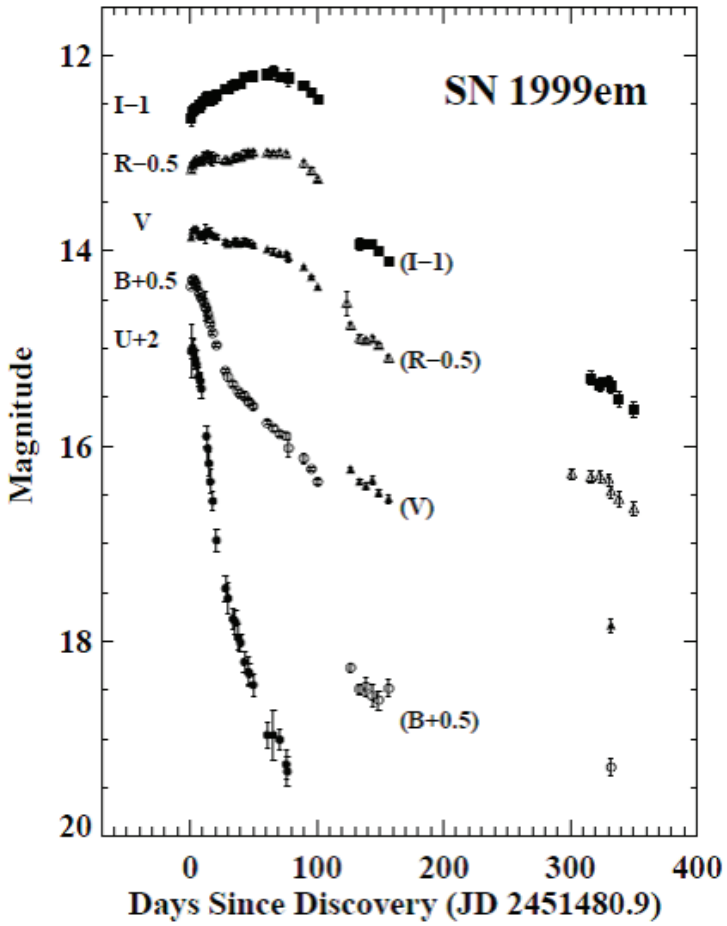

Figure 1.6: The light curve of typical SNe IIP 1999em(Leonard et al., 2002a)

SNe IIP represent the most common class of SNe and occupy ∼70% of core-collapse SNe within 60 Mpc (Li et al., 2011; Graur et al., 2017; Shivvers et al., 2017). Through the analysis of pre-explosion image (Smartt, 2009, 2015), red supergiants are identified as the progenitors of SNe IIP in accordance with standard theoretical predictions of the massive star evolution (e.g., Grassberg et al., 1971; Heger et al., 2003). However, these confirmed progenitors are still limited for relatively lower mass ones, $\lesssim 20 M_{\odot}$.

The observational properties of SNe IIP show various diversities; for example, in the durations of the plateau and the shapes of the initial light curves (Anderson et al., 2014; Faran et al., 2014; Sanders et al., 2015; Pejcha & Prieto, 2015; Valenti et al., 2016). Several SNe IIP which decline slowly in the plateau phase are classified as rather SNe IIL (Faran et al., 2014; Bose et al., 2015), but the definition of SNe IIL is still uncertain.

1.3.2 Type IIb SN

SNe IIb exhibit both hydrogen and helium lines in their early spectra, and their optical light curves show one or two peaks (Bersten et al., 2018). Figure 1.7 shows the R-band light curves

of SN 1993J (two peaks) and SN 2008ax (one peak). Both light curves are similar around the maximum and after the maximum, however the evolution of he pre-maximum is different. These difference comes from the radius of the progenitor (e.g., Maeda et al., 2014; Ouchi & Maeda, 2017). Yellow supergiant (YSG) stars have been detected in pre-explosion images for some SNe IIb (e.g., Aldering et al., 1994; Crockett et al., 2008; Van Dyk et al., 2014).

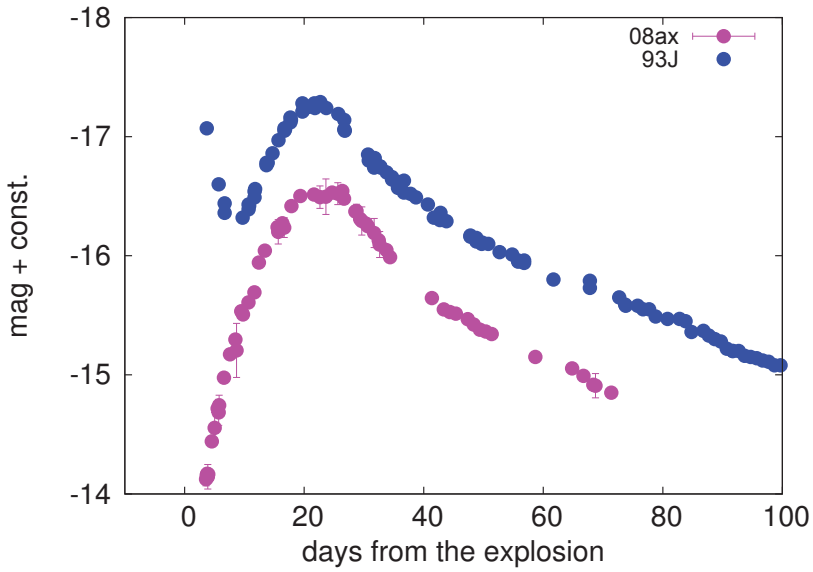

Figure 1.7: The R-band light curves of SN 1993J (Richmond et al., 1996a) and SN 2008ax (Pastorello et al., 2008)

1.3.3 Low-Luminosity Type II-Plateau SN

The absolute magnitudes in the plateau phase in SNe IIP also show a large variety, ranging from $\sim$−14 to $\sim$−17 mag (Anderson et al., 2014). In the past $\sim$20 years, a subclass of faint SNe IIP has been recognized, called low-luminosity SNe IIP (LL SNe IIP; Pastorello et al., 2004). A typical luminosity of LL SNe IIP is lower than those of normal SNe IIP by 2–3 mag. Typical velocities of the absorption lines are also lower than those of normal SNe IIP by a factor of 3–4 (Pastorello et al., 2004). The origin of these LL SNe IIP is still under debate. One of the candidate of LL SNe IIP is weak explosions of the less massive stars ($\sim$9 $M_{\odot}$). Figure 1.8 is the relation between the mass of the synthesized ^{56}Ni and the peak absolute magnitude. Almost LL SNe IIP locate at the tail of typical SNe IIP. It is natural that the progenitor of LL SNe IIP is the less massive stars than those of typical SNe IIP.

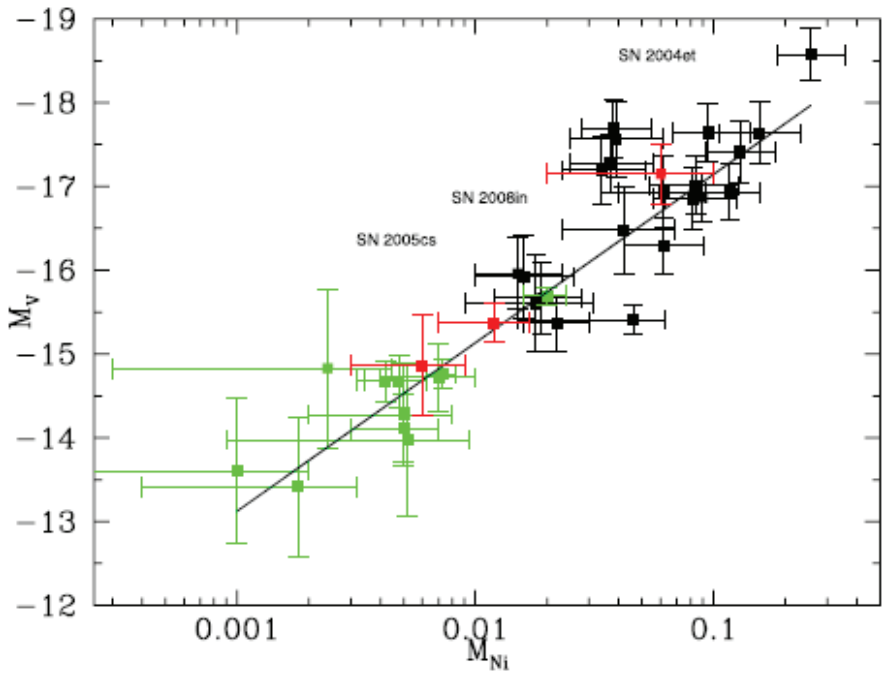

Figure 1.8: The relation between the mass of ^{56}Ni and peak absolute magnitude. Black is typical SNe IIP and green is LL SNe IIP. SN 2005cs and SN 2008in (a part of red point) is LL SNe IIP and SN 2004et is SNe IIP (Spiro et al., 2014).

The other candidate of LL SNe IIP is failed explosions of the core-collapses in very massive stars ($\sim$25 $M_\odot$) (Turatto et al., 1998; Chugai & Utrobin, 2000; Kitaura et al., 2006). Figure 1.9 shows the mass of ^{56}Ni and main sequence mass for several CC SNe (Nomoto et al., 2003). In this figure, the existence of two branches (hypernova and faint SN) are suggested for very massive progenitors ($\gtrsim$ 25 $M_\odot$). SN 1997D which is located at the faint SN branch is classified as LL SN IIP.

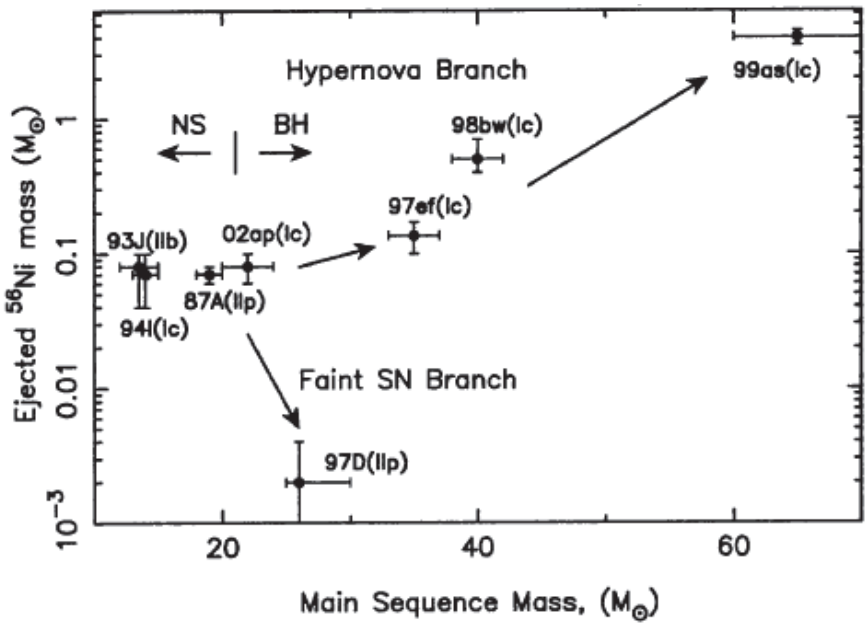

Figure 1.9: The mass of ^{56}Ni and main sequence mass for several SNe(Nomoto et al., 2003).

To date, several LL SNe IIP have been identified and studied (e.g., Turatto et al., 1998; Pastorello et al., 2004; Spiro et al., 2014; Lisakov et al., 2017, 2018). However, the sample covering both the initial rising phase and the tail after the plateau phase is still rare.

1.4 Rapidly Evolving Transients

Rapidly evolving luminous transients have been discovered by Panoramic Survey Telescope and Rapid Response System (Pan-STARRS) (Drout et al., 2014) and they are called as rapidly evolving transients here. Figure 1.10 shows the multi color light curve of the object displayed by (Drout et al., 2014). Their rise and decline rates are much faster than those in fast-evolving SNe Ib/c like SN 1994I (Richmond et al., 1996b).

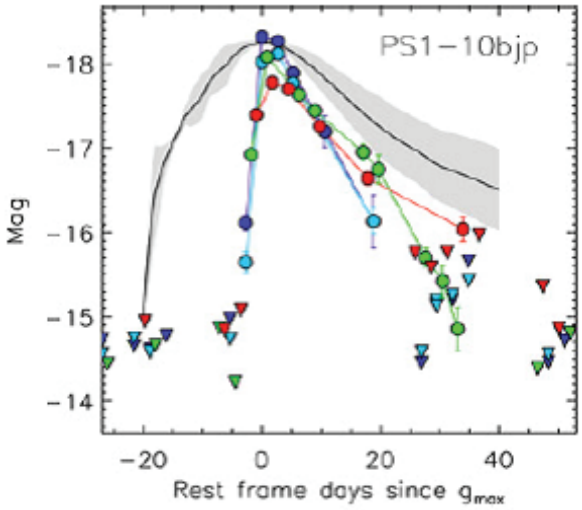

Figure 1.10: The multi color light curve of PS1-10bjp which discovered by Pan-STARRS (Drout et al., 2014).

Recently an increasing number of rapid transients have been found with wide-field and high-cadence survey, e.g., Subaru Hyper Suprime-Cam Transient Survey (Tanaka et al., 2016), Palomar Transient Factory (Whitesides et al., 2017), Dark Energy Survey Supernova Program (Pursiainen et al., 2018), and K2/Kepler (Rest et al., 2018). Most of them are discovered in star-forming galaxies, implying massive progenitors. However, the exact nature of the progenitors and explosions remain elusive.

The absolute peak magnitudes of rapidly evolving transients have a large variety, $-15 - -22$ mag (Drout et al., 2014; Pursiainen et al., 2018). Spectral features also show a diversity: some of them show the blue featureless spectra with photospheric temperatures of 20000-30000 K (Drout et al., 2014; Pursiainen et al., 2018); while, others show the absorption features including helium lines, e.g., for SNe 2002bj (Poznanski et al., 2010), 2005ek (Drout et al., 2013) and 2010X (Kasliwal et al., 2010). However, hydrogen features have never been clearly identified in them.

Many different kinds of scenarios have been proposed for the progenitors of the rapidly evolving transients. For example, rapidly evolving transients may be related to peculiar CC SNe, e.g., ultra-stripped SNe (e.g., Tauris et al., 2013; Moriya et al., 2017a; De et al., 2018), electron-capture SNe (e.g., Moriya & Eldridge, 2016), magnetar-powered SNe (e.g., Whitesides et al., 2017), and failed CC SN explosions (e.g., Moriya et al., 2010). The failed core-collapse SN explosions may also lead to the fallback accretion-powered rapidly evolving SNe (e.g., Dexter & Kasen, 2013). Some others may be powered by the interaction between the SN ejecta and the circumstellar material (e.g., Kleiser et al., 2018b), which in fact nicely reproduces the light curves of well-observed KSN 2015K (Rest et al., 2018). Other proposed mechanisms include tidal disruption events (Drout et al., 2014) and peculiar thermonuclear explosions (Bildsten et al., 2007; Shen et al., 2010). In fact, the nature of the progenitor and explosion is not clear for many rapid transients partly due to the lack of good photometric and spectroscopic coverage. To understand the nature of the rapid transients, extensive follow-up observations are necessary.

1.5 Circumstellar Matter

Several SNe II show the narrow hydrogen emission lines in the early spectra, called as Type IIn supernova (SNe IIn). Figure 1.11 shows the model of circumstellar matter (CSM) and supernova. Before the explosion, the CSM is formed by a stellar wind or explosion at outer layer of the progenitor star. After the explosion, the SN ejecta and CSM interact in several hours to several years. It is considered that the origin of emission lines come from this interaction (Moriya et al., 2017b; Morozova et al., 2017; Yaron et al., 2017; Dessart et al., 2017).

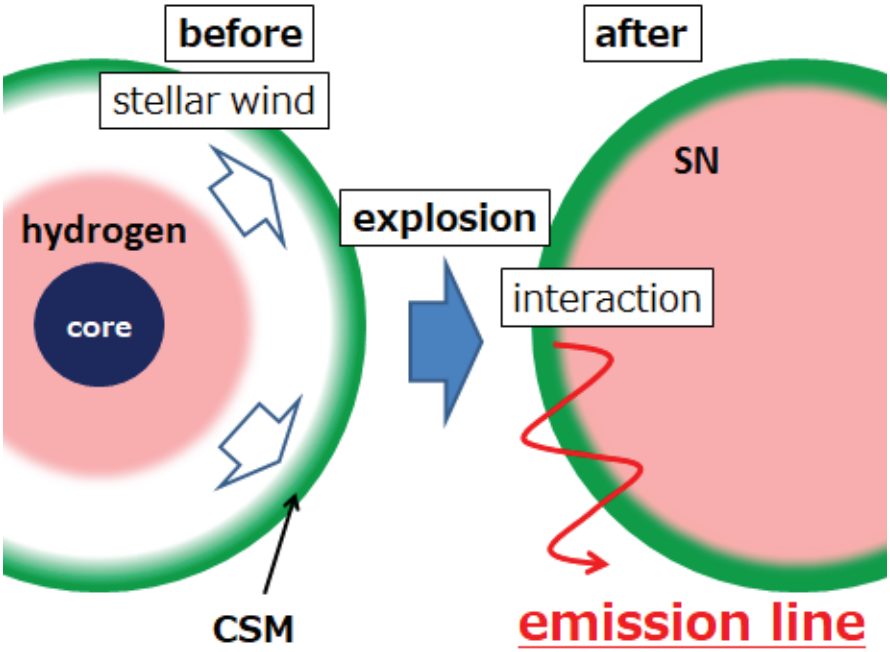

Figure 1.11: The model of CSM and interaction between SN ejecta and CSM.

Figure 1.12 shows the spectra of SNe IIn; SN 1998S which is one of the good sample of SNe IIn (Fassia et al., 2001). In the early phase, SN 1998S shows the blue continuum and hydrogen emission lines with a wide wing. The emission lines of C III , N III and He II are also displayed in this spectra. However, SN 2012aw, typical SNe IIP, shows the blue continuum and absorption lines.

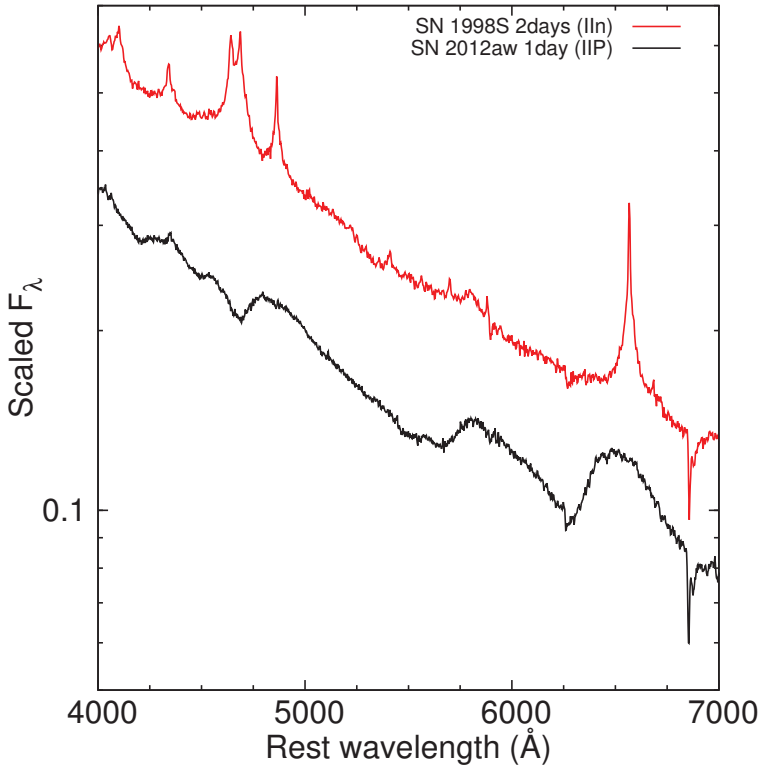

Figure 1.12: The spectra of SN IIn 1998S (Fassia et al., 2001) and typical SN IIP 2012aw(Bose et al., 2013).

Recently, several SNe II show hydrogen emission lines in their early phase as described above. Figure 1.13 shows the spectra of SN 2013fs at 0.2–5.3 days after the explosion (Yaron et al., 2017). As these spectra show the hydrogen and several high-excitation oxygen emission lines, this object seem to experience the interaction between the SN ejecta and CSM. However, the time interval between the explosion date and the observation date is too short (only several hours). The authors suggest that these emission lines may come not from the direct interaction but from the flash-ionized (FI) CSM.

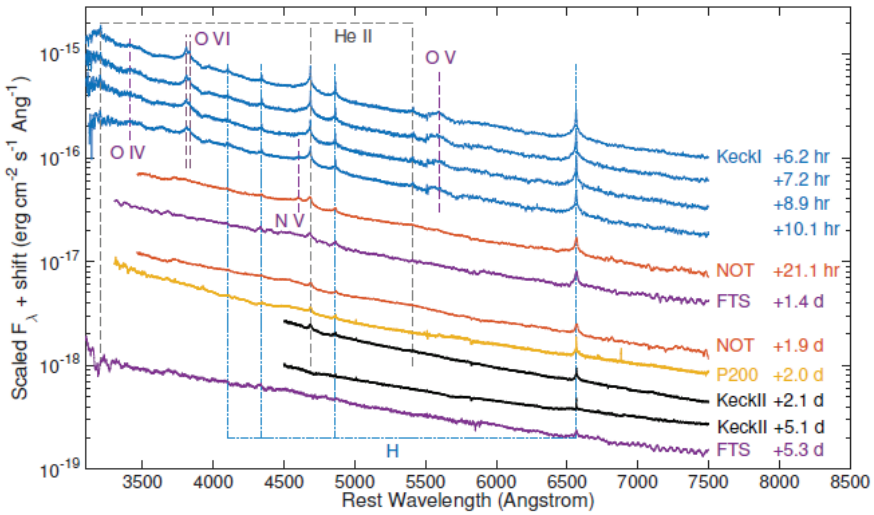

Figure 1.13: The spectra of SN 2013fs at 0.2–5.3 days after the explosion (Yaron et al., 2017).

1.6 Objective in this thesis

CC SNe explode when the massive stars evolve to their final stage in the evolutionary path. For the progenitors of SNe II, any strong mass loss is not predicted in the theoretical studies of stellar evolutions. Recently, the interaction signature between the SN ejecta and the CSM is found through the prompt follow-up observations to some SNe. The observational facts suggest that there is a local CSM surrounding the progenitor, indicating that the strong wind is temporally ejected just before the SN explosion. Their properties are poorly understood. Currently, high-cadence wide-field survey have been developed and discoveries of SNe just after the explosion are realized. We performed prompt observations in optical and near-infrared wavelengths using 1.5-m Kanata telescope. We also carried out the spectroscopic observations at the early stage. We found a few supernova which shows the sign of interaction. In this thesis, we present the observational properties, e.g., light curves, of these SNe. We also discuss the explosion and progenitor properties in comparison with theoretical studies.

Chapter 2

Observation and Data Reduction

In this thesis, we use the observational data of SNe mainly taken with Kanata telescope in Higashi-Hiroshima Observatory, Japan and the *Swift* satellite. In this Chapter, we describe these observational facilities, how to reduce the data, and how to derive the observational results.

2.1 Kanata Telescope

Kanata telescope is fifth largest optical telescope in Japan and located at 34.3 degrees north in latitude and 132.7 degrees east in longitude. It was relocated from the National Astronomical Observatory of Japan to the Higashi-Hiroshima Observatory in 2005–2006, and has been continuously operated thereafter. Figure 2.1 is the exterior view of the Higashi-Hiroshima Observatory and Kanata telescope. Higashi-Hiroshima Observatory is placed in 20 minutes by car from Hiroshima University, and it is easy to maintain the dome, telescope and its instruments. Table 2.1 is the specifications of Kanata telescope. One of the characteristics of Kanata telescope is the world-class mobility in the 1-m class telescopes. Using this mobility, we are focusing on the observation of transient objects including gamma-ray bursts. As Kanata telescope is owned by Hiroshima University, we have plenty of observation time. Thus, this telescope is good for monitoring and long-term observation; e.g., for bright SNe.

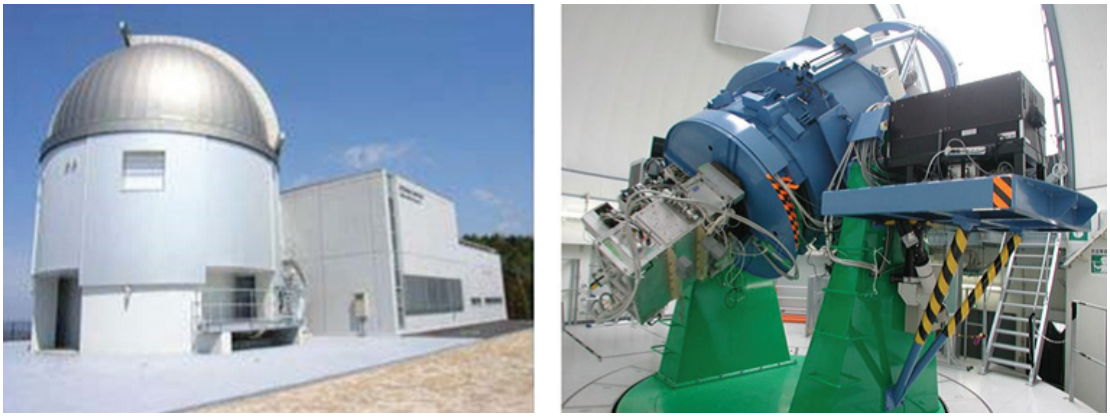

Figure 2.1: (Left)The exterior view of the Higashi-Hiroshima Observatory. (Right)Kanata telescope [2]

Table 2.1: The specifications of Kanata telescope [3]

Item	Value
Telescope optics	Ritchey-Chretien
Diameter of a main mirror	1500 mm
F-value	F/12.3
Focal length	18501.7 mm
Field of view	15 arcmin
Size of focal	11.148 arcmin/mm
Operating speed (max)	5 deg./sec. (azimuth axis) 2 deg./sec. (altitude axis)
Load available (max)	500 kg (Cassegrain) 1000 kg (Nasmyth)

At present (January 2019), the Kanata telescope has the following instruments attached.

- HOWPol (Hiroshima One-shot Wide field Polarimeter)
- HONIR (Hiroshima Optical and Near-InfraRed camera)
- High-Speed CAMera

In this section, HOWPol and HONIR used for our observations of SNe are explained in detail.

2.1.1 HOWPol

HOWPol (Hiroshima One-shot Wide-field Polarimeter) is an instrument that is installed on the first Nasmyth focus of Kanata telescope. This instrument is mainly used for observations in the optical bands. Since the first light of this instrument was done in 2008, it has been used steadily as one of the main instruments in Kanata telescope. Figure 2.2 is the overview of

[2]http://www.hiroshima-u.ac.jp/hasc/institution/hho_kanata/
[3]http://www.hiroshima-u.ac.jp/hasc/institution/telescope/abstract

HOWPol attached to the Kanata telescope. Table 2.2 shows the specifications of HOWPol. The CCD used for HOWPol is a fully depleted one, and has excellent sensitivity in redder region (800–1000 nm). Therefore, HOWPol has I- and z-band filters as well as traditional B-, V- and R-band ones. The transmittance of these filters is shown in Figure 2.3.

In this thesis, we obtained the data of optical imaging and spectroscopy using HOWPol.

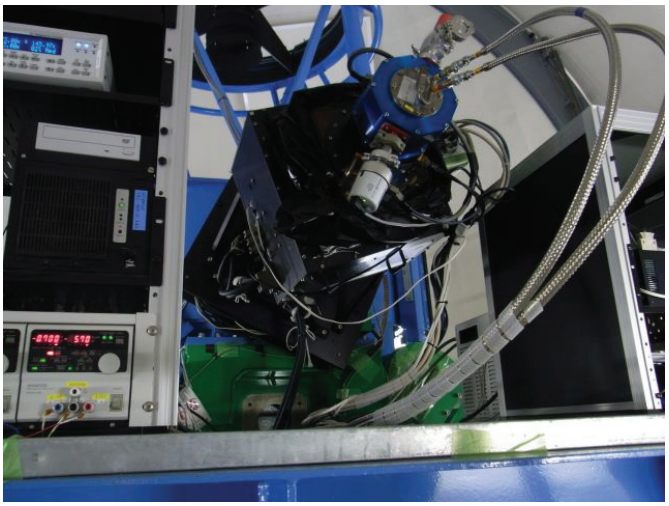

Figure 2.2: HOWPol attached to Nasmyth focus of Kanata telescope [4]

Table 2.2: Specification of HOWPol [5]

Item	Value
Wavelength range	0.45–1 μm
Field of view	15 arcmin (image)
	2.3 arcsec×15 arcmin (spec.)
Filter	B, V, R, I, z
Grism	420/mm R=400
Detector	fully depleted CCD 2k-4k×2
Final F-value	F/6.9

[4] http://hasc.hiroshima-u.ac.jp/instruments/howpol/
[5] http://hasc.hiroshima-u.ac.jp/instruments/howpol/

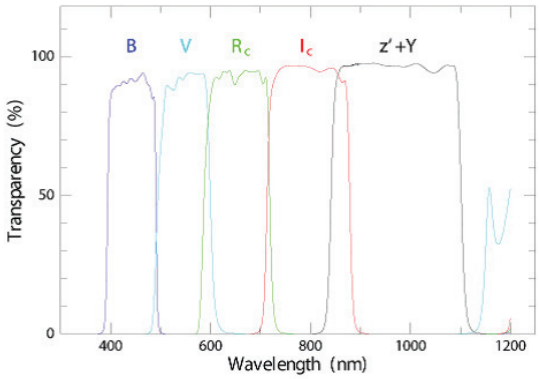

Figure 2.3: The transmittance of the filters mounted in HOWPol[6]

2.1.2 HONIR

HONIR (Hiroshima Optical and Near-InfraRed camera) is an instrument enabling simultaneous observations in optical to near-infrared (NIR) bands, installed at the Cassegrain focus of Kanata telescope. The test observations with HONIR started in 2011. At present (January 2019), HONIR is the most used instruments in Kanata telescope. Figure 2.4 is the overview of HONIR attached to Kanata telescope. The specifications of HONIR are shown in the Table 2.3. The greatest feature of HONIR is the simultaneous observation of the optical and the NIR bands. This is not only shortens the observation time but also leads to increase the time resolution. In addition, the various observation mode is one of the features of HONIR. Especially, the all-time polarimetric capability in the NIR is rare in the world.

In this thesis, we obtained the data of optical and NIR imaging using HONIR.

[6]http://hasc.hiroshima-u.ac.jp/instruments/howpol/

Figure 2.4: The appearance of HONIR attached to Cassegrain of Kanata telescope[7]

Table 2.3: Specifications of HONIR[8]

Item	Optical	NIR
Wavelength	0.5–1 μm	1.15–2.4 μm
Field of view	10 arcmin	10 arcmin
Available Filter	B, V, R, I, Y	Y, J, H, Ks
Detector	fully depleted CCD 2k-4k	HgCdTe VIRGO 2k-2k

2.2 *Swift* Satellite

Swift satellite is a spacecraft that NASA launched on November 20, 2004. It can observe in a wide band from optical to gamma ray. The main mission of the *Swift* satellite is observation of gamma-ray bursts. The characteristic of the data obtained by the *Swift* satellite is that the timescale from observation to the data delivery is quite short. The obtained data usually uploaded on-line archive in about 1–2 weeks. Instruments mounted on the *Swift* satellite are a wide range gamma-ray detector (BAT: Burst Alert Telescope), an X-Ray Telescope (XRT), and an UltraViolet and Optical Telescope (UVOT). Although these instruments are installed for the purpose of observing gamma-ray bursts, other objects are performed when the gamma-ray bursts do not appear. The data of SNe in this thesis is obtained as such ToO observation.

[7]http://hasc.hiroshima-u.ac.jp/instruments/honir/
[8]http://hasc.hiroshima-u.ac.jp/instruments/honir/

The UVOT is described in detail below.

2.2.1 UVOT

To observe the ultraviolet and optical lights from the objects, the UVOT is attached to the *Swift* satellite. Summarize the specifications of the UVOT in Table 2.4. Since the aperture of the main mirror is only 30 cm, the spatial resolution is inferior to those of the large telescopes on the ground. But it is a great merit that it can be observed without the influence of the atmosphere because of the space telescope. With this merit, it is possible to observe the ultraviolet (UV) around 2000 Åwith high efficiency. Table 2.5 summarizes the information on the filters installed in the UVOT. The UV filters are $uvw2$, $uvm2$ and $uvw1$, and these wavelengths are beyond the accessible one by the ground telescope. The UVOT also has optical filters, u, b and v, but we need to be careful to use the data because the specification e.g., function of the filter transmission is slightly different from the typical B- and V-bands. Figure 2.5 shows the transmittance of each filter installed on the UVOT.

In this thesis, the archive data of UV and optical observation for the target SNe were used.

Table 2.4: The specifications of the UVOT[9]

Item	Value
Telescope system	Ritchey-Chretien
Diameter of a main mirror	300 mm
F-value	12.7
Field of view	17 arcmin
Seeing size	2.5 arcsec

Table 2.5: The information of the filters installed in the UVOT[10]

Filter	Center wavelength of the filter(Å)
v	5402
b	4329
u	3501
uw1	2591
um2	2229
uvw2	2033

[9] http://swift.gsfc.nasa.gov/about_swift/uvot_desc.html
[10] http://heasarc.gsfc.nasa.gov/docs/heasarc/caldb/swift/docs/uvot/index.html

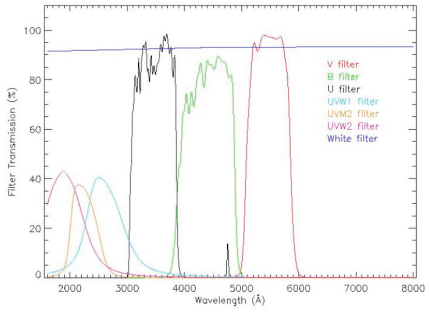

Figure 2.5: The function of the filter transmission installed on the UVOT [11].

2.3 Data Reduction

Observation of SNe using the instruments described in the previous chapter are performed. The obtained images are generally affected by the characteristics of the instruments. Therefore, we need correction and calibration for them. If the calibration is performed wrongly, it increases the systematic errors. By appropriately calibrating the obtained data, it is possible to minimize the error. In this section, we describe the calibration data, the calibration method and how to measure the flux from the target object. IRAF (Tody, 1986, 1993) as used for these calibration and measurement.

2.3.1 Calibration and Correction

Assuming that there are data of the target object and standard star to calibrate the flux of the target object. These images contain not only the radiation from the objects, but also the effects of the characteristics of the instruments, the inhomogeneity of the sensitivity, and the radiation from other sources. These components are mixed like in Figure 2.6. As it is impossible to obtain the correct flux from the target object directly, the correction need using the calibration data.

[11] http://heasarc.gsfc.nasa.gov/docs/heasarc/caldb/swift/docs/uvot/index.html

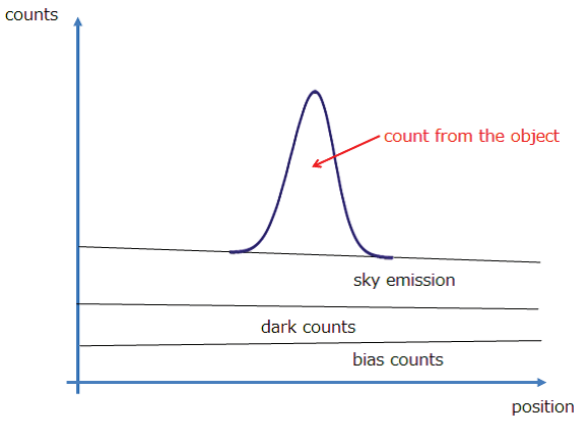

Figure 2.6: The components of the data

2.3.2 Calibration Method

In this subsection, we describe the primary calibration process which is commonly performed for both photometry and spectroscopic data.

Subtraction of bias

When reading the photo-electric charges from the detector, the bias voltage is added. Since this signal is recorded in the image as a count (ADU; analog-to-degital unit), even in cases that no light is illuminated to the detector, constant signal is recorded. This signal or value is called a bias. Since the bias applied to the detector does not change greatly in a day, it can be considered that the bias pattern obtained in the same day is constant. Therefore, the bias images read from the detector with zero seconds exposure are obtained in the same day. The averaged bias image is subtracted from the image of the target object.

Overscan-region

In a large format CCD, the bias signal level slightly changes during the readout, and gives random slopes or stripe patterns and affect the measurement. To follow the bias variation, the overscan regions are artificially added in the obtained images.

Since this part is not for the sensitive pixels in the detector, it is necessary to cut it from the image. This region is called “overscan-region”. The counts in the overscan region corresponds to the bias at the time of the readout of the same lines. Therefore, a subtraction of the average value in each line of the overscan-region from the image makes the further correction of the bias signals. This process is performed for all images.

Flatfielding image

Ideally, the detector should have the same sensitivity for all pixels, but actual detectors are not ideal: e.g., bad pixels (very poor sensitivity) or hot pixels (very high dark signal) exist and dust

particles on the windows at the entrance of the instrument makes partial obstruction of the incident light. For the reasons listed above, the sensitivity of the detector is inhomogeneous. Therefore, we obtain the image applying the uniform light into the telescope (using defocused artificial light), the sensitivity pattern of the detector is derived and it is used for the correction of the sensitivity inhomogeneity. This image is called a flat image.

Bad pixel collection

In general, the number of bad pixels in an infrared detector is larger than that of a CCD because of the fabrication from heterogeneous materials. There is a possibility that the count in the bad pixels have a large uncertainty. When the image obtained by the infrared detector is processed, the pixel value of the bad pixel is overwrote by the counts of surrounding pixels.

Sky subtraction

One of the noise for the astronomical objects is the sky brightness. In the optical bands, sunlight or moonlight are dominant, but these are not a big problem unless we obtain the data of target objects near the sun and the moon. However, in the near-infrared bands, the sky itself is much brighter than in optical, so sky brightness dominates in any long exposure. Considering that the sky brightness does not fluctuate greatly in a short time, it is possible to subtract a sky brightness by taking multiple images of the same target object with different pointing. Therefore, a method called "dithering" is often used for observations in the near-infrared bands. In this thesis, we obtained all data of the SNe in the near-infrared bands using dithering method.

Emission from the host galaxy

SNe occur on or near the galaxies with high probability. Especially in low-luminous cases or in late phases, there are some brighter sources than SNe, such as bulge and H II region. The SNe are contaminated by these components. Therefore, by subtracting the host galaxy template image taken before the SN occurs after the SNe has become sufficiently invisible, it is possible to remove the components of the host galaxy.

2.3.3 Photometry

Aperture photometry

One of the method to measure the object flux from the object is an aperture photometry. The aperture photometry is a method of determining the flux of the object by summing of the counts within a certain range from the center of the object. The profile from the object is approximately represented by Gaussian distribution. Since the full width at half maximum (FWHM) varies depending on the observation conditions, the range for aperture needs to be changed for each image. On the basis from the counts obtained by aperture photometry, the magnitude of the object is determined.

PSF photometry

The other method to measure the object flux is a Point-Spread-Function (PSF) photometry. PSF photometry is a method of determining the brightness of the objects by modeling a matched function of the two-dimensional distribution of the counts and integrating the function. The aperture photometry is sufficient to measure the brightness of the objects, but if the profile of the object is affect by the contamination from other emission, e.g., the host galaxy, those counts are wrongly affect the result. By using PSF photometry, we can avoid or minimize the ill effects from the other emission. In many cases, there are bright galaxies around the SNe. PSF photometry is often more advantageous than the aperture photometry.

2.3.4 Spectroscopy

The way to get the spectral information of the lights from the objects is spectroscopy. With spectroscopy, we can investigate the flux distribution against the wavelength by decomposing the emission from the objects in the detector. In the observation of SNe, by getting the spectra, it is possible to classify the type of SNe. And, by measuring the width or the wavelength shift of the absorption lines, the expansion velocity of the supernova can be derived.

2.4 Observation

We show the list of observations of SNe in Table 2.6. All the listed SNe are SNe II that we observed by ourselves with Kanata telescope except for *Swift* / UVOT.

Table 2.6: The number of the nights of the observational data in this thesis

SN name	Obs. start (date)	Obs. end (date)	Imaging (howpol) (epoch)	Imaging (HONIR) (epoch)	Spec. (HOWPol) (epoch)	Imaging (UVOT) (epoch)
SN 2014cx	2014/09/08	2015/12/01	75	23	21	—
SN in NGC 3430	2015/09/28	2017/10/30	21	12	11	—
SN in UGC 11000	2015/04/08	2015/12/01	43	20	15	—
SN 2015ah	2015/08/07	2016/07/04	28	9	3	—
SN 2015aq	2015/09/21	2017/01/03	24	7	9	—
SN 2015bf	2015/12/14	2016/12/17	12	8	13	—
SN 2016B	2016/01/04	2017/02/28	15	16	33	8
SN 2016C	2016/01/04	2016/02/04	3	3	2	—
SN 2016X	2016/01/26	2017/02/28	26	16	29	27
SN 2016bkv	2016/03/24	2018/01/11	28	20	21	—
SN 2016bmf	2016/04/15	2017/02/02	22	2	0	—
SN 2016cok	2016/05/28	2017/02/27	18	7	7	14
SN 2016gfy	2016/10/05	2017/12/17	24	4	5	—
SN 2017bgu	2017/02/24	2018/02/04	32	15	14	—
SN 2017cjb	2017/03/28	2018/01/12	18	9	17	—
SN 2017czd	2017/04/13	2018/08/07	31	9	19	—
SN 2017eaw	2017/05/14	2018/06/16	109	66	3	29
SN 2017gkk	2017/08/24	2018/06/02	28	2	0	—
SN 2017hcc	2017/11/08	2018/07/09	16	7	0	—
SN 2018gv	2018/01/17	2018/05/14	14	8	0	2
SN 2018gj	2018/01/17	2018/07/09	30	8	1	—
SN 2018zd	2018/03/10	2018/08/07	27	17	2	—
SN 2018aoq	2018/04/01	2018/08/07	20	13	2	3

Chapter 3

Results

In this chapter, we explain the observational characteristics of the objects picked up in Section 2.4, especially of the outstanding features in light curves and spectra. They will be discussed in Chapter 4 from the viewpoint of the link between the SN explosion and the CSM.

3.1 SN 2016bkv

In this section, we present the observational characteristics of the SN 2016bkv.

3.1.1 Discovery and Host Galaxy

SN 2016bkv was discovered by Koichi Itagaki on 2016 Mar 21.7 (UT) (Itagaki, 2016). At two days after the discovery, this SN was classified as an SN II by the spectral similarity to SN IIn 1998S (Hosseinzadeh et al., 2016). The host galaxy, NGC 3184, is a face-on spiral galaxy and known to be an active SN factory in the last 100 years (i.e., SNe 1921B, 1921C, 1937F and 1999gi have been found in NGC 3184; Leonard et al. 2002b). The distance to the host galaxy is assumed to be 12.3 ± 2.2 Mpc, adopting the mean redshift-independent distance reported in the literatures (via NED[1]). The explosion date is assumed to be 2016 Mar 20.4 ± 1.3, as constrained by the last non-detection date (Mar 19.1) by Katzman Automatic Imaging Telescope (KAIT). Throughout the paper, the observation epoch is given with respect to the estimated explosion date. Hosseinzadeh et al. (2018) presented optical light curves and spectra of SN 2016bkv, and discussed the nature of the explosion and progenitor using models of nebular spectra.

3.1.2 Host Extinction

In our photometric data of SN 2016bkv, shown in Figure 3.1, the Galactic extinction of $E(B-V) = 0.0144$ (Schlafly & Finkbeiner, 2011) along the direction toward the SN has been corrected for. We also derive an upper limit of the total extinction as $E(B-V) \lesssim 0.015$ by using the equivalent width of Na I D absorption line (Poznanski et al., 2012) in our stacked spectrum (EW $\lesssim 0.065$ Å). Since the Galactic extinction is close to the upper limit of the total extinction, We

[1] http://ned.ipac.caltech.edu/

consider that the interstellar extinction within the host galaxy is negligibly small ($E(B-V) \lesssim 0.005$).

3.1.3 Photometry

Our photometric results in SN 2016bkv are shown in Figure 3.1, Table 3.1 and Table 3.2. These data are obtained by using HOWPol in 10 nights from 2016 Apr 5.3 until Oct 9.4, and using HONIR in 14 nights from Mar 24.3 until Aug 9.1. All magnitudes are given in the Vega magnitudes throughout the thesis. For the calibration of optical photometry, we used the magnitudes of a nearby comparison star given in Leonard et al. (2002b) (see Figure 3.2).

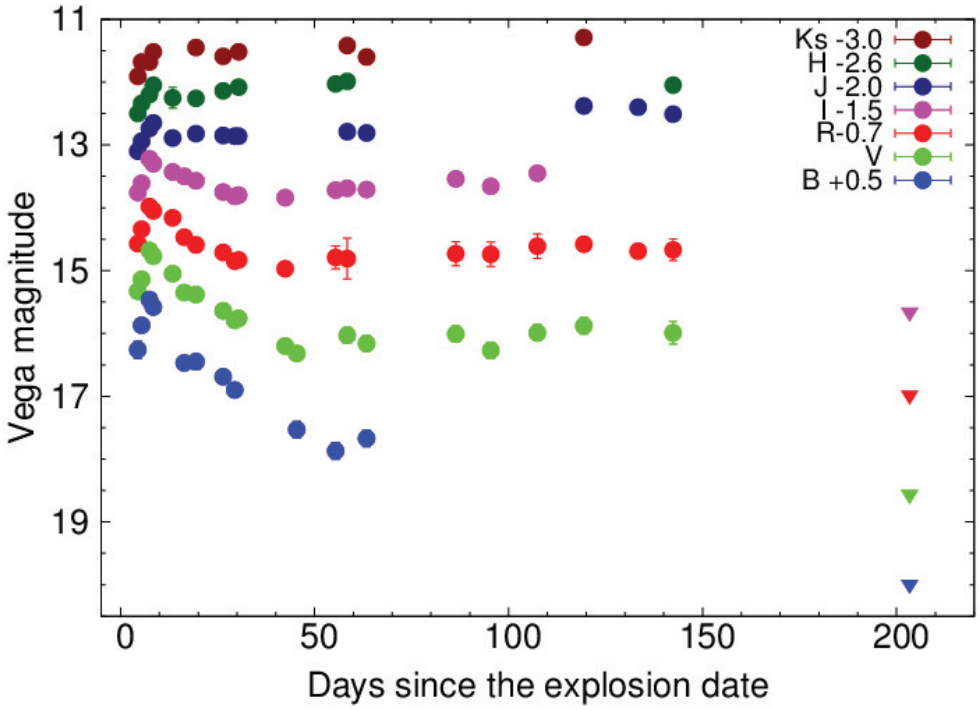

Figure 3.1: Optical to NIR light curves of SN 2016bkv. The Galactic interstellar extinction (Schlafly & Finkbeiner, 2011) has been corrected for. The host-galactic extinction is estimated to be negligible (see Section 3.1.2) and therefore no correction has been made.

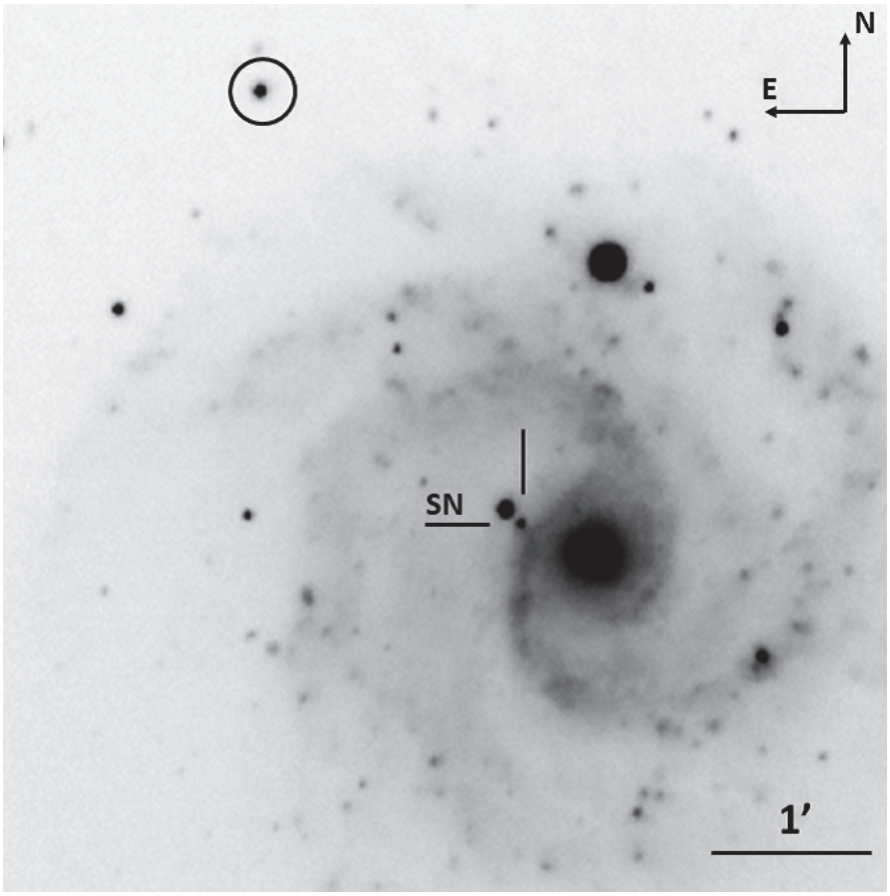

Figure 3.2: *R*-band image of SN 2016bkv in NGC 3184 taken using HOWPol. The location of SN and comparison star (Leonard et al., 2002b) are marked.

Table 3.1: Photometric observations of SN 2016bkv in optical bands.

MJD	Epoch (day)	B (mag)	V (mag)	R (mag)	I (mag)	Instrument
57471.7	4.4	15.76(0.13)	15.33(0.08)	15.27(0.04)	15.26(0.04)	HONIR
57472.7	5.4	15.37(0.07)	15.14(0.06)	15.04(0.04)	15.11(0.04)	HONIR
57474.7	7.4	14.96(0.05)	14.68(0.04)	14.68(0.04)	14.72(0.04)	HONIR
57475.7	8.4	15.08(0.04)	14.77(0.05)	14.75(0.04)	14.80(0.05)	HONIR
57480.7	13.4	—	15.05(0.05)	14.86(0.04)	14.93(0.08)	HONIR
57483.6	16.3	15.97(0.04)	15.35(0.05)	15.17(0.04)	15.0(0.08)	HOWPol
57486.6	19.3	15.95(0.11)	15.38(0.05)	15.29(0.11)	15.07(0.05)	HONIR
57493.6	26.3	16.19(0.04)	15.64(0.05)	15.41(0.05)	15.25(0.05)	HONIR
57496.7	29.4	16.40(0.08)	15.79(0.07)	15.55(0.07)	15.32(0.04)	HONIR
57497.7	30.4	—	15.76(0.06)	15.53(0.04)	15.30(0.04)	HONIR
57509.7	42.4	—	16.2(0.06)	15.67(0.04)	15.34(0.04)	HOWPol
57512.6	45.3	17.03(0.13)	16.32(0.06)	—	—	HOWPol
57522.6	55.3	17.37(0.13)	—	15.49(0.18)	15.22(0.06)	HONIR
57525.6	58.3	—	16.03(0.12)	15.51(0.32)	15.19(0.05)	HONIR
57530.6	63.3	17.17(0.13)	16.16(0.12)	—	15.21(0.08)	HONIR
57553.6	86.3	—	16.01(0.12)	15.43(0.19)	15.04(0.08)	HOWPol
57562.5	95.2	—	16.27(0.12)	15.44(0.19)	15.16(0.08)	HOWPol
57574.5	107.2	—	15.99(0.12)	15.31(0.19)	14.95(0.08)	HOWPol
57586.5	119.2	—	15.88(0.13)	15.28(0.04)	—	HONIR
57600.5	133.2	—	—	15.39(0.07)	—	HONIR
57609.5	142.2	—	15.99(0.18)	15.37(0.17)	—	HONIR
57670.8	203.5	19.49(0.13)	18.56(0.18)	17.68(0.17)	17.16(0.08)	HOWPol

Table 3.2: Photometric observations of SN 2016bkv in NIR bands.

MJD	Epoch (day)	J (mag)	H (mag)	Ks (mag)
57471.7	4.4	15.1(0.02)	15.1(0.03)	14.91(0.03)
57472.7	5.4	14.94(0.02)	14.94(0.03)	14.68(0.03)
57474.7	7.4	14.74(0.02)	14.8(0.03)	14.68(0.03)
57475.7	8.4	14.65(0.02)	14.65(0.03)	14.52(0.04)
57480.7	13.4	14.89(0.04)	14.85(0.16)	—
57486.6	19.3	14.82(0.02)	14.86(0.05)	14.45(0.07)
57493.6	26.3	14.85(0.03)	14.74(0.03)	14.59(0.04)
57496.7	29.4	14.86(0.02)	—	—
57497.7	30.4	14.86(0.02)	14.68(0.03)	14.52(0.04)
57522.6	55.3	—	14.63(0.05)	—
57525.6	58.3	14.79(0.05)	14.59(0.02)	14.42(0.06)
57530.6	63.3	14.81(0.04)	—	14.6(0.08)
57586.5	119.2	14.38(0.04)	—	14.29(0.08)
57600.5	133.2	14.4(0.04)	—	—
57609.5	142.2	14.51(0.03)	14.65(0.06)	—

3.1.4 Light Curve

Figure 3.3 shows the light curve in absolute R-band magnitude of SN 2016bkv, compared with those of other LL SNe IIP and a normal SN IIP 1999em. For the SNe other than SN 2016bkv, we adopted the estimations of the explosion dates from Pastorello et al. (2004), Fraser et al. (2011) and Spiro et al. (2014). We also adopted the total extinction corrections used in their references. In the mid-plateau phase ($\sim$80 days), the R-band absolute magnitude of SN 2016bkv is $M_R \sim -15.0$ mag. This is $\sim$2 mag fainter than that of the normal SN IIP 1999em. Among LL SNe IIP, SN 2016bkv is $\sim$0.2 mag brighter than SN 2003Z and $\sim$0.5 mag fainter than that of SN 2002gd. SN 2016bkv shows a slight brightening toward $\sim$120 days, reaching the maximum magnitude of $M_R \sim -15.1$ mag.

The length from the explosion to the end of the plateau phase ($\gtrsim$140 days) is later than those of other LL SNe IIP for which the data covering the plateau phase are available; $\sim$110 days in SNe 2003Z and 2009md (Spiro et al., 2014; Fraser et al., 2011). In fact, the epoch of the end of the plateau is still later than that of SN 2009ib (Takáts et al., 2015), which shows the longest plateau length ($\sim$130 days) among normal SNe IIP.

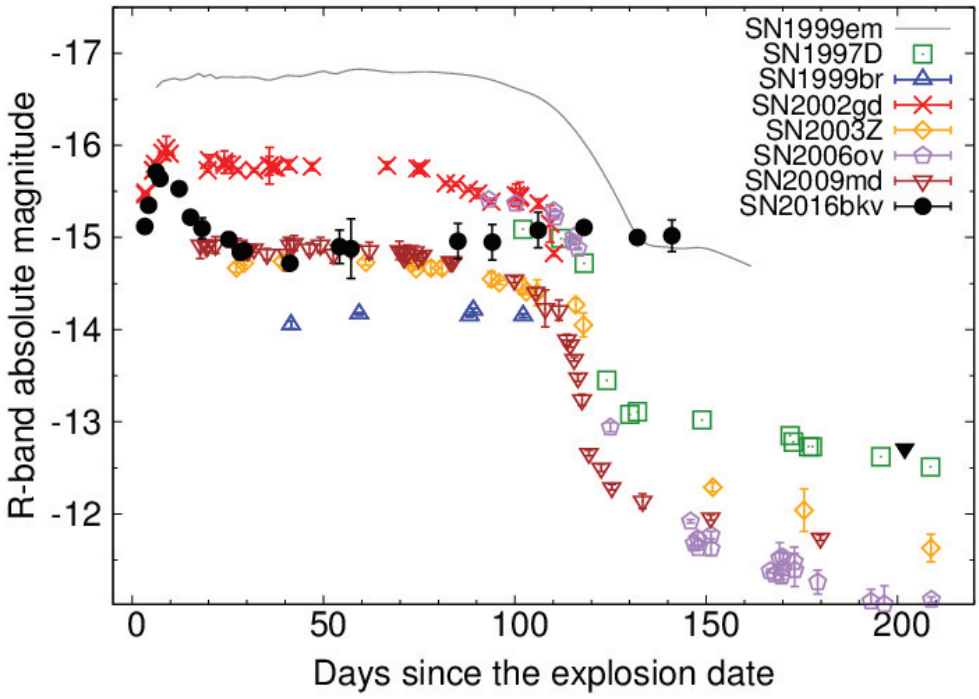

Figure 3.3: The R-band light curve of SN 2016bkv compared with those of other LL IIP SNe 1997D, 1999br (Pastorello et al., 2004), 2002gd, 2003Z, 2006ov (Spiro et al., 2014), 2009md (Fraser et al., 2011) and normal IIP SN 1999em (Leonard et al., 2002a).

3.1.5 Early Bump

SN 2016bkv shows a bump in the early phase. The light curves show a peak at ∼7 days after the explosion (Figure 3.1). At 2–7 days, the SN shows a rapid brightening by about 0.8 mag, 0.65 mag, 0.6 mag and 0.54 mag in the B-, V-, R- and I-band, respectively. Such bumps in the light curves are also seen in the V-band light curve of SN 2002gd (Spiro et al., 2014) and the B-band light curve of SN 2005cs (Pastorello et al., 2009), but the bump in SN 2016bkv is more pronounced. The bump gradually decays (by ∼1 mag through ∼30 days in the R-band) and then the SN seems to enter into the plateau phase. The decay rates between the peak of the bump and the phase of entering the plateau(s_1, as defined by Anderson et al., 2014) are ∼0.043 and ∼0.03 mag day^{-1} in the V-band and R-band, respectively. The amplitudes of the bump and their decay rates are larger in shorter wavelengths (Galbany et al., 2016). Figure 3.4 shows the peak absolute magnitude in the V-band ($M_{\rm max}$) and the decay rate of the bump (s_1) of SN 2016bkv as compared with those of other SNe II (Anderson et al., 2014). The error includes the uncertainty of the distance to the host galaxy and the uncertainty of a transition epoch from the bump into the plateau. From Figure 3.4, it is clear that SN 2016bkv shows the

fastest decay among SNe II having similar peak brightness and LL SNe IIP. We will discuss the features and possible origin of the bump in Section 4.1.

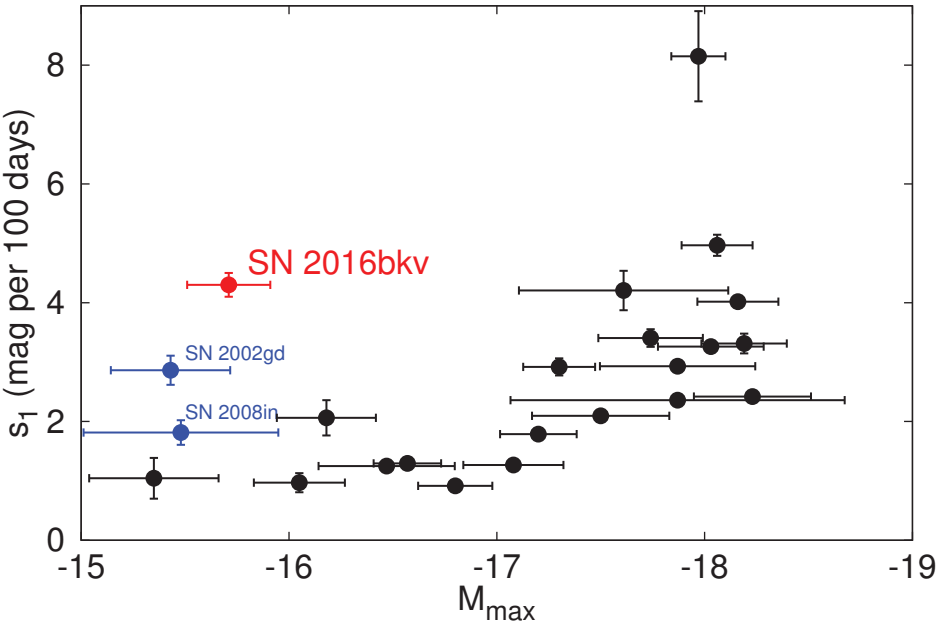

Figure 3.4: Relation between absolute peak magnitudes in the V-band and the decay rates of the initial bumps (s_1) for SN 2016bkv and other SNe II (except for type IIb and IIn). All the data except for SN 2016bkv are taken from Anderson et al. (2014). Blue data are identified as LL SNe IIP (Spiro et al., 2014).

3.1.6 Optical Spectra

We performed optical spectroscopic observations using HOWPol on 17 nights from Mar 24.3 until Jun 26.3. Figure 3.5 shows the spectral evolution of SN 2016bkv from 4 to 98 days, and the log of our spectroscopic observations is shown in Table 3.3. Until 20 days, the spectra are dominated by a blue continuum, superimposed by a weak and narrow ($\sim$1000 km s^{-1}) emission line of Hα (Figures 3.5 and 3.7). After 30 days after the explosion, various absorption lines, e.g., H, Sc II , Fe II , Ba II , Ca II , get stronger with time (Figure 3.5). No significant He I line is seen in the spectra. The identification of the absorption lines of SN 2016bkv are written in the next subsection.

Table 3.3: Spectroscopic observations of SN 2016bkv.

MJD	Epoch (day)	Exposure (sec)
57471.5	4.2	1600
57472.7	5.4	1400
57474.8	7.5	900
57475.6	8.3	1200
57476.7	9.4	1150
57477.7	10.4	1200
57483.6	16.3	1200
57486.5	19.2	1500
57489.5	22.2	1500
57493.5	26.2	1500
57495.6	28.3	1200
57496.6	29.3	2400
57512.7	45.4	1800
57522.6	55.3	1800
57530.6	63.3	2700
57553.5	86.2	2700
57565.5	98.2	2700

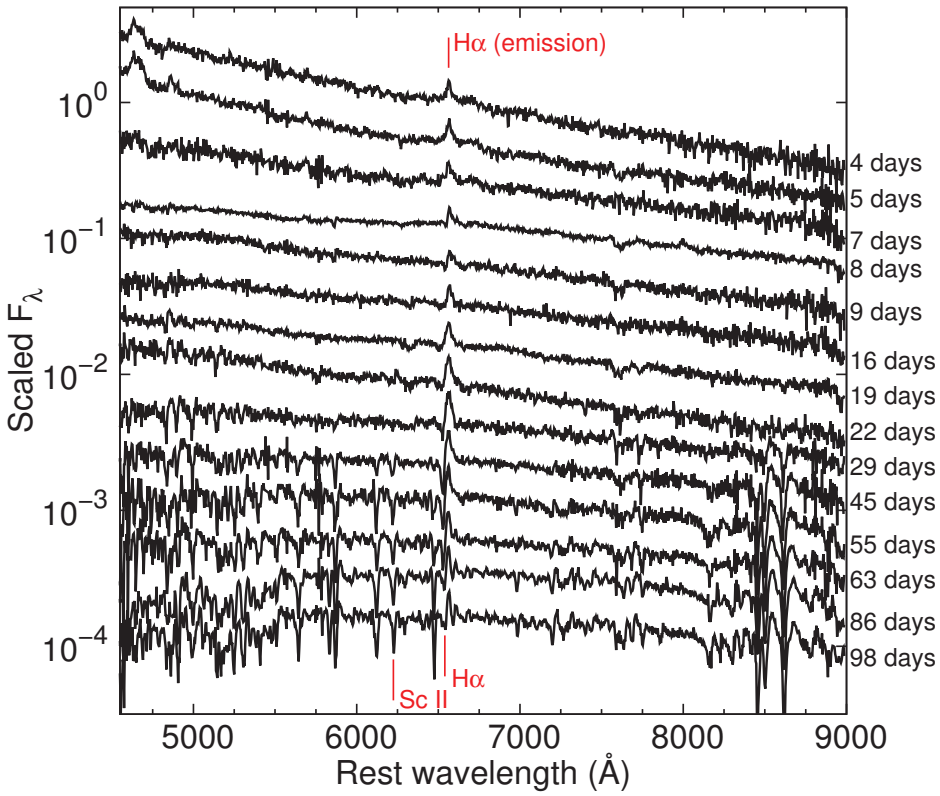

Figure 3.5: Spectral evolution of SN 2016bkv. The epoch of each spectrum is given in the right outside of the panel.

3.1.7 Line Identification

After the end of the initial bump (∼30 days after the explosion), many resolved absorption lines are seen in the spectra (Figure 3.5). Even in LL SNe IIP, the Hα absorption line around 50 days is often affected by Ba II λ6497 because of the slight wavelength difference between Hα and Ba II λ6497 (Roy et al., 2011; Lisakov et al., 2017). However, since the velocity of Hα in SN 2016bkv is slower than that of other LL SNe IIP (see Figure 3.10), the profile of Hα in SN 2016bkv can be clearly isolated from the Ba II λ6497 between 45 and 98 days. Figure 3.6 shows the identification of the absorption lines of SN 2016bkv at 98 days. The identification of other absorption lines is followed by Pastorello et al. (2004).

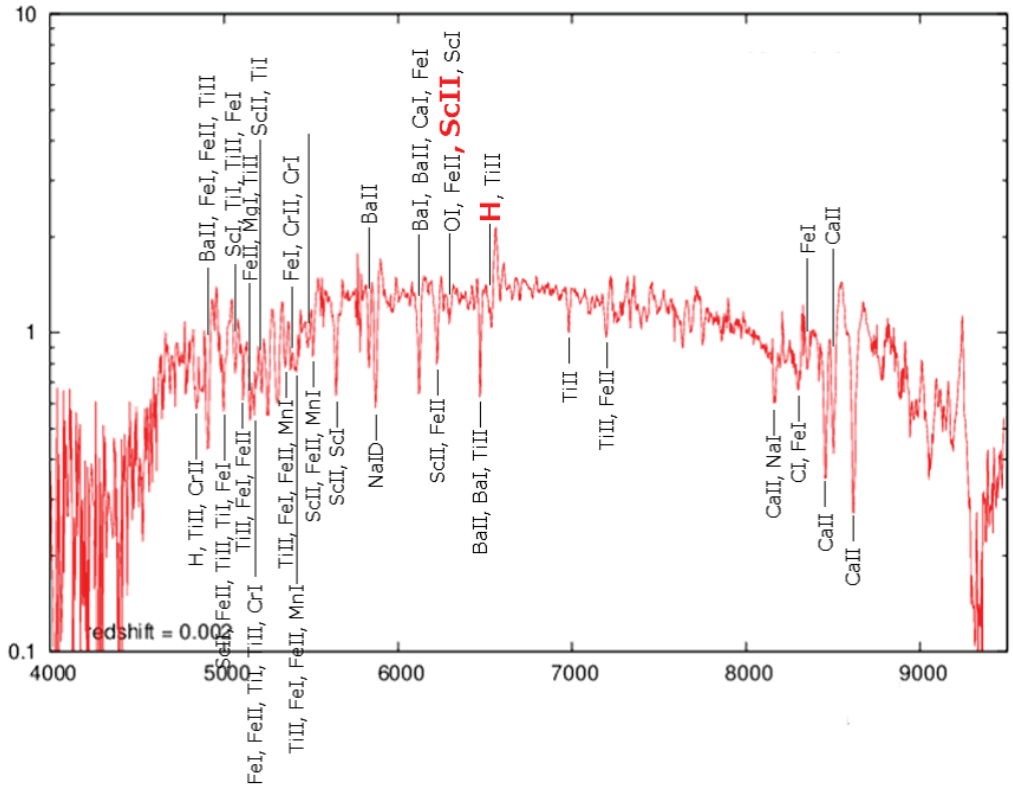

Figure 3.6: The identification of the absorption lines of SN 2016bkv at 98 days. This identification is followed by Pastorello et al. (2004).

3.1.8 Early Phase Spectra

Although the overall spectral properties of SN 2016bkv are similar to other LL SNe IIP, SN 2016bkv shows some remarkable features in the earliest phases (Hosseinzadeh et al., 2018, ,see Figure 3.7). The Hα emission line at 4 days is narrower than in other LL SNe IIP, with a possible asymmetric profile truncated at a redder side, and there is no clear absorption component (see Figure 3.5). At 8–9 days, a possible weak absorption component in the bluer side of the Hα is marginally visible (The details will be described in Section 4.1). After ∼9 days, the absorption component gradually develops (Figure 3.5). All of these properties are quite different from those in well-observed LL SNe IIP 2002gd, 2003Z and 1999br (see Figure 3.7), which show clear P Cygni profiles in Hα (and Hβ) at these epochs with larger line velocities.

Narrow Balmer emission lines with a blue continuum are sometimes seen in SNe II at their early phases. Figure 3.8 shows the spectral comparison of SN 2016bkv with other SNe II showing narrow emission lines and a blue continuum at 0–8 days. In fact, the overall features of SN 2016bkv match well to those of SN IIn 1998S (Fassia et al., 2001), whose spectra show the emission lines of Hα and Hβ , and also the emission lines around 4600 Å (a blend of highly-excitation lines of C III , N III and He II ; Shivvers et al. 2017). As also shown in Figure 3.8, similar emission features are seen in SNe 2009aj and 2009au at similar epochs (Gutiérrez

et al., 2017). The similarity is also found to SN 2013fs (iPTF13dqy; Yaron et al., 2017), as the spectrum was observed much earlier since the explosion. Given the epochs when these spectra are obtained, the emissions from SNe 2009aj and 2009au may be powered by the CSM interactions, while those of SN 2013fs are suggested to be flash ionized (FI; where the optical flash at the initial explosion ionizes the CSM) features (Gal-Yam et al., 2014). We discuss the origin of these features from a viewpoint of possible CSM-ejecta interaction in Section 4.1 and Section 4.3.

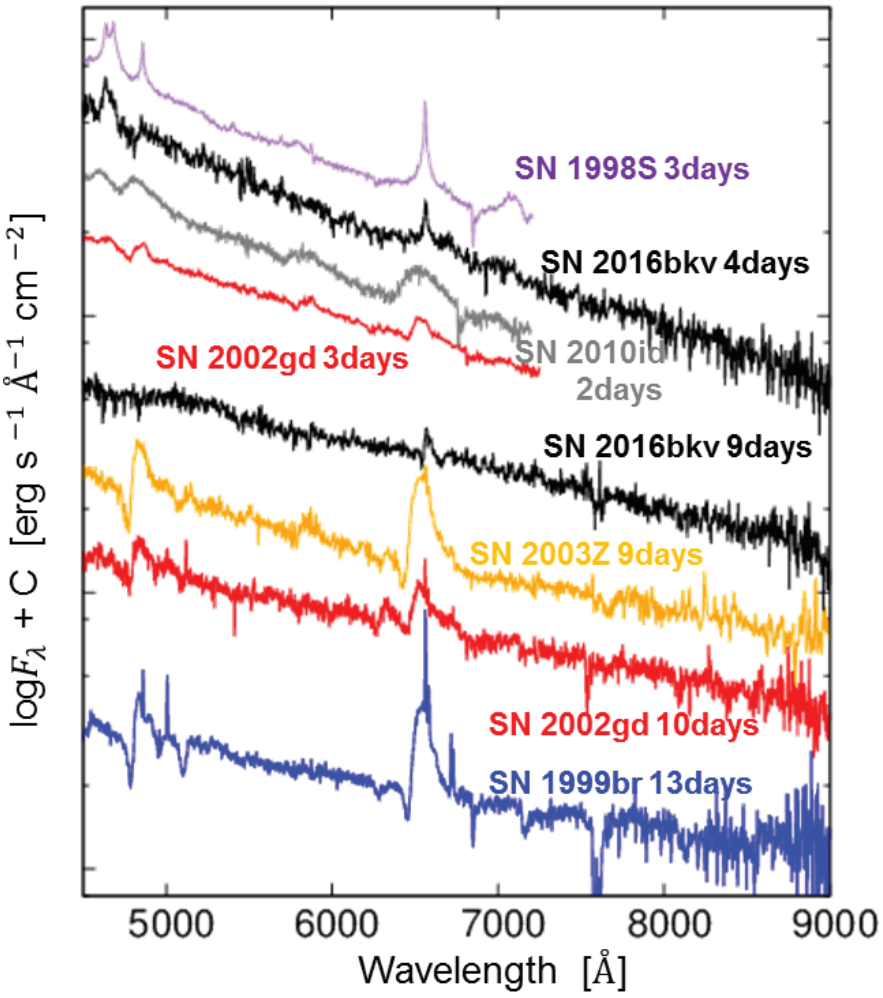

Figure 3.7: Spectra of SN 2016bkv in the early phase, compared with LL SNe IIP 2002gd, 2003Z (Spiro et al., 2014), 1999br (Pastorello et al., 2004) and IIn 1998S (Fassia et al., 2001) at similar epochs. The fluxes are shown in the logarithmic scale and arbitrarily scaled to avoid overlaps.

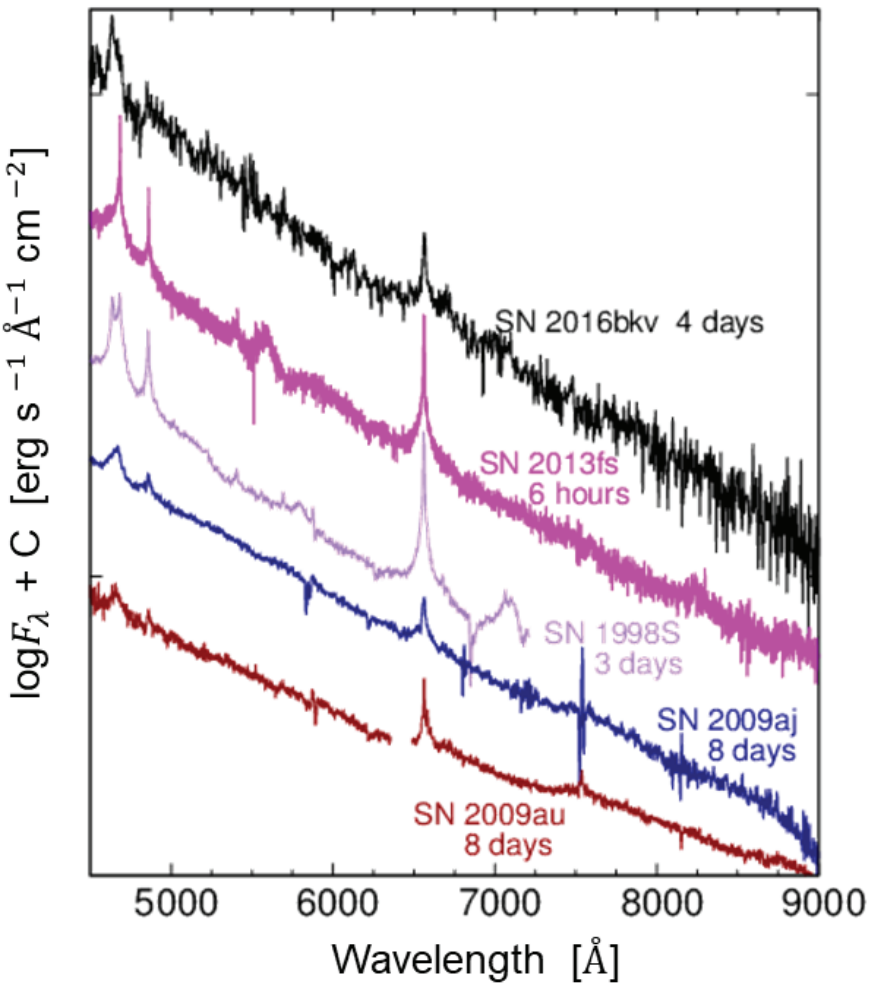

Figure 3.8: Spectrum of SN 2016bkv at 4 days in comparisons with those of SNe 1998S (Fassia et al., 2001), 2009aj, 2009au (Gutiérrez et al., 2017) and 2013fs (Yaron et al., 2017) at their earliest phases (0.3–8 days).

3.1.9 Late Phase Spectra

In Figure 3.9, we compare the spectra of SN 2016bkv with those of LL SNe IIP at around 100 days. At this epoch, the overall spectral features are similar to those in other LL SNe IIP, although SN 2016bkv shows slightly narrower features than others. At this epoch, SN 2016bkv shows a complicated structure of the Hα line, which is also seen in other LL SNe IIP. These facts confirm our classification of SN 2016bkv as LL SN IIP.

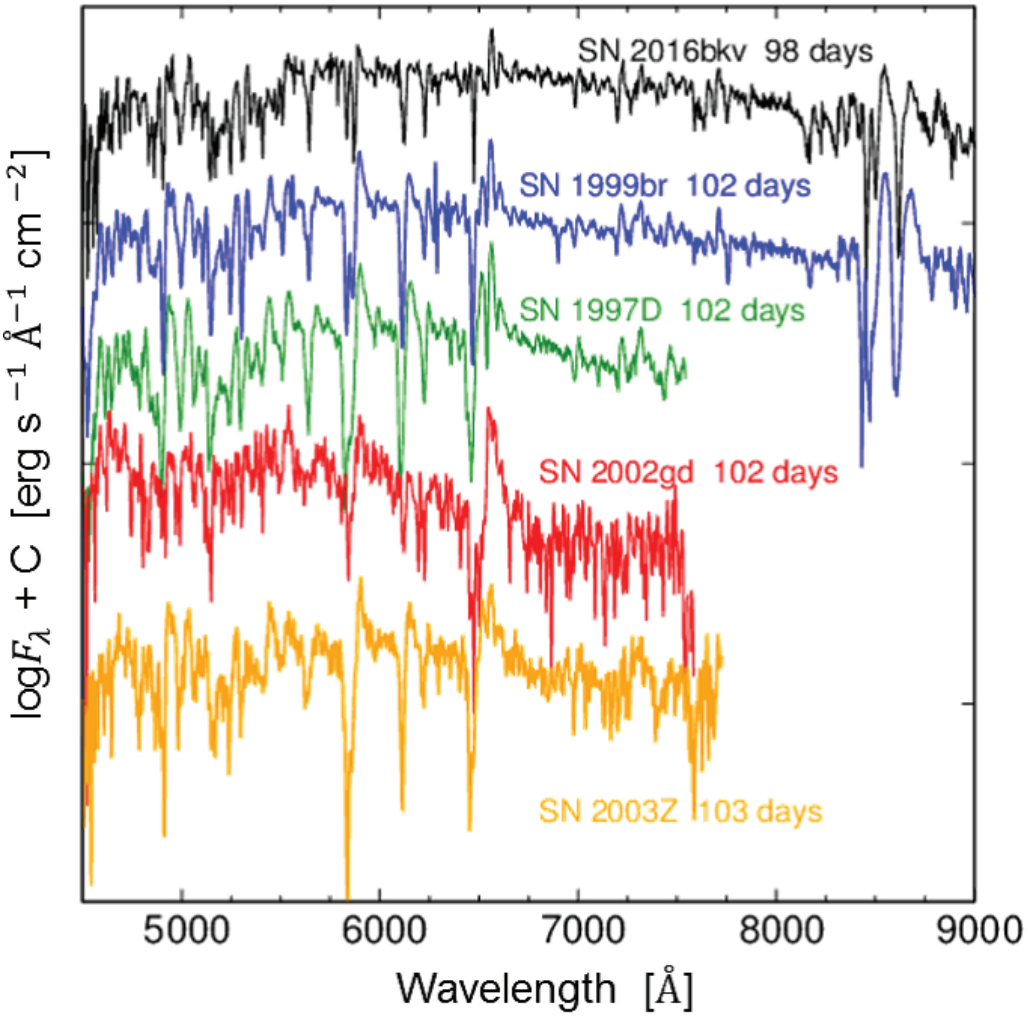

Figure 3.9: Spectra of SN 2016bkv at 98 days in comparison with the spectra of LL SNe IIP 1999br, 1997D (Pastorello et al., 2004), 2002gd and 2003Z (Spiro et al., 2014) at similar epochs (near the end of the plateau phase).

3.1.10 Line Velocity of Hα

Since the absorption component of the Hα feature is not so narrow, the line velocities were measured by fitting a Gaussian function to the absorption component. The difference between the rest wavelength and the wavelength at the minimum of the fitting function is assumed to be the line velocity. Figure 3.10 shows the line velocity evolutions of various absorption lines: Hβ , Fe II λ5169, Na I D, Sc II λ6246, Ba II λ6497, Hα and Ca II λ8662. When we compare the different lines created by the same element at the same ionization state, the velocities and their evolutions should be mutually consistent (e.g., Ca II NIR triplet). Thus, only representative line velocities are shown in Figure 3.10. The velocities are about 1,600–2,000 km s^{-1} at 22 days and decreases to 1,000–1,600 km s^{-1} at 85 days. The Sc II and Na I D lines exhibit one of the

lowest velocities among these lines. In normal SNe IIP (e.g., SN 1999em), the Hα line velocities are always higher than the velocities of other elements (Leonard et al., 2002a). This trend is, however, not necessarily true for LL SNe IIP. For example, the faster line velocity is observed for the Ca IR triplet and Fe II than the Hα in SN 2008in at 60-100 days after the explosion (Roy et al., 2011). Similarly, in SN 2016bkv, the Ca IR triplet line velocities are higher than the Hα line velocity after $\sim$80 days.

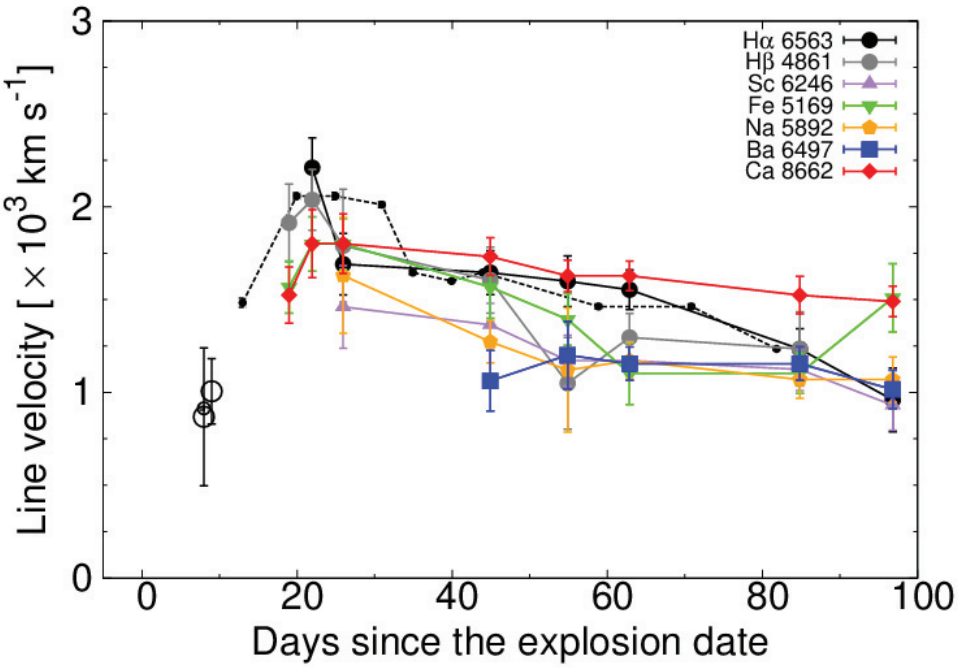

Figure 3.10: Velocity evolutions of the Hα , Sc II , Fe II , Na I D, and Ca II lines in SN 2016bkv. The symbols are indicated in the upper-right of the panel. The open black circles show the line velocity of the weak absorption component accompanied with the narrow Hα emission line seen at 8 and 9 days (see Section 4.1.4). We obtain the errors by taking into account the uncertainties in the wavelength calibration and fitting error. In addition to the measurements for our spectra, we also added Hα line velocities measured by Hosseinzadeh et al. (2018) with black dots and the dashed line.

Figure 3.11 shows the Hα velocity evolution of SN 2016bkv, compared with other LL SNe and the normal SN IIP 1999em (Leonard et al., 2002a). For SN 2016bkv, the spectra are also obtained by Hosseinzadeh et al. (2018). Thus, the Hα velocity measured by the same manner are plotted in this figure (dashed line). It is clear that LL SNe IIP commonly show lower velocities than those of SN IIP 1999em over the entire phases. SN 2016bkv exhibits the lowest velocities among LL SNe IIP until $\sim$60 days. Interestingly, SN 2016bkv shows a slower evolution; the evolution of line velocities after $\sim$20 days is flatter than the other LL SNe IIP. The slow

recession of the photospheric velocity means that the photospheric radius ($R_{\rm ph}$) tends to be large. This may be related to the slight increase in the luminosity at the end of the plateau phase ($L \propto R_{\rm ph}^2 T^4$) seen in SN 2016bkv.

The Hα velocities at the earliest phases are interest. At 4, 5, and 7 days, the spectra exhibit the emission line of Hα , and then, a very weak absorption component is possibly detected at 8 and 9 days for Hα . The velocities of these absorption components are measured as 800–1,000 km s^{-1} (open symbols in Figures 3.10 and 3.11). In addition to the absorption lines, we measure the width of the emission line of Hα . We find that the FWHMs of the emission lines are similar to the blueshift velocities of the absorption components, i.e., 800–1,000 km s^{-1} . These velocities are clearly slower than the velocities of the stronger absorption component which appears after 26 days (1,700 km s^{-1}) in the same SN. Implication from this feature is discussed in Section 4.1.

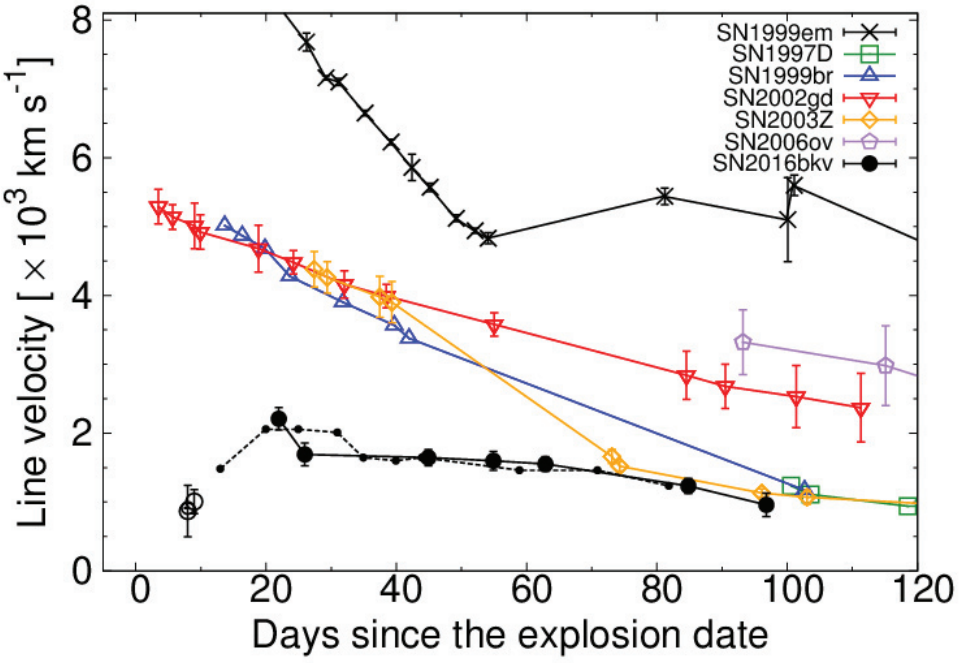

Figure 3.11: Comparison of Hα line velocities among LL IIP SNe 2016bkv, 1997D and 1999br (Pastorello et al., 2004), 2002gd, 2003Z, 2006ov (Spiro et al., 2014), and a normal SN IIP 1999em (Leonard et al., 2002a). The black dots and the dashed line shows the velocities measured in the spectra of SN 2016bkv by Hosseinzadeh et al. (2018).

3.1.11 Line Velocity of Sc II

Figure 3.12 shows the velocity evolution of Sc II (6243 Å). Pastorello et al. (2004) suggest that this line is a tracer of the photospheric velocity for LL SNe IIP. As in the case for Hα line,

SN 2016bkv shows the lowest velocity among the LL SNe IIP and the normal SN IIP 1999em until ∼60 days in this line.

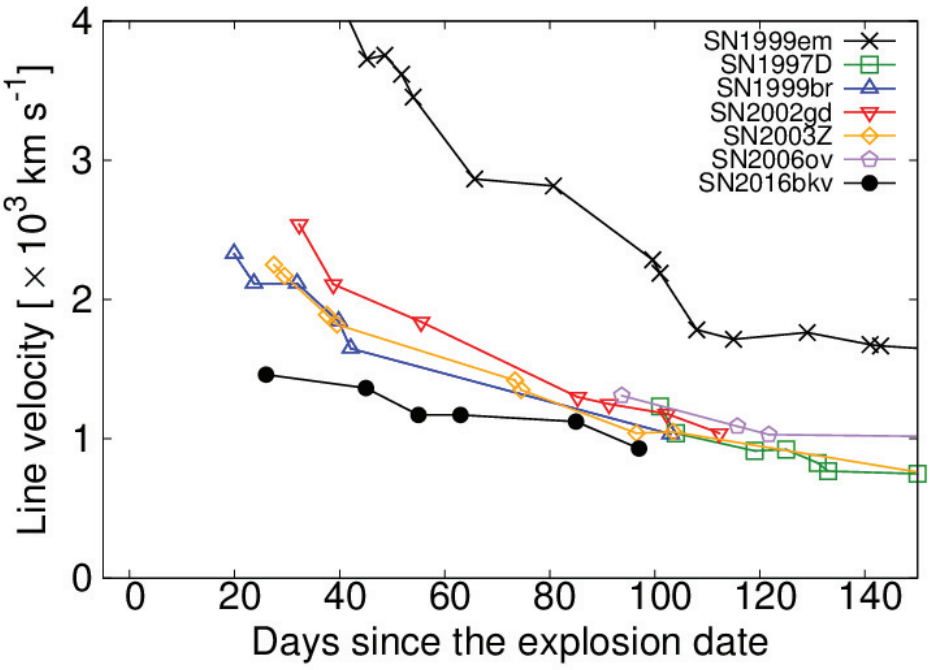

Figure 3.12: The same as Figure 3.11, but for the Sc II λ6243 line velocity.

3.2 SN 2017czd

In this section, we present the characteristics of the second target in this thesis, SN 2017czd.

3.2.1 Discovery and Host Galaxy

SN 2017czd was discovered by Koichi Itagaki on 2017 April 12.7 (UT) (Itagaki, 2017). About 1 day after the discovery, this SN was classified as a young SN II with the featureless and blue continuum by spectroscopic observation (Hosseinzadeh et al., 2017). The host galaxy, UGC 9567, is an irregular galaxy with emission lines. The date of explosion is constrained by the latest non-detection date (Apr 10.3) by Gaia Photometric Alerts. In this thesis, the explosion date is assumed to be 2017 Apr 11.5 (defined as $t = 0$ days, where t is the time since the explosion in the rest frame), which is the middle between the latest non-detection and the discovery. The observational epoch is given with respect to this explosion date.

3.2.2 Extinction in the Host Galaxy

In the light curves shown in Figure 3.13, the Galactic extinction of $E(B-V) = 0.02$ (Schlafly & Finkbeiner, 2011) has been corrected for. Since any clear absorption lines of Na I D at the wavelength corresponding to the host galaxy is not detected (equivalent width $\lesssim$0.062 Å), We assume that the extinction within the host galaxy is negligible.

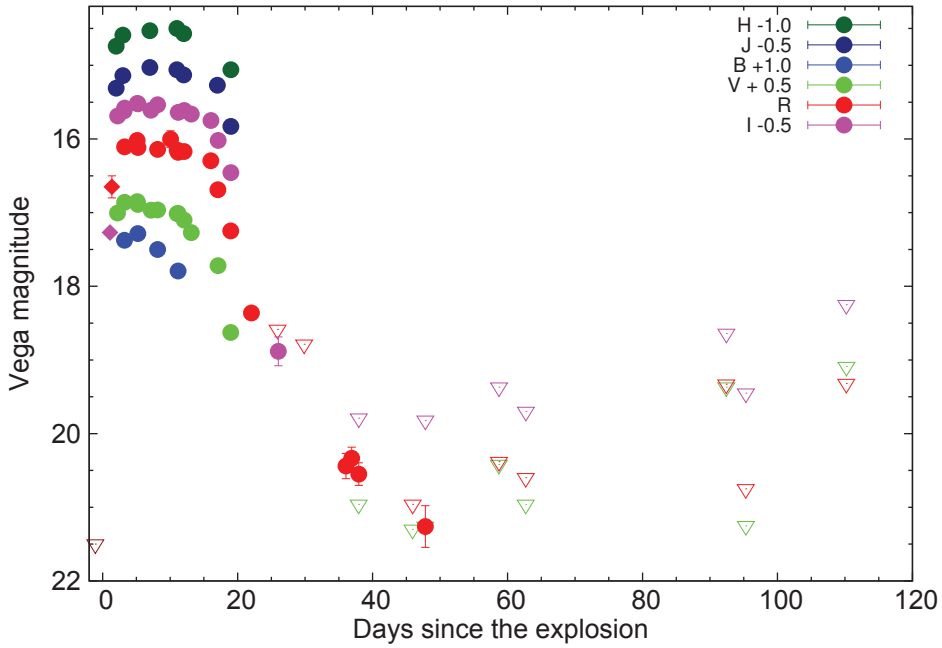

Figure 3.13: Optical and NIR light curves of SN 2017czd. Circles show the HOWPol and HONIR data. The diamond shapes at the early epochs show non-filter magnitude in K. Itagaki's image (red) and Pan-STARRS i-band magnitude (magenta). The Galactic extinction (Schlafly & Finkbeiner, 2011) has been corrected. The upper limits are denoted by the triangles.

3.2.3 Photometry

The data of the observational result in SN 2017czd is shown in Figure 3.13, Table 3.4 and Table 3.5. The obtained $BVRI$-band data are obtained using HOWPol on 31 nights from 2017 April 14.6 (t = 3.1 days) through Aug 30.5 (t = 137.8 days), and HONIR on 14 nights from 2017 April 13.6 (t = 2.1 days) through May 11.5 (t = 29.7 days).

Contamination from the underlying background emission from the host galaxy cannot be ignored in the optical data (see Figure 3.14). For photometry, we first performed image subtraction using the HOWPol and HONIR data taken at 2018 Apr 18 (t = 327 days). Then, we measured the brightness in the subtracted images. Local standard star magnitudes were calibrated using the photometric standard stars (Landolt, 1992) (see Figure 3.14 and Table 3.6).

The resultant magnitudes of SN 2017czd are summarized in Table 3.4. Figure 3.13 shows the light curves of where the Galactic extinction has been corrected for.

We also performed the point-spread function (PSF) photometry of the SN in the discovery image obtained by Itagaki who is an amateur astronomer in Japan. We considered the non-filter magnitude as R-band according to the literature (Zheng et al., 2014). This photometric information is also included in the R band light curves presented in this thesis.

The optical images of the SN 2017czd obtained in the Gemini Multi-Object Spectrograph (GMOS, Hook et al., 2004) attached to the 8.0-m Gemini telescope on 2018 Jul 15 ($t = 456$ days) are also used in this thesis. We confirmed that there was no object brighter than the underlying component of the host galaxy at the position of the SN in the r-band images. We also confirmed that the brightness of the underlying component of the host galaxy is consistent with pre-explosion images obtained by Sloan Digital Sky Survey (SDSS) and Pan-STARRS.

The NIR imaging data were obtained using HONIR on 18 nights from 2017 Apr 13.6 ($t = 2.1$ days) through May 27.6 ($t = 18.8$ days). By using the images taken with dithering method , we accurately subtract the bright foreground sky. We did not subtract the underlying component of the host galaxy for the NIR imaging data since its contamination was less than $\sim 10\%$ ($t = 2.1 - 18.8$ days). After taking the standard manner of the data reduction (see Section 2.3), we carried out the PSF photometry. Photometric calibrations were performed using magnitudes of reference stars given in the 2MASS catalog (Persson et al., 1998). The derived JHK_s-band magnitudes and the light curves are shown in Table 3.5 and Figure 3.13, respectively.

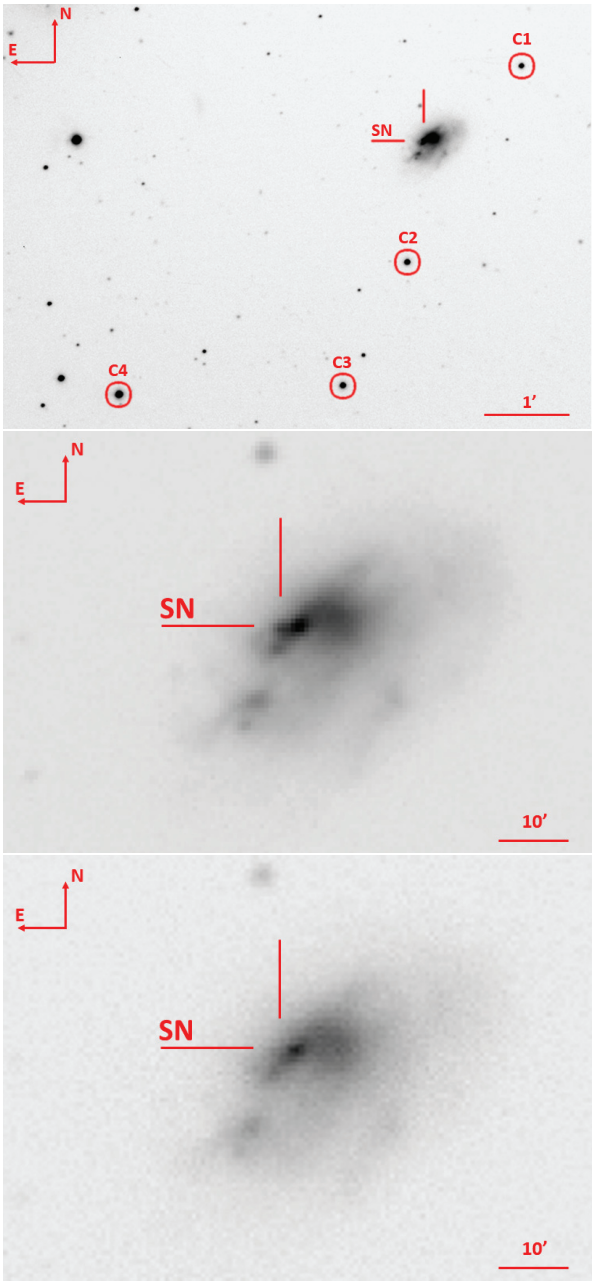

Figure 3.14: (Top) The R-band image of SN 2017czd in UGC 9567 taken at $t = 5.0$ days using HOWPol. The location of the SN is marked by the two lines. Comparison stars are marked by the circles. (Middle) The same with the top panel but the image close to the SN position. (Bottom) The same with the Middle panel but the image at $t = 327$ days.

Table 3.4: Log of the optical photometry of SN 2017czd.

MJD	Epoch (day)	B (mag)	V (mag)	R (mag)	I (mag)	Instrument
57856.6	2.1	—	16.5(0.07)	—	16.19(0.05)	HONIR
57857.6	3.1	16.38(0.03)	16.36(0.02)	16.11(0.02)	16.08(0.02)	HONIR
57859.6	5.0	16.28(0.02)	16.39(0.03)	16.12(0.04)	16.02(0.03)	HOWPol
57861.6	7.0	—	16.47(0.06)	—	16.11(0.05)	HONIR
57862.6	8.0	16.5(0.05)	16.46(0.02)	16.14(0.05)	16.04(0.02)	HOWPol
57864.5	9.9	—	—	16.02(0.11)	—	HOWPol
57865.7	11.1	16.79(0.02)	16.51(0.02)	16.18(0.06)	16.14(0.02)	HOWPol
57866.6	12.0	—	16.6(0.04)	16.19(0.04)	16.11(0.04)	HONIR
57867.6	13.0	—	16.77(0.05)	—	16.16(0.04)	HOWPol
57870.6	15.9	—	—	16.32(0.05)	16.25(0.05)	HOWPol
57871.6	16.9	—	17.22(0.07)	16.71(0.05)	16.52(0.04)	HONIR
57873.5	18.8	—	18.13(0.07)	17.27(0.05)	16.96(0.05)	HONIR
57876.6	21.9	—	—	18.38(0.06)	—	HOWPol
57880.5	25.7	—	—	>18.59	19.38(0.19)	HONIR
57884.5	29.7	—	—	>18.79	—	HONIR
57890.8	36.0	—	—	20.44(0.17)	—	HOWPol
57891.6	36.7	—	—	20.34(0.15)	—	HOWPol
57892.7	37.8	—	—	20.55(0.15)	>20.29	HOWPol
57900.7	45.8	—	>20.8	>20.96	—	HOWPol
57902.6	47.7	—	>20.76	21.26(0.28)	>20.32	HOWPol
57913.6	58.6	—	>19.92	>20.38	>19.87	HOWPol
57917.6	62.5	—	>20.46	>20.6	>20.2	HOWPol
57947.6	92.2	—	>18.87	>19.33	>19.14	HOWPol
57950.6	95.2	—	>20.75	>20.75	>19.95	HOWPol

Table 3.5: Log of the NIR photometry of SN 2017czd.

MJD	Epoch (day)	J (mag)	H (mag)
57856.6	2.1	15.81(0.03)	15.75(0.03)
57857.6	3.1	15.64(0.03)	15.59(0.03)
57861.6	7.0	15.54(0.03)	15.53(0.03)
57865.7	11.1	15.56(0.02)	15.51(0.03)
57866.6	12.0	15.64(0.03)	15.58(0.04)
57871.6	16.9	15.77(0.03)	—
57873.5	18.8	16.33(0.09)	16.06(0.05)

Table 3.6: Optical magnitudes of the comparison stars

ID	B (mag)	V (mag)	R (mag)	I (mag)
C1	17.75(0.03)	17.15(0.02)	16.67(0.01)	16.2(0.06)
C2	17.06(0.03)	16.56(0.02)	16.11(0.02)	15.71(0.03)
C3	16.62(0.04)	16.28(0.06)	15.94(0.02)	15.57(0.03)
C4	15.76(0.04)	15.31(0.02)	14.88(0.02)	14.46(0.03)

3.2.4 Light curves

The light curves of SN 2017czd can be divided into four stages based on the slopes of the R-band light curve: (i) the rising phase (up to t ∼3 days), (ii) the plateau phase (between t ∼3 and 16 days), (iii) the declining phase (between t ∼16 and 30 days), and (iv) the tail phase (after t ∼30 days). Below we discuss the light-curve properties in each stage.

A rapid rise is found at the earliest phase. The rising rate is ∼0.3 mag day^{-1}in the R-band between t = 1.4 and 3.1 days. Using the i-band magnitude of 17.8 mag obtained by the Pan-STARRS at t = 1.1 days[2], we obtain the rising rate of 1.6 mag day^{-1}in the I-band between t = 1.1 and 2.1 days. Combined with the fact that the pre-discovery upper-limit magnitude of 21.5 mag at t = -1.2 days, it is evident that this SN experiences a rapid rise just after the explosion.

Between $t \sim 3$ and 16 days, the light curves show a short plateau except in the B-band. The flat shape of the light curves are evident in R and I bands. We define t_p as the duration in which the magnitude is constant within ± 0.2 mag. We find t_p ∼13 days in R and I bands. In the V-band, the plateau is also seen, but the duration is shorter than those in the R and I-bands, i.e., the V-band light curve turns to decline around t = 13 days. In the B-band, the light curve reaches the peak at t ∼5 days and then starts to decline. These characteristics of the plateau is similar to the normal SNe IIP except for the plateau length (see also Figure 3.18). Given the sparse NIR data, the plateau shapes in the J and H -band light curves are not as clear as in the R and I-bands, but they also show relatively flat light curves between t ∼3 and 16 days.

After the plateau, optical light curves show rapid decline. In particular, the R and I-band light curves suddenly drop after their plateau phases. The light curves in shorter wavelengths exhibit more rapid evolution; the decline rates between t = 15.9 and 21.9 days are estimated to be 0.5, 0.3, and 0.2 mag day^{-1}in the V, R, and I bands, respectively. We see a slowdown in the decline rate of the $R-$band light curve after $t \sim 35$ days (0.1 mag day^{-1}) although the photometric errors at t = 47.7 days are rather large.

Comparison with Other Transients

Compared with normal SNe, the light curves of SN 2017czd show more rapid evolution, but its absolute magnitudes are within the range of normal SNe. Figure 3.15 compares the absolute R-band magnitude of SN 2017czd with those of normal SNe; SNe Ib 2008D (Modjaz et al., 2009), IIL 1986L (Anderson et al., 2014), IIb 1993J (Richmond et al., 1996a), IIP 1999em (Leonard et al., 2002a), IIb 2008ax (Pastorello et al., 2008), and IIn 2009ip (Smartt, 2015). In order

[2]https://wis-tns.weizmann.ac.il/object/2017czd

to compare their rise times quantitatively, we define the time taking from the half maximum luminosity to the maximum one as $t_{1/2,\mathrm{rise}}$. For SN 2017czd, it is estimated to be 2.6 days, which is much shorter than those of SNe 1993J (7.64 days) and 2008ax (9.05 days).

The R-band magnitude around the peak is -16.5 mag for SN 2017czd, which is comparable to those of SNe 1999em and 2008D. After the sudden light-curve drop, the absolute magnitude of SN 2017czd becomes much fainter than those of SNe 1986L, 1993J, 1999em, 2008D, 2008ax, and 2009ip The brightness after the plateau becomes comparable to faint SN Iax 2008ha (Foley et al., 2009; Valenti et al., 2009).

To closely compare the rapid decline rate after the plateau, we show the magnitude relative to the peak in the bottom panel of Figure 3.15. The decline rate of SN 2017czd (0.3 mag day^{-1}in R-band) is the highest among other SNe compared in Figure 3.15. For example, the magnitude decline is 4.5 mag within $\sim$ 20 days after the peak for SN 2017czd, while it is 1.5 mag for SN 2008ha.

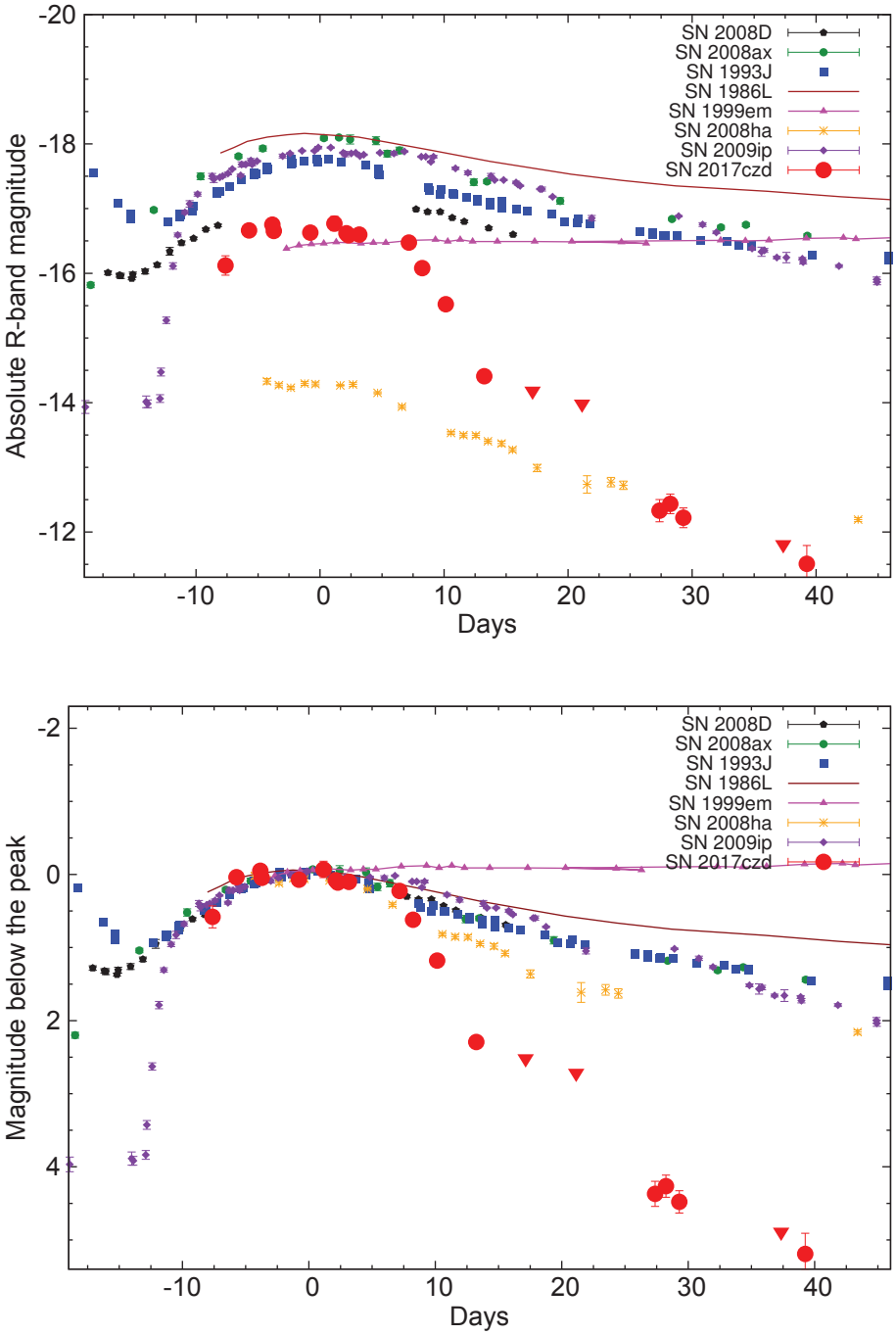

Figure 3.15: (Top) The R-band absolute magnitudes of SN 2017czd compared with those of well-observed SNe. The extinction of each SNe has been corrected for. The inverse triangle of SN 2017czd is shown in an upper limit. Light curves are shifted along the time axis to match their maximum dates. (Bottom) The same as the top panel but the magnitudes relative to the peaks (i.e., shifted along the vertical axis to match the peak magnitudes). Both figures are compared in the rest frames.

Next, we compare the SNe II which have especially short plateau. Figure 3.16 shows the V-band light curve of SN 2017czd and comparison objects which have especially short plateau exhibited by Anderson et al. (2014). The V-band light curve of SN 2017czd shows similar evolution to that of SN 2006Y at $\lesssim$15 days. From this figure, SN 2017czd is the object which have the shortest plateau among the well observed SNe II.

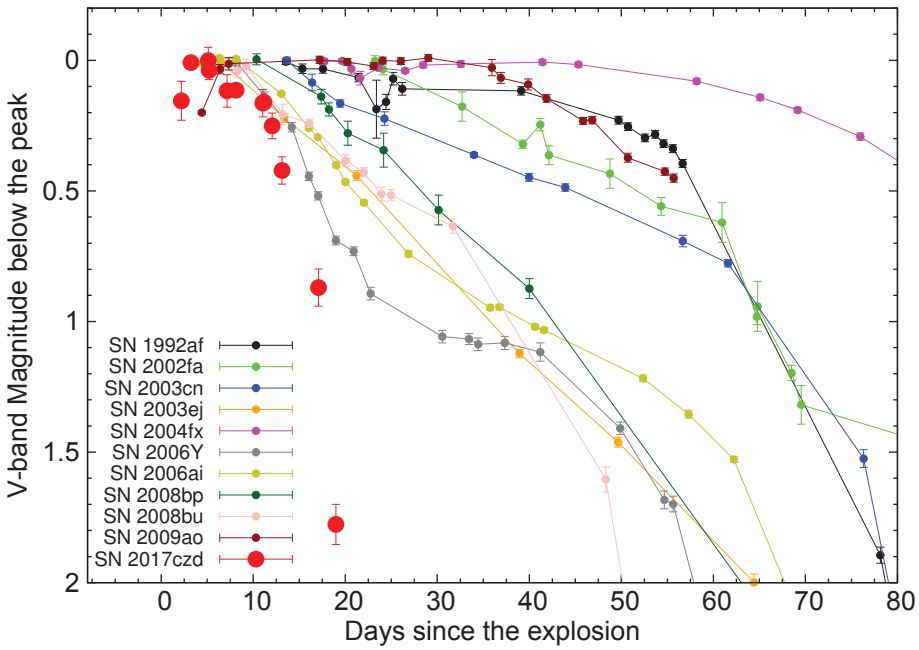

Figure 3.16: The V-band light curves of SN 2017czd and several SNe which have short plateau (Anderson et al., 2014).

The fast decline of SN 2017czd is in fact similar to those of "rapidly evolving transients". Figure 3.17 shows the R-band light curve of SN 2017czd compared with those of rapid transients given by Drout et al. (2014), and the fast declining SN Ic 1994I (Richmond et al., 1996b) and SN 2002bj (Poznanski et al., 2010). A large diversity of $\sim$3 mag is seen in the peak absolute magnitudes in the rapid transients of Drout et al. (2014), and SN 2017czd is located at the faint end. Among rapid transients presented by Drout et al. (2014), the observations after t $\sim$20 days are available only for PS1-10ah, and SN 2017czd shows a faster decline than PS1-10ah.

The bottom panel of Figure 3.17 compares the light curves relative to the peak. Compared with other rapid transients in the figure, only SN 2017czd exhibits a plateau in the light curve. Because the data are sparse in the rapidly evolving transients, we define the decline time ($t_{1/2,\mathrm{decline}}$) as the time taking from the light-curve maximum to the half maximum as the alternatives. The timescale of SN 2017czd ($t_{1/2,\mathrm{decline}}$ = 14.5 days in the R-band) is similar to those of SN 2002bj (8.3 days in the R-band, Poznanski et al. 2010) and the Pan-STARRS rapid transients ($t_{1/2,\mathrm{decline}}$ =3–17 days in the r-band, Drout et al. 2014).

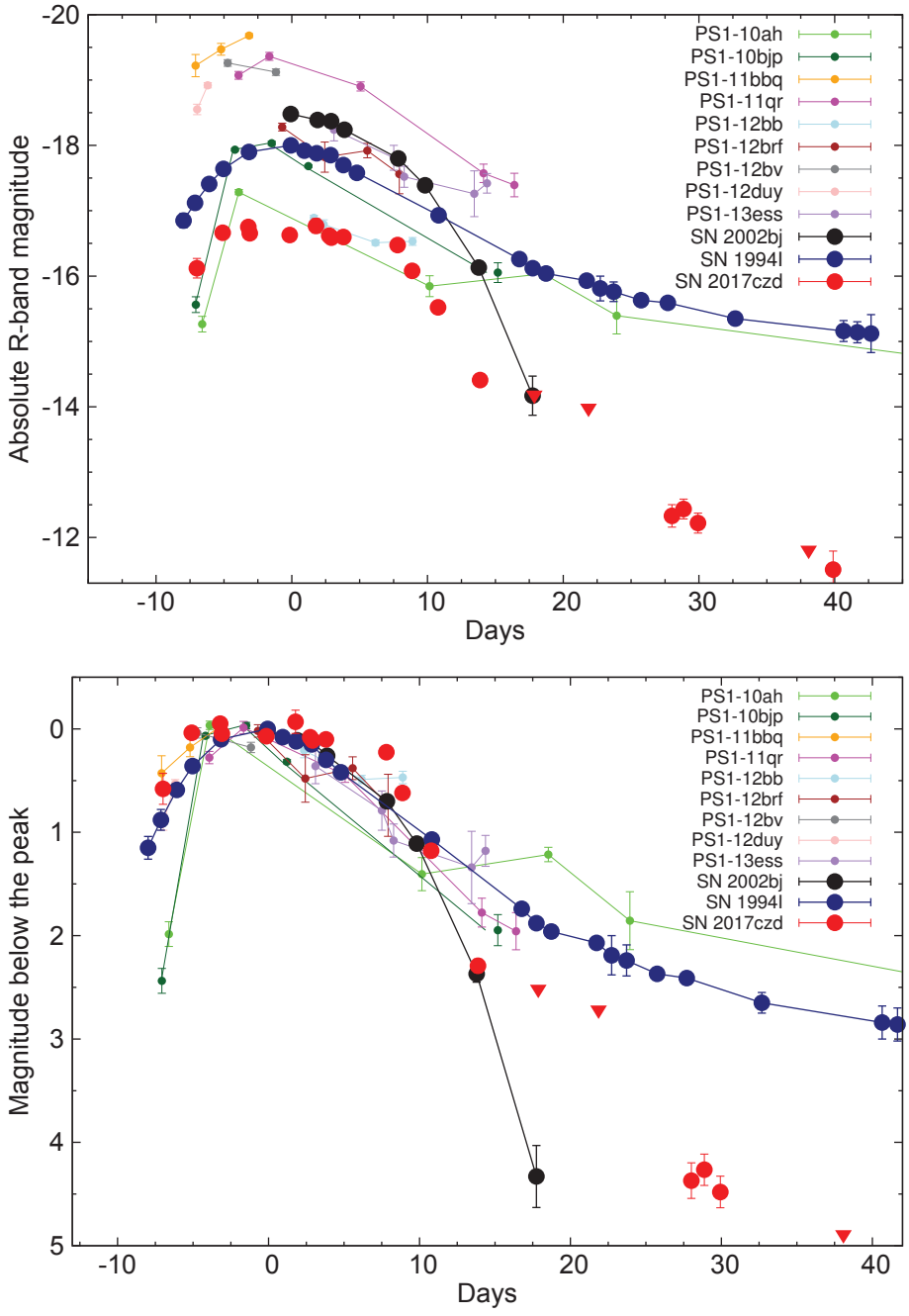

Figure 3.17: (Top) The R-band absolute magnitudes of SN 2017czd compared with those of rapidly evolving transients given by Drout et al. (2014) in the r-band. The extinction of each SNe has been corrected for. The days of these SNe are shifted to match their maximum dates along the horizontal axis. (Bottom) The same as the top panel but the data are shifted along the vertical axis to match the peak magnitude, i.e., showing the light curves relative to the peaks. In both figures, the epochs are corrected to match the rest frame ones.

Motivated by the presence of the short plateau in the light curve, we also compare the light curve of SN 2017czd with SNe II. Figure 3.18 shows the light curve of SN 2017czd compared with SNe 1993J, 1999em, and SN impostor 1997bs (Van Dyk et al., 2000). As in other Type IIP SNe, SN 1999em shows a plateau lasting ∼100 days in the R-band. We stretch the light curve of SN IIP 1999em to match that of SN 2017czd by assuming a stretch factor of 0.17 in time (blue in Figure 3.18). The stretched light curve is in fact quite similar to that of SN 2017czd until t ∼20 days. The sharp drop after the plateau is also similar, although the light curve of SN 2017czd keeps declining rapidly.

It is interesting to note that SN (or SN impostor) 1997bs also shows a short plateau in the R-band light curve (Figure 3.18), whose timescale is comparable to that in SN 2017czd. However, several characteristics are different from those of SN 2017czd: the plateau luminosity in SN 1997bs is lower than that of SN 2017czd, and the light curve after the short plateau becomes flat again. Furthermore, spectra of SN 1997bs show narrow emission lines, which are not seen in SN 2017czd (see Section 3.2.6).

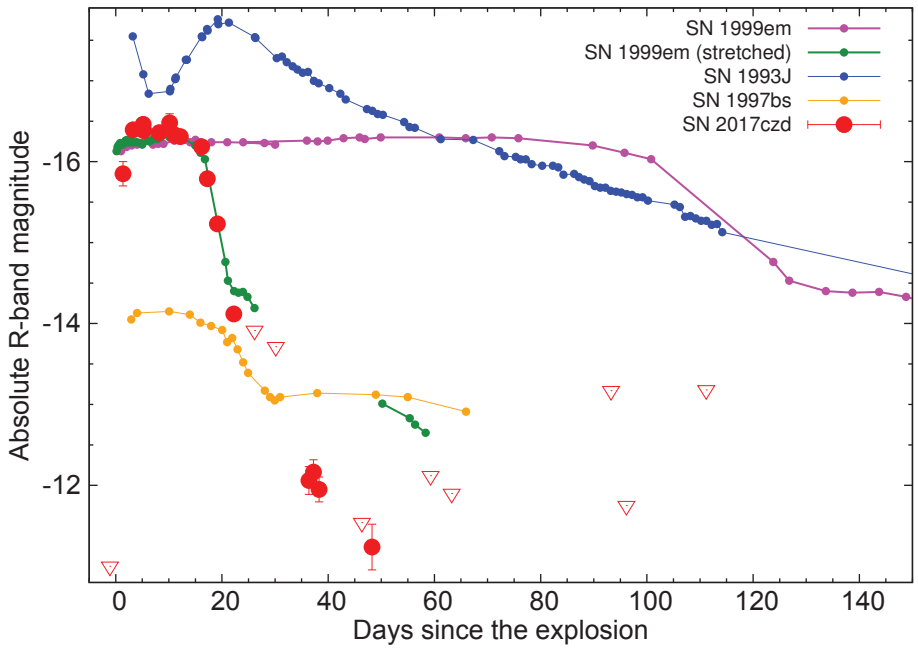

Figure 3.18: The R-band absolute magnitudes of SN 2017czd compared with those of SNe IIb 1993J, IIn 1997bs, and IIP 1999em. The inverse triangle of SN 2017czd is shown in an upper limit. The green curve shows the light curve of SN 1999em whose timescale is stretched by a factor of 0.17.

3.2.5 Color Evolution

Figure 3.19 compares the $V-R$ color evolution of SN 2017czd and some SNe II; SNe IIb 1993J (Richmond et al., 1996a), IIP 1999em (Leonard et al., 2002a), and IIb 2008ax (Pastorello et al., 2008). Until t ∼10 days, the $V-R$ color of SN 2017czd is similar to or slightly redder than those of SNe 1993J and 1999em. However, after t ∼15 days, the color in SN 2017czd rapidly becomes redder. Such a rapid change is not seen in other SNe IIb and IIP, confirming that SN 2017czd is a rapidly evolving object in the color, too.

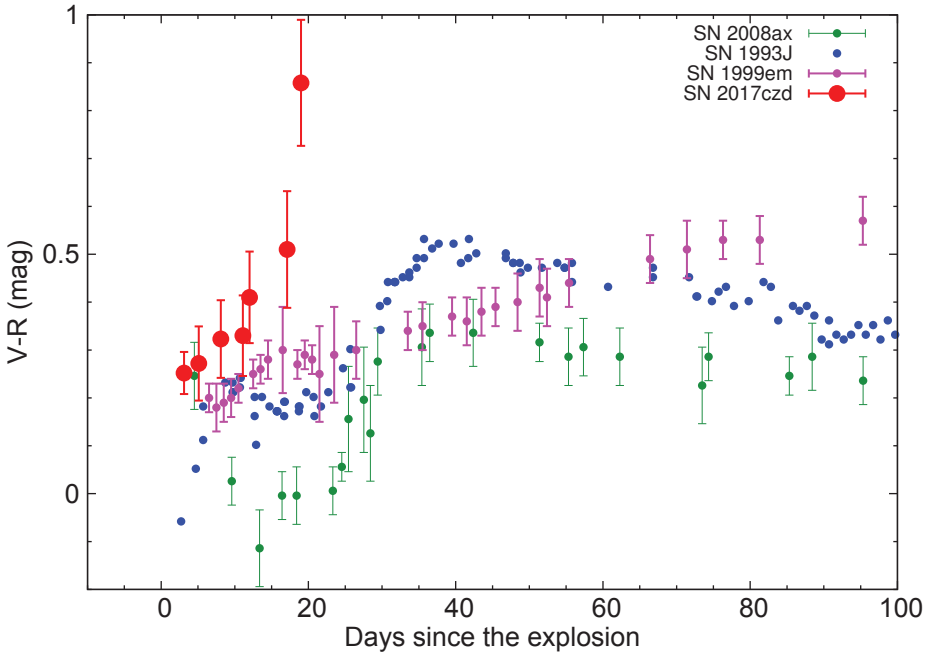

Figure 3.19: The $V-R$ color evolution of SN 2017czd compared with those of SNe IIb 1993J, 2008ax, and SN IIP 1999m. The extinction of each SNe has been corrected for.

3.2.6 Optical Spectra

Optical spectroscopic data are obtained using HOWPol on 9 nights from 2017 Apr 13.6 ($t = 2.1$ days) through 30.7 ($t = 19.0$ days). A grism giving a spectral resolution of $R \sim 400$ and a spectral coverage of 4500–9000 Å are used in this instrument. To calibrate the responce function with the wavelength, spectroscopic standard stars are observed in the same nights. For the wavelength calibration, we used sky emission lines taken in object frames. The strong atmospheric absorption bands around 6900 and 7600 Å have been removed using smooth spectra of hot standard stars. Additionally, the continuum of the spectra is calibrated to match the SED from the photometry at the same epoch if necessary. The log of our spectroscopic observations is given in Table 3.7, and the obtained spectra are shown in Figure 3.20.

Figure 3.20 shows the time evolution of the optical spectra from the initial rising phase (t = 2.1 days) through the declining phase (t = 19.0 days). Note that narrow emission lines of Hα , Hβ , [O III] $\lambda\lambda$ 4959, 5007, [N II] λ 6583, and [S II] $\lambda\lambda$ 6716, 6731 come from the H II region in the host galaxy. Initially, the spectra are dominated by the blue continuum as in SNe IIP in their early phases (e.g., Huang et al., 2018). The broad absorption component is seen around 6000 Å from t = 3.1 days which could be a high-velocity component of Hα . This possible broad Hα feature led us to classify SN 2017czd as an SN II as discussed below. In addition to Hα , the broad feature of Ca II IR triplet is seen in the spectrum at t = 16.0 and 19.0 days.

Table 3.7: Log of spectroscopic observations of SN 2017czd.

MJD	Epoch (day)	Exposure (sec)
57856.6	2.1	2400
57857.6	3.1	2700
57859.6	5.0	2700
57861.8	7.2	2700
57865.6	11.0	2700
57866.6	12.0	2700
57867.7	13.1	3600
57870.7	16.0	2700
57873.7	19.0	2700

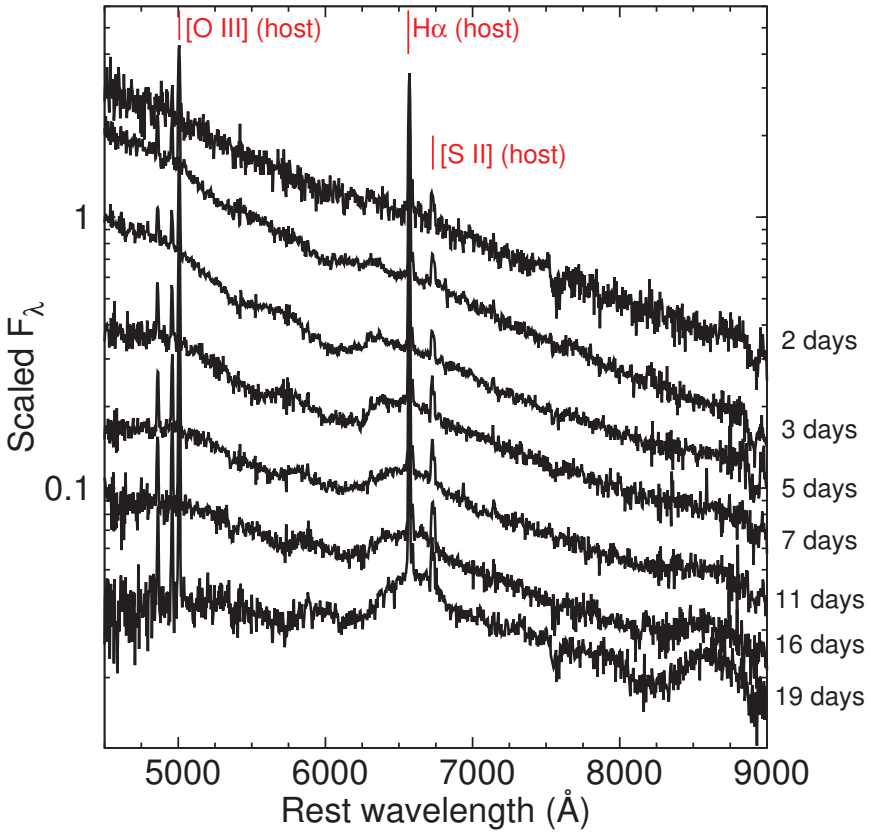

Figure 3.20: Spectral evolution of SN 2017czd. The epoch for each spectrum, shown in the right outside of the panel, is given in days since the explosion.

3.2.7 Early Phase Spectra

The spectra of SN 2017czd are similar to those of SNe IIP in early phases. Figure 3.21 shows the spectral comparison with various types of SNe; SN 2017czd at $t = 7$ days, SN IIP 2006bp at $t = 6$ days (Quimby et al., 2007), SN IIb 1993J at $t = 5$ days (Barbon et al., 1995), SN IIn 1998S at $t = 2$ days (Fassia et al., 2001), luminous SN Ia 1991T at $t = 10$ days (Mazzali et al., 1995), and broad-lined SN Ic 2006aj at $t = 14$ days (Pian et al., 2006). The blue continuum and the broad Hα line in the spectrum of SN 2017czd match those of SN 2006bp at $t = 6$ days. This fact supports our classification of SN 2017czd as a SN II. SNe 1993J and 2006aj show more prominent absorption lines than SN 2017czd. SNe 1998S and 1991T also show the blue continuum. However, SN 1998S shows characteristic narrow emission lines and SN 1991T shows a strong absorption feature of Fe III around 5000 Å. Thus, they are clearly different from SN 2017czd.

In Figure 3.22, we compare SN 2017czd with SNe II, SNe IIP 1999em, 2012aw and SN IIb

1993J, at around $t = 5$ days. The Hα absorption line of SN 2017czd is shallow and blueshifted compared with those of SNe IIP. Figure 3.23 shows the comparison with the same SNe but at later epoch. The spectrum of SN 2017czd shows weak absorption lines of Hα , Ca II IR triplet, and He I λ 5876 at $t = 20$ days. The spectral features of SN 2017czd are broadly similar to SNe IIP at early phase ($\sim$ 5 days) and similar to SN IIb 1993J at decline phase.

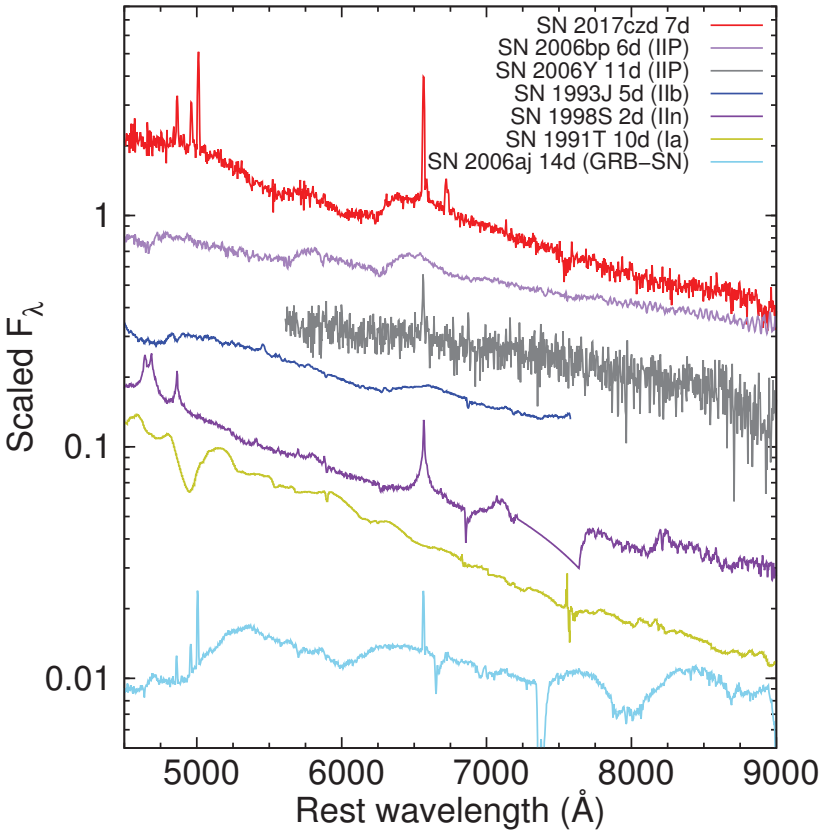

Figure 3.21: Spectrum of SN 2017czd at 7 days compared with well-observed SN IIP 2006bp, SN IIb 1993J, SN IIn 1998S, SN Ia 1991T, and broad-lined SN Ic 2006aj at similar epochs. The fluxes were shown in the logarithmic scale and arbitrarily scaled to avoid overlaps.

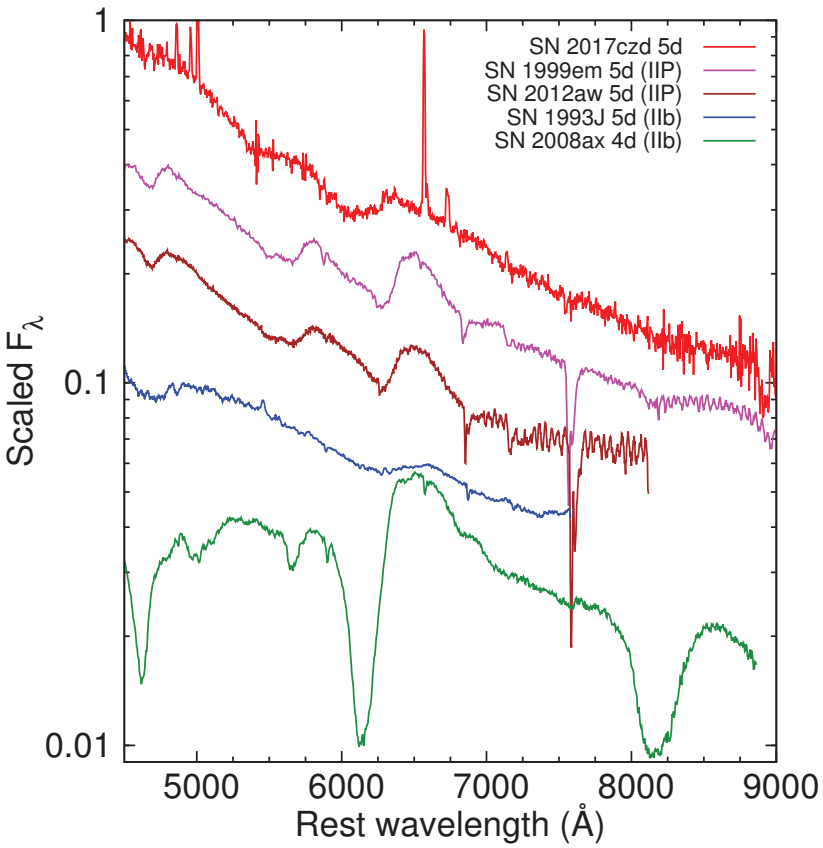

Figure 3.22: Spectrum of SN 2017czd at $t \sim 5$ days compared with those of hydrogen-rich SNe at similar epoch.

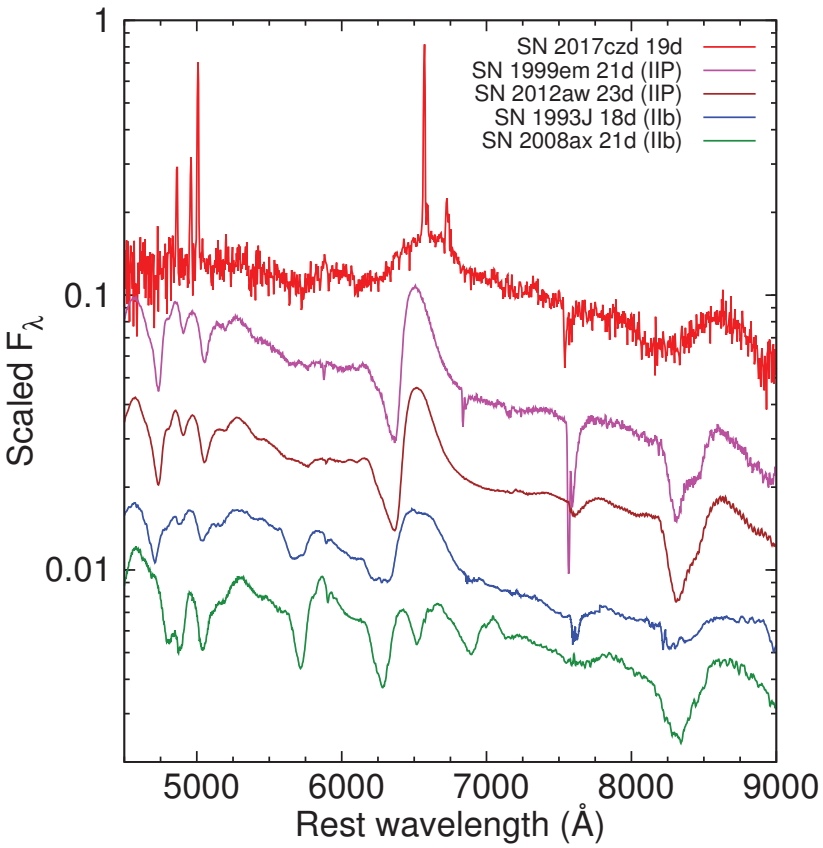

Figure 3.23: The same as Figure 3.22 but at around $t \sim 20$ days.

3.2.8 Line Velocity

Figure 3.24 shows the evolution of the Hα line velocity in SN 2017czd. We fit the Gaussian function to the Hα absorption component. We consider the difference between the rest wavelength and the wavelength at the minimum of the fitting function as the line velocity. The Hα line velocity of SN 2017czd is about $\sim$26,000 km s^{-1} at $t \sim$3 days and declines to $\sim$20,000 km s^{-1} at $t \sim$15 days. These velocities are significantly higher than those of other SNe II at similar epochs, which are around 10,000–20,000 km s^{-1} .

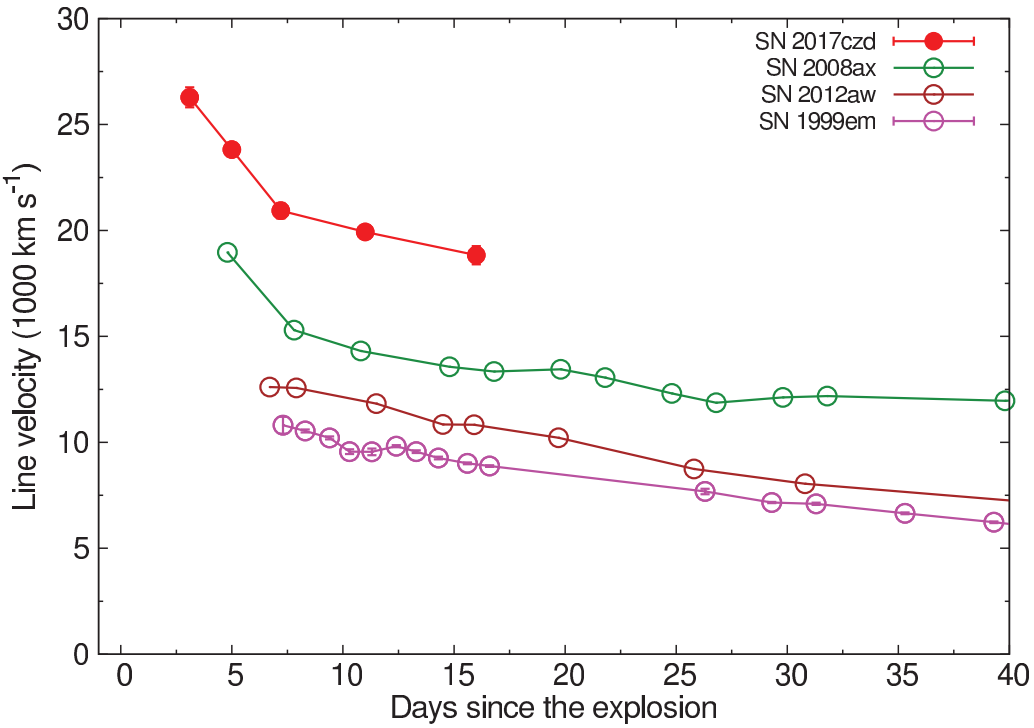

Figure 3.24: Hα line velocity evolution of SN 2017czd compared with those of SNe IIP 1999em, 2012aw, and IIb 2008ax. The errors are calculated from the wavelength calibration and the Gaussian fitting error. The wavelength resolution corresponds to the velocity resolution of 750 km s^{-1} .

Chapter 4

Discussion

4.1 SN 2016bkv

4.1.1 Bolometric Luminosity

We derived quasi-bolometric luminosities by integrating the $BVRI$-band fluxes as follows. First, the extinction-corrected $BVRI$-band magnitudes were converted into fluxes using filter parameters (Bessell, 1990) and the zero-magnitude fluxes (Fukugita et al., 1995). Then, we fitted the spectral energy distributions (SEDs) with the blackbody function. Finally the flux is integrated by using the best-fit blackbody parameters. In the blackbody fit, we have included the JHK_s-band if available, in order to constrain the temperature as accurately as possible. Then the fluxes are integrated in the $BVRI$-band wavelength region. The quasi-bolometric luminosities of other LL SNe IIP were also calculated in the same manner. This allows fair comparisons to the other samples, as the NIR data are not always available.

Figure 4.1 shows the SED with $BVRIJHK_s$-band fluxes and the best-fit blackbody function at 7.4 days after the explosion (at the peak of the early bump). The blackbody temperature is obtained to be $9,600 \pm 600$ K. The temperature of LL SNe IIP 2002gd at 5.7 and 9.1 days are 12,700 K and 9,700 K, respectively (Spiro et al., 2014). Note that since there is no data at ultraviolet wavelengths and the temperature estimation in particular at $T > 10,000$ K is somewhat uncertain. To illustrate this uncertainty, the blackbody functions with the temperature of $\sim$12,000 and $\sim$8,000 K are also shown in Figure 4.1. This uncertainty affects the bolometric luminosities up to by a factor of about two.

Figure 4.2 shows the quasi-bolometric light curve of SN 2016bkv, compared with those of other LL SNe IIP and the normal SN IIP 1999em. As in the multi-color light curves, the bolometric luminosity of SN 2016bkv clearly shows a bump ($\gtrsim$1 mag) in the early phase. As expected, the luminosities of SN 2016bkv are always $\sim 7 - 10$ times fainter than those of the normal SN IIP 1999em. In comparisons with LL SNe IIP, the luminosities of SN 2016bkv are comparable to those of SN 2002gd before peak. After the bump ($\sim$30 days), the luminosities of SN 2016bkv become 2–3 times fainter than those of SN 2002gd, and become comparable to those of SN 2003Z.

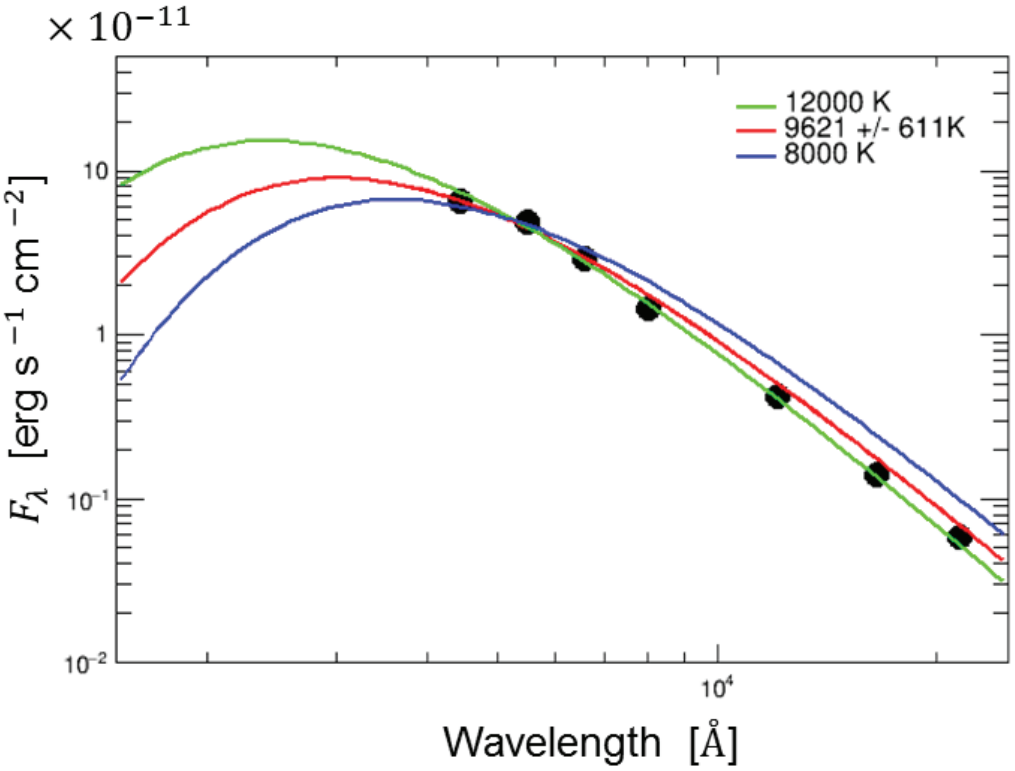

Figure 4.1: SED of SN 2016bkv at 7.4 days after the explosion as compared to blackbody with different temperatures. The best fit model (9621 K, in red), models of higher temperature (8000 K, in blue) and lower one (12000K, in green).

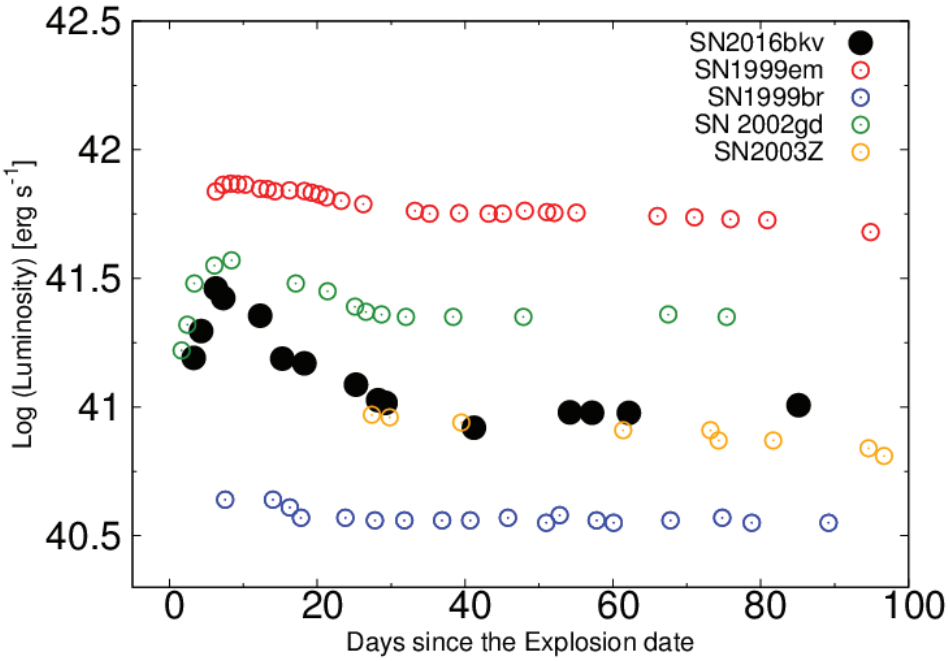

Figure 4.2: Quasi-bolometric light curve of SN 2016bkv compared with that of LL SNe IIP 1999br (Pastorello et al., 2004), 2002gd, 2003Z (Spiro et al., 2014) and a normal SN IIP 1999em (Leonard et al., 2002a). For all the SNe, the quasi-bolometric luminosities are derived by blackbody fitting in the *BVRI*-band wavelength range.

4.1.2 ^{56}Ni Mass

We give a constraint on the ^{56}Ni mass of SN 2016bkv using the luminosity at the tail phase. As discussed in Section 2, The luminosities are defined as the upper limit in the late phase due to the bright background emission from the host galaxy. By using the quasi-bolometric luminosity at 201 day and assuming a relation between the tail luminosity and the ^{56}Ni mass suggested by Hamuy (2003), We obtain the upper limit of $M(^{56}\mathrm{Ni}) \lesssim 0.01 M_{\odot}$. This upper limit of the optical luminosity at ∼200 days is close to the observed luminosity given by Hosseinzadeh et al. (2018). Therefore, the ejected mass of ^{56}Ni is, in fact, likely to be $M(^{56}\mathrm{Ni}) \sim 0.01 M_{\odot}$. This is between the typical ^{56}Ni masses of other LL SNe IIP and those of normal SNe IIP (Spiro et al., 2014).

4.1.3 Explosion Parameters

The observed properties of SNe IIP reflect the photosheric radius and mass of the progenitor and the energy of the explosion. If the density structure and temperature are described in a

self-similar manner for different SNe, the timescale of the plateau ($t_{\rm EoP,sn}$)[1] and the plateau luminosity (L_{sn}) are scaled as follows (Kasen & Woosley, 2009):

$$t_{\rm EoP,sn} \propto E^{-1/6} M_{\rm ej}^{1/2} R_0^{1/6} \kappa^{1/6} T_I^{-2/3}, \text{and}$$
$$L_{\rm SN} \propto E^{5/6} M_{\rm ej}^{-1/2} R_0^{2/3} \kappa^{-1/3} T_I^{4/3}, \tag{4.1}$$

where E is the kinetic energy of the ejecta, $M_{\rm ej}$ is the ejecta mass, R_0 is the radius of progenitor star, κ is the opacity, and T_I is the ionization temperature. These relations are derived by equation of adiabatic expansion, timescale of ejecta and blackbody radiation as follows:

$$E(t) = E(\frac{R(t)}{R_0})^{-1},$$
$$t = \frac{\tau R}{c}, \text{and}$$
$$L = 4\pi\rho R^2 T^4, \tag{4.2}$$

where τ is optically thickness of ejecta. The mean free path of ejecta $\lambda_{\rm ej} = (\kappa\rho)^{-1}$ and optically thickness of ejecta $\tau = \frac{R_{\rm ej}}{\lambda_{\rm ej}}$ are substituted for the equations (4.2). If the ejecta is sphere of uniform density ($\rho \sim \frac{M_{\rm ej}}{R_{\rm ej}^3}$), we derive the relations 4.1. Replacing the kinetic energy by the ejecta velocity ($v_{\rm ej}$), using $E \propto M_{\rm ej} v_{\rm ej}^2$, the relations (4.1) lead to the following expressions:

$$t_{\rm EoP,sn} \propto v_{\rm ej}^{-1/3} M_{\rm ej}^{1/3} R_0^{1/6} \kappa^{1/6} T_I^{-2/3}, \text{and}$$
$$L_{\rm SN} \propto v_{\rm ej}^{5/3} M_{\rm ej}^{1/3} R_0^{2/3} \kappa^{-1/3} T_I^{4/3}. \tag{4.3}$$

Since it is a sound approximation that κ and T_I are the same for different SNe, two quantities, $M_{\rm ej}$ and R_0, are constrained from $t_{\rm EoP,sn}$, $L_{\rm SN}$, and $v_{\rm ej}$.

Here we estimate the properties of SN 2016bkv, using equations above. We first use SN 2003Z for reference, whose properties have been extensively studied with numerical light-curve models (Pumo et al., 2017, $M_{\rm 03Z} = 11.3\ M_\odot, R_{\rm 03Z} = 260\ R_\odot$). As the photospheric velocity, we use the line velocity of the Sc II line (Leonard et al., 2002a). The ratio of velocity of SN 2016bkv to that of LL SN IIP 2003Z ($v_{\rm 16bkv}/v_{\rm 03Z}$) is ∼0.8 around 60 days. Using this velocity ratio, the ratio of $t_{\rm EoP,sn}$ between SN 2016bkv ($t_{\rm 16bkv}$) and SN 2003Z ($t_{\rm 03Z}$) is expressed as follows: $t_{\rm 16bkv}/t_{\rm 03Z} \sim 1.1(M_{\rm 16bkv}/M_{\rm 03Z})^{1/3}(R_{\rm 16bkv}/R_{\rm 03Z})^{1/6}$. We can similarly derive the ratio of the luminosity as $(L_{\rm 16bkv}/L_{\rm 03Z}) \sim 0.65(M_{\rm 16bkv}/M_{\rm 03Z})^{1/3}(R_{\rm 16bkv}/R_{\rm 03Z})^{2/3}$. From this data, $t_{\rm 16bkv}/t_{\rm 03Z}$ is given as ~ 1.4 (see Figure 3.3) and $L_{\rm 16bkv}/L_{\rm 03Z}$ is ~ 1.0 (see Figure 4.2). Here we use $L_{\rm 03Z} = 1 \times 10^{41}$ erg s^{-1} and $t_{\rm 03Z} = 110$ days, respectively. Therefore, we derive $M_{\rm 16bkv}/M_{\rm 03Z} \sim 1.7$ and $R_{\rm 16bkv}/R_{\rm 03Z} \sim 1.5$, suggesting that the ejecta mass is larger in SN 2016bkv.

We also perform similar analysis using SNe 1999br and 2008bk (Pastorello et al., 2004; Lisakov et al., 2017). We obtain similar tendencies, i.e., a larger ejecta mass than these LL SNe IIP,

[1]In this context, We consider that the bump component is additional to the underlying plateau one. Thus, we define $t_{\rm EoP,sn}$ as the epoch of the end of the plateau.

i.e., 1.2 and 2.4 times larger than these objects, respectively. By adopting the explosion parameters presented by Zampieri et al. (2003); Lisakov et al. (2017); Pumo et al. (2017), we derive the ejecta mass and progenitor radius of SN 2016bkv to be 16.1–19.4 $M_\odot$ and 180–1080 $R_\odot$, respectively (Spiro et al., 2014). It should be noted, however, that since the methods to estimate the explosion parameters are different in different papers, the resultant values include large systematic uncertainties.

From these results, we suggest that the progenitor of SN 2016bkv is more massive than the progenitors of other LL SNe IIP. It should be noted that Hosseinzadeh et al. (2018) suggest a relatively low mass ($\sim$9 $M_\odot$) progenitor from the nebular spectra, in particular from the weakness of the [O I] line. However, such a low-mass progenitor is unlikely to result in a late $t_{\rm EoP,sn}$ for $\gtrsim$140 days as derived for SN 2016bkv (see Sukhbold et al., 2016). On the other hand, the estimation using the properties observed of the plateau phase has a different possible systematic error, based on the assumption that the same scaling relations of normal SNe IIP (Eqs. 4.1 and 4.3) are applicable to LL SNe IIP. Therefore, the derived properties are subject to uncertainties. We need more detailed, consistent modeling of both light curves and spectra from the early to nebular phases.

4.1.4 CSM Properties

The luminosity arising from the interaction between the SN ejecta and CSM can be estimated as

$$L = 4\pi r_s^2 \cdot \frac{1}{2}\rho v_{\rm ej}^3 \epsilon, \tag{4.4}$$

where r_s is the radius of the shock and $\epsilon \sim 0.1$ is a conversion factor from the kinetic energy to radiation (Moriya & Maeda, 2014). At the peak of the bump, 7.4 days after the explosion, the luminosity of the bump component is $L = 4\times10^{41}$ erg s^{-1} . Here we extract the luminosity of the bump component from the total luminosity at 7–9 days by subtracting the plateau luminosity at 40–60 days (assuming that the SN luminosity is constant). The plateau component accounts for about one third of the total flux (see Figure 4.2). Assuming that the ejecta velocity is $v_{\rm ej}$ $\sim$2,000 km s^{-1} , which is observed in Hα absorption at 22 days (Figure 3.10), the radius reaches $r_s \sim 1,800$ $R_\odot$ at the peak of the bump. Then we obtain the mass loss rate of $\dot{M}_0/u_{v,5} = 1.7\times10^{-3}$ $M_\odot$ yr^{-1} where $\dot{M}_0$ is the mass loss rate and $u_{v,5}$ is the wind velocity normalized to 10^5cm s^{-1} . The CSM mass within r_s is $M_{\rm CSM} \sim 6.8\times10^{-2}$ $M_\odot$.

If we assume a typical velocity of the red supergiant (RSG) wind, $u_{v,5} = 10$ (i.e., 10 km s^{-1}), the mass loss rate is $\dot{M} \sim 1.7\times10^{-2}$ $M_\odot$ yr^{-1} . Then, the CSM within the shock radius r_s corresponds to the mass loss in the final 4.1 years. These results are consistent with those presented by other studies for the SNe II showing early bumps (e.g., Morozova et al., 2017; Moriya et al., 2017b), suggesting that the progenitor of SN 2016bkv has also experienced an intensive mass loss just before the SN explosion.

The dense CSM derived above might also follow a strong FI features (e.g., Gal-Yam et al., 2014; Khazov et al., 2016), if there would have been a sufficiently strong ionizing flux [2]. However, at the peak of the bump, this effect is likely insignificant already, since the FI features are

[2]We use the terminology of FI features for the features produced by radiative ionization from shock breakout either at the stellar surface or at the dense CSM.

typically found only within the first day as seen in SN 2013cu and some other SNe (Gal-Yam et al., 2014) and soon disappear following the decay of the UV flux from an SN. In addition, SN 2016bkv is a LL SN IIP and the ionizing photon would be less intense than those in normal SNe IIP, leading to fainter FI features. Therefore, we do not attribute the emission lines in the early phase to the FI features. It is possible that SN 2016bkv might have shown a genuine FI feature, if it would have been observed within the first day. Adopting the properties of CSM as derived above, we estimate that a strong Hα emission ($L_{H\alpha} \sim 7 \times 10^{40}$ erg s^{-1}) should have existed if such an observation would have been performed within a day after the explosion. Interestingly, SN 2013cu and SN 2016bkv show common emission lines of C III and N III at $\sim 3-4$ days. These features may be caused by ionizing photons from the on-going interacting region.

During several days just after the bump peak (7–10 days after the explosion), spectra of SN 2016bkv show a hint of a weak Hα absorption with the velocities of 800–1000 km s^{-1} . The origin of this feature could be distinct from the strong P Cygni features with the broader emission lines after $\sim$16 days (Figure 3.5), which are produced by the SN ejecta. As discussed in this section, the bump in the light curve and narrow emission lines at the early phases are likely to be caused by the CSM interaction. In this context, we speculate that the absorption component might be originated in the unshocked CSM. The observed velocities (800–1,000 km s^{-1}) are much higher than a typical wind velocity of RSGs. This suggests that the progenitor star might have experienced a sudden, eruptive mass loss ejecting $\sim 6.8 \times 10^{-2}$ $M_{\odot}$ within r_s at only 0.2 years prior to the explosion. Although it is rather speculative, it may be the case given the large uncertainty in the mass loss of the progenitor just before the explosion. However, the gradual increase of the Hα velocities from 1,000 to 2000 km s^{-1} (Figure 3.10), is not well explained if the low velocity component is attributed to unshocked CSM. Dense observations at the early phases are necessary to fully understand possible activities of the progenitors of LL SNe IIP.

4.2 SN 2017czd

We have shown that SN 2017czd has different light curve characteristics from those of other rapidly evolving SNe currently known and it shows a plateau phase as in SNe IIP although it is very short (Section 3.2.4). We have also presented that SN 2017czd clearly shows the broad hydrogen feature in the spectra (Section 3.2.6). Based on these facts, we discuss the nature of SN 2017czd in this section.

4.2.1 Bolometric Luminosity

First, to clarify the power source of SN 2017czd, we construct the bolometric light curve based on the optical and infrared photometry. We find that the spectral energy distribution (SED) in the $BVRIJH$-band can be well explained by a single black-body function until the end of the plateau phase when the multi-band photometry is available. Therefore, we estimate the bolometric luminosity of SN 2017czd from the rising phase to the declining phase by integrating the single black-body function matching the photometry.

Because we only have the R-band photometry during the tail phase after the plateau, we estimate the bolometric luminosity in the tail phase based only on the R-band photometry. Lyman et al. (2014) investigate bolometric correction of SNe IIP and SNe IIb and find that the R-band should covers 20–25% of the total fluxes in the tail phases. Assuming this fraction, we obtain the quasi-bolometric luminosity of SN 2017czd at the tail phase. The bolometric light curve of SN 2017czd is presented in Figure 4.3.

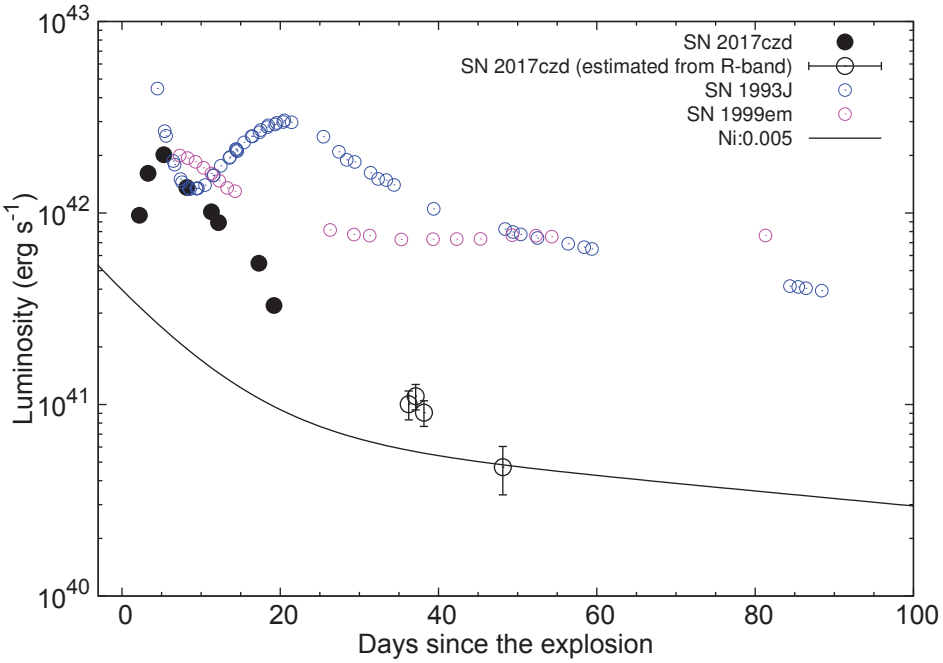

Figure 4.3: Bolometric light curve of SN 2017czd compared with those of SNe IIP 1999em (Leonard et al., 2002a) and IIb 1993J (Lewis et al., 1994). The total available energy from the nuclear decay of 0.005 $M_\odot$ of ^{56}Ni is presented.

4.2.2 ^{56}Ni Mass

One possible power source of SN 2017czd is the radioactive decay of ^{56}Ni, which is a standard power source of SNe. The total radioactive luminosity from the decay of ^{56}Ni is (Nadyozhin, 1994).

$$\left[6.5\exp\left(\frac{-t}{8.8\text{ days}}\right)+1.45\exp\left(\frac{-t}{111.3\text{ days}}\right)\right]\frac{M_{^{56}\text{Ni}}}{M_\odot}\times 10^{43}\text{ erg s}^{-1}, \tag{4.5}$$

where $M_{^{56}\text{Ni}}$ is the initial mass of radioactive ^{56}Ni .

Assuming that the major power source at the tail phase is the ^{56}Ni decay, we compare the estimated bolometric light curve with the total available decay energy (4.5) in Figure 4.3. The

total luminosity is consistent with the total decay energy from 0.005 $M_\odot$ of ^{56}Ni. However, the peak luminosity of SN 2017czd is much brighter than the expected luminosity from this ^{56}Ni mass assuming the full trapping of gamma-rays from the ^{56}Ni decay. Therefore, another energy source is necessary to explain the peak luminosity.

4.2.3 Explosion Parameters

Assuming that SN 2017czd is powered by the thermal energy from the SN shock as in SNe IIP, we first estimate the SN properties to account for the observed properties of SN 2017czd by using the scaling relation formulated by Popov (1993). We adopt -16.8 mag as the absolute V-band magnitude during the plateau and the plateau length $t_p = 13$ days. Fe II line velocity is typically used to estimate the photospheric velocity in SNe IIP but Fe II absorption lines are not found in the spectra of SN 2017czd. We only obtain the Hα line velocity ($\sim$ 20000 km s^{-1} at $t = 16.0$ days). Fe II line velocities for SNe IIP are roughly half of the Hα (e.g., Bose et al., 2013). Assuming this relation, we set the photospheric velocity of $v_{ph} = 10000$ km s^{-1} . With these parameters, the explosion energy is estimated to be 3×10^{49} erg. The hydrogen-rich envelope mass and radius of the progenitor of SN 2017czd are estimated to be 0.04 $M_\odot$ and 860 $R_\odot$, respectively.

Such an extended progenitor with a small amount of the hydrogen-rich envelope is similar to the progenitors of SNe IIb which result from massive star binary evolution (e.g., Bersten et al., 2012). To confirm if such a progenitor can explain the observational properties of SN 2017czd, The numerical light curve calculations are performed by using a progenitor model obtained from stellar evolution modeling.

4.2.4 Model of Progenitor

A progenitor model with a small hydrogen-rich envelope is calculated by Ouchi & Maeda (2017) using `MESA` code (Paxton et al., 2011, 2013, 2015, 2016, 2018). The progenitor we adopt has 16 $M_\odot$ and solar metallicity at the zero-age main sequence (ZAMS). It is in a binary system in which the initial mass of the secondary star is 15.2 $M_\odot$ (the mass ratio of 0.95) and the initial orbital period is 1000 days. The mass transfer in the binary system is treated in the non-conservative way with the mass accretion efficiency of 0.5. Further details of the progenitor evolution are refer to Ouchi & Maeda (2017). The progenitor evolution is calculated until the end of the central carbon burning. The envelope structure is not much affected by the rest of the evolution and we take this model for the light curve modeling. The final progenitor mass is 5.4 $M_\odot$ with the hydrogen-rich envelope mass of 0.4 $M_\odot$ and the helium core mass of 5.0 $M_\odot$. The hydrogen fraction in the envelope is 0.46. The progenitor radius is 767 $R_\odot$. The progenitor properties well match those of extended SN IIb progenitors (e.g., Chevalier & Soderberg, 2010).

The synthetic light curves are calculated by using `STELLA`, which is a one-dimensional multi-group radiation hydrodynamics code developed by Blinnikov et al. (1998, 2000, 2006). The mass cut of the progenitor are set at 1.4 $M_\odot$ and the thermal energy are put just above the mass cut to initiate the SN explosions. The radioactive ^{56}Ni are set just above the mass cut.

Figure 4.4 presents the synthetic multi-color light curves. The explosion energy and ^{56}Ni mass of the model is 5×10^{50} erg and 0.003 $M_\odot$, respectively. The model curve in R and I bands

after $\sim$ 35 days are followed by the decay rate of ^{56}Ni . Figure 4.5 shows the same figure as Figure 4.4 but is displayed in the bolometirc light curves. Both the multi-color and bolometric light curves are well reproduced by this model. Given the constraint from the magnitude of Gaia upper limit, SN 2017czd is found to rise more quickly than the model but the early rise may be caused by the confined dense circumstellar medium (CSM) around the progenitor (e.g., Moriya et al., 2017b, 2018; Förster et al., 2018; Morozova et al., 2018). Additionally, the luminosity of SN 2017czd in the early phase (<20 days) can be explained by the energy of interaction between the SN ejecta and this CSM (Moriya & Maeda, 2014). The contribution from the shock interaction cannot be excluded. The early discrepancy in the bolometric light curve is due to the fact that the bolometric luminosity constructed from the observations does not include contributions from the ultraviolet wavelengths which is included in the model. While the model shows some discrepancy in the tail phase in the bolometric light curve, the bolometric luminosities in the tail has a large uncertainty, since it is constructed solely by the R-band. The photospheric velocity of the model presented in Figure 4.6 is consistent with the estimation from our spectroscopy (v_{ph} = 10000 km s^{-1}), although this model shows slightly different time evolution. This difference might be due to use of the Rosseland-mean opacity in estimating the photospheric velocity. The estimated explosion energy and hydrogen-rich envelope mass by this numerical modeling are about a factor of 10 larger than those estimated by the Popov formula. This is partly because of the large helium fraction in the model envelope (Kasen & Woosley, 2009), as well as the limitation of the simple semi-analytic formula.

Figure 4.7 shows the synthetic light curves with the same progenitor models and explosion energy but with different ^{56}Ni masses. The synthetic light curve with the large amount of ^{56}Ni (0.1 $M_{\odot}$) shows the secondary peak due to the ^{56}Ni heating as in ordinary SNe IIb.

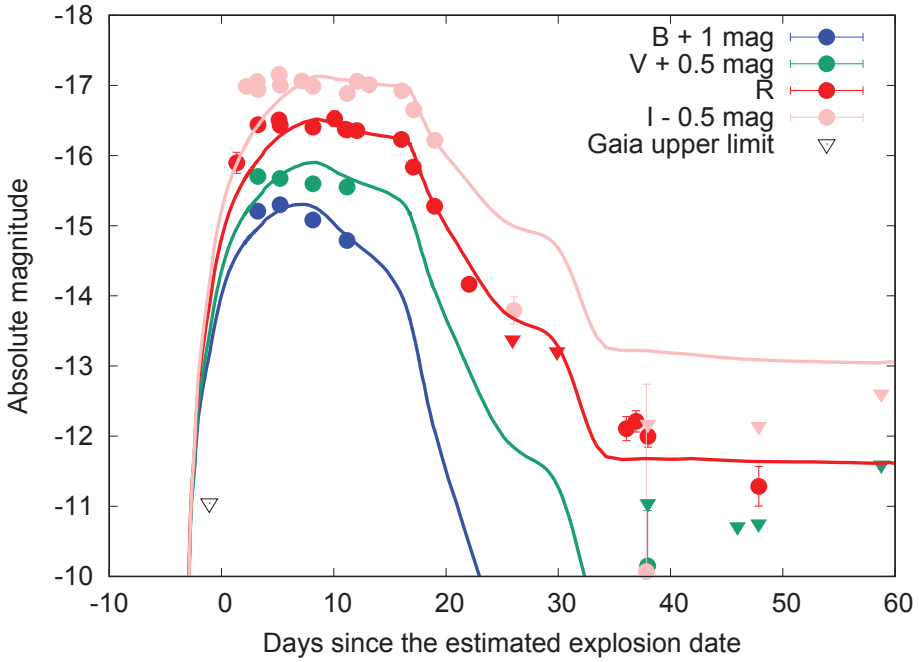

Figure 4.4: Synthetic multi-color light curves from the 5.4 $M_\odot$ progenitor model with the hydrogen-rich envelope of 0.4 $M_\odot$. The explosion energy and ^{56}Ni mass of the model are 5×10^{50} erg and 0.003 $M_\odot$, respectively. The open triangle shows the upper limit given by the observation with Gaia satellite.

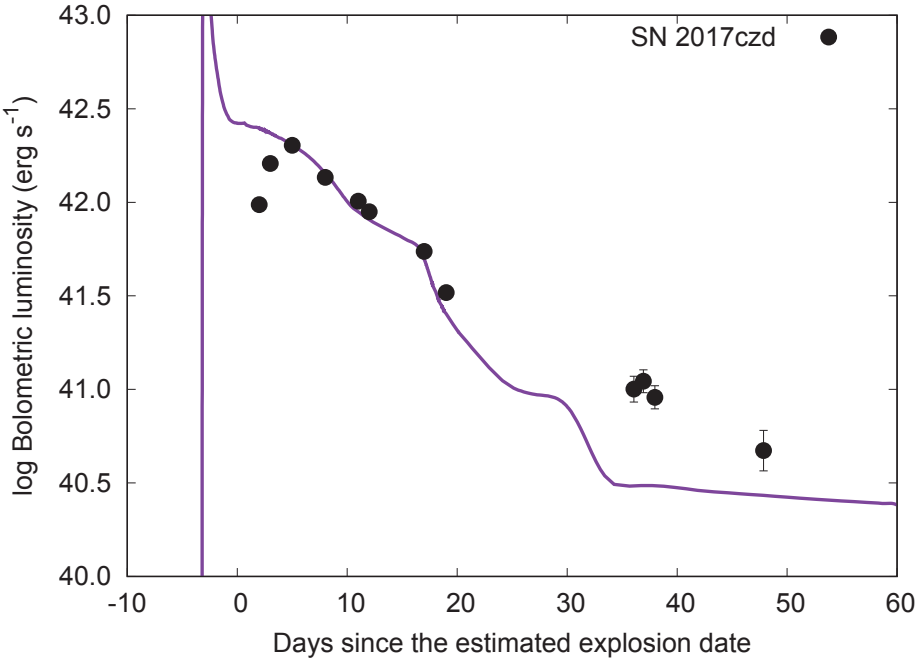

Figure 4.5: The same as Figure 4.4 but displayed in the bolometric light curves.

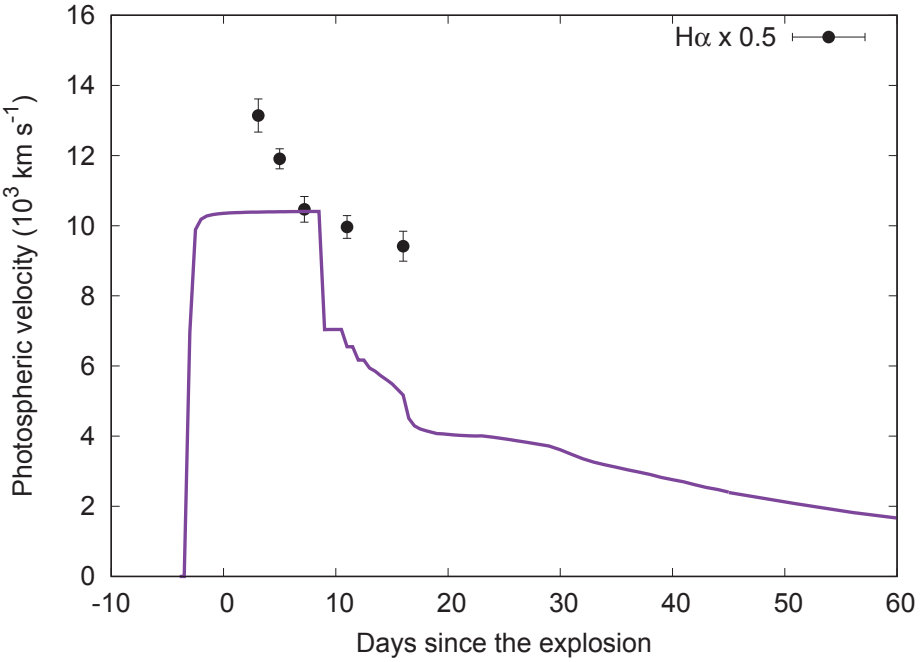

Figure 4.6: The photospheric velocity evolution of the model, where the photosphere is defined as the radius with the Rosseland-mean optical depth of 2/3. The half of the Hα velocity (Figure 3.24) which approximately traces the photospheric velocity is also shown. The time in the figure is from the observationally estimated explosion date and the explosion date of this synthetic model is 4 days before the estimated explosion date.

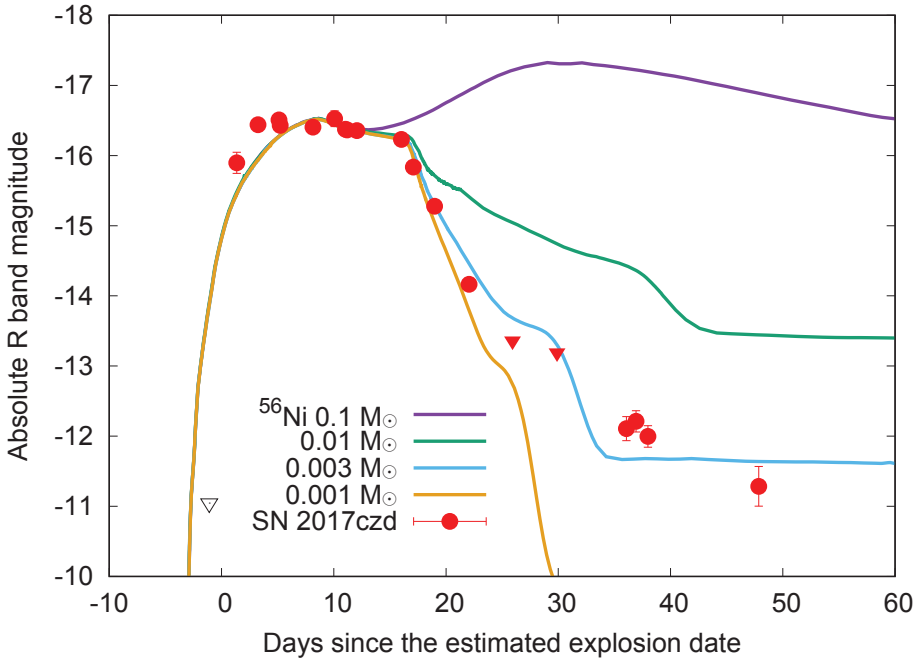

Figure 4.7: The R-band synthetic light curves with the same progenitor and explosion energy as in Figure 4.5 but with different ^{56}Ni mass. The open triangle shows the Gaia upper limit.

4.3 Observational Links between the SN and the Massive Star

4.3.1 The CSM and Massive Star

Recently, possible signatures of the interaction between the SN ejecta and CSM for some SNe IIP are detected in the early-phase spectroscopy (e.g., Yaron et al., 2017). These facts indicate that a large amount of CSM is temporally ejected by their progenitor stars just before the explosions, although theoretical studies have not predicted the temporal ejection of the envelope during the red supergiant stars (RSGs) for stellar evolutions. We can probe the progenitor nature from their CSM properties. We found that SN 2016bkv is a low-luminosity SN showing the ejecta-CSM interaction signature from our observations. In general, the stellar wind blows due to the strong radiation pressure in a massive star. Because the stellar luminosity is proportional to ~ 3.5 orders of its mass, the mass loss rate is highly dependent on the progenitor mass. We found that the progenitor mass of SN 2016bkv is significantly larger than those of average LL SNe IIP. Table 4.1 is the estimated progenitor mass of SN 2016bkv by using the relations (4.1). The progenitor mass of SN 2016bkv is even larger than those of typical SNe IIP. For LL SNe IIP, their progenitor mass are known to be rather smaller than those of typical SNe IIP by the pre-explosion image analyses using HST or hydrodynamic model (Table 4.2). From these facts, there are two populations among LL SNe IIP.

Table 4.1: The mass ratio of the progenitor of SN 2016bkv to each LL SNe IIP

Scaling source	Mass ratio to each SN	Ref.
SN 1999em	1.03	(Utrobin et al., 2007)
SN 2003Z	2.09	(Utrobin et al., 2007)
SN 2005cs	1.66	(Utrobin & Chugai, 2008)
SN 2008in	1.37	(Utrobin & Chugai, 2013)
SN 2012A	1.45	(Utrobin & Chugai, 2015)

Table 4.2: The progenitor mass of typical LL SNe IIP

Object	Progenitor mass $M_\odot$	Ref.
SN 2008bk	8–8.5	(Van Dyk et al., 2012)
SN 2008in	13.6	(Utrobin & Chugai, 2013)
SN 2003Z	14.0	(Utrobin et al., 2007)

The different explosion models may explain such observational diversities. For LL SNe IIP including SN 2016bkv, there is a weak correlation between the initial mass of the progenitor and the ^{56}Ni mass. Since the ^{56}Ni masses of typical LL SNe IIP are low comparing to typical SNe IIP (see Figure 1.8), the progenitor mass could be smaller, generally. The small ^{56}Ni mass ejection from the massive progenitor like SN 2016bkv can be explained by the failed or weak explosion (see Section 4.3.2). If we find more LL SNe IIP showing the long plateau length and the ejecta-CSM interaction signature, such scenario would be more plausible.

In the previous study, the CSM interaction has been known in limited Type of SNe e.g., SNe IIb and IIn. In SNe IIb, we know that several SNe IIb show the interaction between the SN ejecta and the CSM by X-ray observation (Immler et al., 2001; Maeda et al., 2014) In SNe IIn, the wide Hα emission lines come from this interaction. However, current studies present that only several SNe IIP display this interaction like SN 2016bkv.

Figure 4.8 shows the light curve of SN IIP 2013ej which shows possible interaction between the SN ejecta and the CSM (Morozova et al., 2017). In their study, the authors regard the small bump in the rising phase of the light curve ($\lesssim$30 days) as the sign of a such interaction. The estimated mass loss rate of SN 2013ej is quite larger than that of one of the most violently mass-losing red supergiant in our Galaxy (e.g., $\sim 10^{-3}$ $M_\odot$ yr^{-1} for VY CMa; Smith et al. 2009). As the mass loss rate of SN 2016bkv is comparable to or even larger, the progenitors of SNe II just before the explosion seem to be the powerful activity.

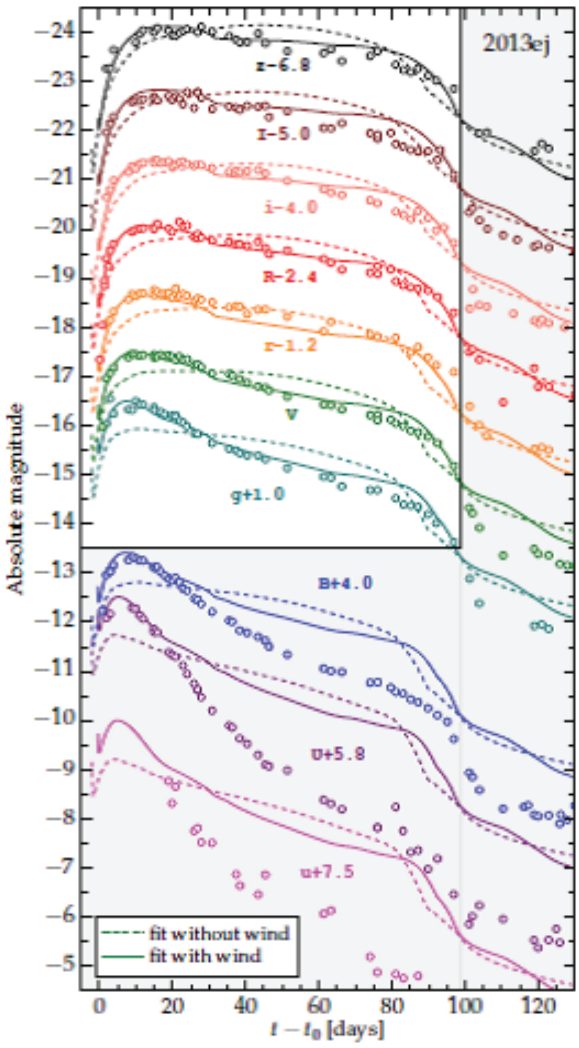

Figure 4.8: The light curves of SN 2013ej. The solid lines are best fit model with CSM (Morozova et al., 2017).

4.3.2 Diversity of Explosion

The observations of SN 2017czd are well explained by the explosion of an SN IIb progenitor. The ^{56}Ni mass of SN 2017czd ($\sim$ 0.001 $M_{\odot}$) is much smaller than those of typical SNe IIb ($\sim$ 0.1 $M_{\odot}$, e.g., Lyman et al. 2016). Thus, we suggest that SN 2017czd is a weak explosion case in the SN IIb progenitor. Such an explosion would not eject so much ^{56}Ni . It is consistent that the secondary maximum was not observed in SN 2017czd (unlike SN 1993J; see also Milisavljevic et al., 2013). It is worth noting that such a weak explosion with a small amount of ^{56}Ni may be consistent with the explosions obtained by the current state-of-the-art neutrino-driven CC SN simulations. It is well-known that the current core-collapse SN simulations fail to reproduce the standard SN explosions with the explosion energy of $\sim 10^{51}$ erg (e.g., Takiwaki et al., 2016). In

addition, Suwa et al. (2017) recently point out that the amount of ^{56}Ni produced in the explosions obtained by the current numerical simulations would be very small because they take too much time for the shock recovery. Although the current simulations are yet far from reproducing the ordinary core-collapse SN explosions, their results match the explosion properties of SN 2017czd. Alternatively, the low ^{56}Ni mass may also be a result of fallback (Tominaga et al., 2007; Moriya et al., 2010). A weak explosion can result in the unsuccessful explosion of the inner layers of the progenitor where ^{56}Ni exists. Then, little ^{56}Ni may remain in the ejecta with a small explosion energy.

Our study on SN 2017czd indicates that some rapidly evolving transients may be related to the weak explosions of SN IIb progenitors with little ^{56}Ni ejection. The ^{56}Ni-free core-collapse SN explosions to account for rapidly evolving SNe have been previously suggested for hydrogen-free extended progenitors (e.g., Kleiser & Kasen, 2014; Kleiser et al., 2018a). However, we propose that there is a little hydrogen left in the progenitor in the case of SN 2017czd. This makes the extremely short plateau in the light curve, and the hydrogen features are also expected to be observed in this case.

Chapter 5

Conclusions

In this thesis, we observed many nearby SNe II by using Kanata telescope and clarified the progenitors of peculiar SNe II,. From our extensive observations, we found two peculiar SNe II, and analyzed the property of these progenitor.

We performed our optical and NIR observations of the LL SN IIP 2016bkv. Our observations cover the initial rising phase through the plateau phase, and make this object one of the best observed LL SNe IIP. In initial phase, SN 2016bkv clearly shows a bump ($\gtrsim$1 mag) in the light curves. The bump peaks at $\sim$7 days after the explosion. During this initial phase, optical spectra show a blue continuum and narrow hydrogen emission lines. These features suggest the interaction between the SN ejecta and the CSM. Using the scaling relations for the timescale of the plateau and its luminosity, the ejecta mass of SN 2016bkv is estimated to be larger than those of other LL SNe IIP and typical SNe IIP. From the luminosity of the early bump and the Hα line emission, we conclude that the progenitor star has a relatively massive CSM in its vicinity. If the CSM has been produced by the stellar wind in the progenitor, the required mass loss rate is estimated to be $\sim 1.7 \times 10^{-2}$ $M_{\odot}$ yr^{-1} and the accumulated mass of the CSM is $\sim 6.8 \times 10^{-2}$ $M_{\odot}$, lasting at least for several years before the SN explosion (for the assumed wind velocity of 10 km s^{-1}). The mass loss rate inferred for SN 2016bkv is comparable to or even larger than the largest mass loss rate estimated for violent RSG stars in the Milky Way.

We also performed our optical and NIR observations of rapidly evolving SN 2017czd showing hydrogen features. The light curves of SN 2017czd show a short plateau ($\sim$13 days in R band) followed by a rapid decline. The spectra exhibit the hydrogen features, and overall spectra are similar to those of SNe IIP in the early phases and SNe IIb in the late phases. However, the hydrogen features are broader than those of SNe IIb and IIP, and then the line velocities are larger. In the analysis of SN 2017czd, we calculate synthetic light curves based on a binary progenitor model (16 $M_{\odot}$ at ZAMS and 5.4 $M_{\odot}$ at the explosion) with a small (0.4 $M_{\odot}$) hydrogen-rich envelope at the pre-explosion stage. The observed properties of SN 2017czd, including the short plateau duration and rapid decline, are explained by the model with the relatively low explosion energy (5×10^{50} erg) and the low ^{56}Ni mass (0.003 $M_{\odot}$). We conclude that SN 2017czd is a weak explosion of a SN IIb progenitor, which does not eject much ^{56}Ni. Our results suggest that some rapidly evolving transients are also caused by such a weak explosion of SN IIb progenitor.

From our studies on the two peculiar SNe II, we might suggest three speculations about the

progenitor of SNe II. One is that a part of the progenitors of SNe II have their CSM and its possibility is higher than those expected in previous studies. It is because the CSM emission is not always bright relative to the photospheric luminosity in plateau phase. We need to make further discussion whether all SNe II have the CSM or not. Next, a part of rapidly evolving transients can be explained by the weak explosion of SNe IIb progenitors. Such a weak explosion is likely to give a rapid evolution and low ^{56}Ni mass synthesized. Finally, some SNe II occur as the weak explosion. Several studies said that ^{56}Ni mass and explosion energy are weakly correlated with their progenitor masses. In order to obtain further informations about the weak explosion, we need to observe the SNe II from just after their explosion dates.

Acknowledgements

I would like to show my greatest appreciation to every collaborators. Advice and comments given by Kawabata-san and Yamanaka-san has been a great help in this thesis. Maeda-san, M. Tanaka-san and Moriya-san give insightful comments and suggestions for my study. I would like to thank observers for the observation of the supernovae in Kanata telescope. I acknowledge the past and present members of my laboratory.

Bibliography

Aldering, G., Humphreys, R. M., & Richmond, M. 1994, The Astronomical Journal, 107, 662

Anderson, J. P., et al. 2014, The Astrophysical Journal, 786, 67

Barbon, R., Benetti, S., Cappellaro, E., Patat, F., Turatto, M., & Iijima, T. 1995, Astronomy and Astrophysics, Supplement, 110, 513

Bersten, M. C., et al. 2012, The Astrophysical Journal, 757, 31

—. 2018, Nature, 554, 497

Bessell, M. S. 1990, Publications of the Astronomical Society of the Pacific, 102, 1181

Bildsten, L., Shen, K. J., Weinberg, N. N., & Nelemans, G. 2007, The Astrophysical Journal, Letters, 662, L95

Blinnikov, S., Lundqvist, P., Bartunov, O., Nomoto, K., & Iwamoto, K. 2000, The Astrophysical Journal, 532, 1132

Blinnikov, S. I., Eastman, R., Bartunov, O. S., Popolitov, V. A., & Woosley, S. E. 1998, The Astrophysical Journal, 496, 454

Blinnikov, S. I., Röpke, F. K., Sorokina, E. I., Gieseler, M., Reinecke, M., Travaglio, C., Hillebrandt, W., & Stritzinger, M. 2006, Astronomy and Astrophysics, 453, 229

Bose, S., et al. 2013, Monthly Notices of the Royal Astronomical Society, 433, 1871

—. 2015, The Astrophysical Journal, 806, 160

Chevalier, R. A., & Soderberg, A. M. 2010, The Astrophysical Journal, Letters, 711, L40

Chugai, N. N., & Utrobin, V. P. 2000, Astronomy and Astrophysics, 354, 557

Clayton, D. D. 1984, Principles of stellar evolution and nucleosynthesis.

Crockett, R. M., et al. 2008, Monthly Notices of the Royal Astronomical Society, 391, L5

De, K., et al. 2018, Science, 362, 201

Dessart, L., John Hillier, D., & Audit, E. 2017, Astronomy and Astrophysics, 605, A83

Dexter, J., & Kasen, D. 2013, The Astrophysical Journal, 772, 30

Drout, M. R., et al. 2014, The Astrophysical Journal, 794, 23

—. 2013, The Astrophysical Journal, 774, 58

Faran, T., et al. 2014, Monthly Notices of the Royal Astronomical Society, 442, 844

Fassia, A., et al. 2001, Monthly Notices of the Royal Astronomical Society, 325, 907

Filippenko, A. V. 1997, Annual Review of Astron and Astrophys, 35, 309

Foley, R. J., et al. 2009, The Astronomical Journal, 138, 376

Förster, F., et al. 2018, Nature Astronomy

Fraser, M., et al. 2011, Monthly Notices of the Royal Astronomical Society, 417, 1417

Fukugita, M., Shimasaku, K., & Ichikawa, T. 1995, Publications of the Astronomical Society of the Pacific, 107, 945

Gal-Yam, A., et al. 2014, Nature, 509, 471

Galbany, L., et al. 2016, The Astronomical Journal, 151, 33

Grassberg, E. K., Imshennik, V. S., & Nadyozhin, D. K. 1971, Astrophysics and Space Science, 10, 28

Graur, O., Bianco, F. B., Modjaz, M., Shivvers, I., Filippenko, A. V., Li, W., & Smith, N. 2017, The Astrophysical Journal, 837, 121

Gutiérrez, C. P., et al. 2017, The Astrophysical Journal, 850, 89

Hamuy, M. 2003, The Astrophysical Journal, 582, 905

Heger, A., Fryer, C. L., Woosley, S. E., Langer, N., & Hartmann, D. H. 2003, The Astrophysical Journal, 591, 288

Hook, I. M., Jørgensen, I., Allington-Smith, J. R., Davies, R. L., Metcalfe, N., Murowinski, R. G., & Crampton, D. 2004, Publications of the Astronomical Society of the Pacific, 116, 425

Hosseinzadeh, G., Arcavi, I., Howell, D. A., Mccully, C., & Valenti, S. 2017, Transient Name Server Classification Report, 429

Hosseinzadeh, G., Howell, D. A., Arcavi, I., Mccully, C., & Valenti, S. 2016, Transient Name Server Classification Report, 239

Hosseinzadeh, G., et al. 2018, ArXiv e-prints

Huang, F., et al. 2018, Monthly Notices of the Royal Astronomical Society, 475, 3959

Immler, S., Aschenbach, B., & Wang, Q. D. 2001, The Astrophysical Journal, Letters, 561, L107

Itagaki, K. 2016, Transient Name Server Discovery Report, 234

—. 2017, Transient Name Server Discovery Report, 420

Kasen, D., & Woosley, S. E. 2009, The Astrophysical Journal, 703, 2205

Kasliwal, M. M., et al. 2010, The Astrophysical Journal, Letters, 723, L98

Khazov, D., et al. 2016, The Astrophysical Journal, 818, 3

Kitaura, F. S., Janka, H.-T., & Hillebrandt, W. 2006, Astronomy and Astrophysics, 450, 345

Kleiser, I., Fuller, J., & Kasen, D. 2018a, Monthly Notices of the Royal Astronomical Society

Kleiser, I. K. W., & Kasen, D. 2014, Monthly Notices of the Royal Astronomical Society, 438, 318

Kleiser, I. K. W., Kasen, D., & Duffell, P. C. 2018b, Monthly Notices of the Royal Astronomical Society, 475, 3152

Landolt, A. U. 1992, The Astronomical Journal, 104, 340

Leonard, D. C., et al. 2002a, Publications of the Astronomical Society of the Pacific, 114, 35

—. 2002b, The Astronomical Journal, 124, 2490

Lewis, J. R., et al. 1994, Monthly Notices of the Royal Astronomical Society, 266, L27

Li, W., et al. 2011, Monthly Notices of the Royal Astronomical Society, 412, 1441

Lisakov, S. M., Dessart, L., Hillier, D. J., Waldman, R., & Livne, E. 2017, Monthly Notices of the Royal Astronomical Society, 466, 34

—. 2018, Monthly Notices of the Royal Astronomical Society, 473, 3863

Lyman, J. D., Bersier, D., & James, P. A. 2014, Monthly Notices of the Royal Astronomical Society, 437, 3848

Lyman, J. D., Bersier, D., James, P. A., Mazzali, P. A., Eldridge, J. J., Fraser, M., & Pian, E. 2016, Monthly Notices of the Royal Astronomical Society, 457, 328

Maeda, K., Katsuda, S., Bamba, A., Terada, Y., & Fukazawa, Y. 2014, The Astrophysical Journal, 785, 95

Mazzali, P. A., Danziger, I. J., & Turatto, M. 1995, Astronomy and Astrophysics, 297, 509

Milisavljevic, D., et al. 2013, The Astrophysical Journal, 767, 71

Modjaz, M., et al. 2009, The Astrophysical Journal, 702, 226

Moriya, T., Tominaga, N., Tanaka, M., Nomoto, K., Sauer, D. N., Mazzali, P. A., Maeda, K., & Suzuki, T. 2010, The Astrophysical Journal, 719, 1445

Moriya, T. J., & Eldridge, J. J. 2016, Monthly Notices of the Royal Astronomical Society, 461, 2155

Moriya, T. J., Förster, F., Yoon, S.-C., Gräfener, G., & Blinnikov, S. I. 2018, Monthly Notices of the Royal Astronomical Society, 476, 2840

Moriya, T. J., & Maeda, K. 2014, The Astrophysical Journal, Letters, 790, L16

Moriya, T. J., et al. 2017a, Monthly Notices of the Royal Astronomical Society, 466, 2085

Moriya, T. J., Yoon, S.-C., Gräfener, G., & Blinnikov, S. I. 2017b, Monthly Notices of the Royal Astronomical Society, 469, L108

Morozova, V., Piro, A. L., & Valenti, S. 2017, The Astrophysical Journal, 838, 28

—. 2018, The Astrophysical Journal, 858, 15

Nadyozhin, D. K. 1994, The Astrophysical Journal, Supplement, 92, 527

Nomoto, K., Maeda, K., Umeda, H., Ohkubo, T., Deng, J., & Mazzali, P. 2003, in IAU Symposium, Vol. 212, A Massive Star Odyssey: From Main Sequence to Supernova, ed. K. van der Hucht, A. Herrero, & C. Esteban, 395

Ouchi, R., & Maeda, K. 2017, The Astrophysical Journal, 840, 90

Pastorello, A., et al. 2008, Monthly Notices of the Royal Astronomical Society, 389, 955

—. 2009, Monthly Notices of the Royal Astronomical Society, 394, 2266

—. 2004, Monthly Notices of the Royal Astronomical Society, 347, 74

Paxton, B., Bildsten, L., Dotter, A., Herwig, F., Lesaffre, P., & Timmes, F. 2011, The Astrophysical Journal, Supplement, 192, 3

Paxton, B., et al. 2013, The Astrophysical Journal, Supplement, 208, 4

—. 2015, The Astrophysical Journal, Supplement, 220, 15

—. 2016, The Astrophysical Journal, Supplement, 223, 18

—. 2018, The Astrophysical Journal, Supplement, 234, 34

Pejcha, O., & Prieto, J. L. 2015, The Astrophysical Journal, 806, 225

Persson, S. E., Murphy, D. C., Krzeminski, W., Roth, M., & Rieke, M. J. 1998, The Astronomical Journal, 116, 2475

Pian, E., et al. 2006, Nature, 442, 1011

Popov, D. V. 1993, The Astrophysical Journal, 414, 712

Poznanski, D., et al. 2010, Science, 327, 58

Poznanski, D., Prochaska, J. X., & Bloom, J. S. 2012, Monthly Notices of the Royal Astronomical Society, 426, 1465

Pumo, M. L., Zampieri, L., Spiro, S., Pastorello, A., Benetti, S., Cappellaro, E., Manicò, G., & Turatto, M. 2017, Monthly Notices of the Royal Astronomical Society, 464, 3013

Pursiainen, M., et al. 2018, ArXiv e-prints

Quimby, R. M., Wheeler, J. C., Höflich, P., Akerlof, C. W., Brown, P. J., & Rykoff, E. S. 2007, The Astrophysical Journal, 666, 1093

Rest, A., et al. 2018, Nature Astronomy, 2, 307

Richmond, M. W., Treffers, R. R., Filippenko, A. V., & Paik, Y. 1996a, The Astronomical Journal, 112, 732

Richmond, M. W., et al. 1996b, The Astronomical Journal, 111, 327

Roy, R., et al. 2011, The Astrophysical Journal, 736, 76

Sanders, N. E., et al. 2015, The Astrophysical Journal, 799, 208

Schlafly, E. F., & Finkbeiner, D. P. 2011, The Astrophysical Journal, 737, 103

Shen, K. J., Kasen, D., Weinberg, N. N., Bildsten, L., & Scannapieco, E. 2010, The Astrophysical Journal, 715, 767

Shivvers, I., et al. 2017, Publications of the Astronomical Society of the Pacific, 129, 054201

Smartt, S. J. 2009, Annual Review of Astron and Astrophys, 47, 63

—. 2015, Publications of the Astron. Soc. of Australia, 32, e016

Smith, N., Hinkle, K. H., & Ryde, N. 2009, The Astronomical Journal, 137, 3558

Spiro, S., et al. 2014, Monthly Notices of the Royal Astronomical Society, 439, 2873

Sukhbold, T., Ertl, T., Woosley, S. E., Brown, J. M., & Janka, H.-T. 2016, The Astrophysical Journal, 821, 38

Suwa, Y., Tominaga, N., & Maeda, K. 2017, ArXiv e-prints

Takáts, K., et al. 2015, Monthly Notices of the Royal Astronomical Society, 450, 3137

Takiwaki, T., Kotake, K., & Suwa, Y. 2016, Monthly Notices of the Royal Astronomical Society, 461, L112

Tanaka, M., et al. 2016, The Astrophysical Journal, 819, 5

Tauris, T. M., Langer, N., Moriya, T. J., Podsiadlowski, P., Yoon, S.-C., & Blinnikov, S. I. 2013, The Astrophysical Journal, Letters, 778, L23

Tody, D. 1986, in Proceedings of the SPIE, Vol. 627, Instrumentation in astronomy VI, ed. D. L. Crawford, 733

Tody, D. 1993, in Astronomical Society of the Pacific Conference Series, Vol. 52, Astronomical Data Analysis Software and Systems II, ed. R. J. Hanisch, R. J. V. Brissenden, & J. Barnes, 173

Tominaga, N., Umeda, H., & Nomoto, K. 2007, The Astrophysical Journal, 660, 516

Turatto, M., et al. 1998, The Astrophysical Journal, Letters, 498, L129

Utrobin, V. P., & Chugai, N. N. 2008, Astronomy and Astrophysics, 491, 507

—. 2013, Astronomy and Astrophysics, 555, A145

—. 2015, Astronomy and Astrophysics, 575, A100

Utrobin, V. P., Chugai, N. N., & Pastorello, A. 2007, Astronomy and Astrophysics, 475, 973

Valenti, S., et al. 2016, Monthly Notices of the Royal Astronomical Society, 459, 3939

—. 2009, Nature, 459, 674

Van Dyk, S. D., et al. 2012, The Astronomical Journal, 143, 19

Van Dyk, S. D., Peng, C. Y., King, J. Y., Filippenko, A. V., Treffers, R. R., Li, W., & Richmond, M. W. 2000, Publications of the Astronomical Society of the Pacific, 112, 1532

Van Dyk, S. D., et al. 2014, The Astronomical Journal, 147, 37

Whitesides, L., et al. 2017, The Astrophysical Journal, 851, 107

Yaron, O., et al. 2017, Nature Physics, 13, 510

Zampieri, L., Pastorello, A., Turatto, M., Cappellaro, E., Benetti, S., Altavilla, G., Mazzali, P., & Hamuy, M. 2003, Monthly Notices of the Royal Astronomical Society, 338, 711

Zheng, W., et al. 2014, The Astrophysical Journal, Letters, 783, L24